POLITECNICO DI MILANO

DEPARTMENT OF PHYSICS

DOCTORAL PROGRAM IN PHYSICS

High-resolution spectroscopy by optical frequency combs

Supervisor: Dr. Gianluca GALZERANO

Tutor: Prof. Paolo LAPORTA

Doctoral Dissertation of:
Edoardo VICENTINI
Matr. 841450

2021 Ciclo XXXIII

Abstract

This doctoral dissertation presents different approaches to exploit optical frequency comb sources for high precision and broadband spectroscopy. In particular, a comb assisted sub-Doppler spectroscopy of fluoroform, CHF_3, is described, using a quantum cascade laser at 8.6 μm phase-locked to a mid-infrared difference frequency generation comb. Direct transmission measurement and wavelength modulation are investigated to measure absorption profiles reaching its best relative precision at the level of 10^{-11} in line centre determination, moreover pressure shift and broadening coefficient could be determined. Additionally, frequency modulation and modulation transfer techniques are exploited to frequency lock a QCL to CHF_3 line centres. In this way, a mid-infrared absolute reference is created reaching a stability at the level of 10^{-12} for an integration time of 100 s. Direct-comb spectroscopy has been also investigated. A new spectroscopy method called SMART is characterised in terms of bandwidth and ultimate resolution. Spectroscopy of acetylene gas and of a narrow Fabry-Pérot cavity have been performed at 1.5 μm demonstrating 50 kHz resolution over a span of 4 THz. Moreover, a new application for dual-comb spectroscopy is demonstrated, with a proof of principle of dual-comb high-spectral resolution hyperspectral imaging experiment of ammonia and acetylene around 1.5 μm. A resolution of 350 MHz over a 0.6 THz bandwidth has been demonstrated for 512 spatial elements parallelly acquired.

Acknowledgements

In first place, I would like to express my deep gratitude toward my supervisor Dr. Gianluca Galzerano for his patient guidance, warm encouragement and useful critiques along all my doctoral studies and experimental activities. With him, I thank also Prof. Paolo Laporta to have been always a reference point. I must thank Dr. Nicola Colucceli for counting on me as part of interesting research projects that helped me to wide my professional experience.

I am grateful to Dr. Nathalie Picqué for accepting me as an internship student at Max Planck Institute for Quantum Optics. I am very grateful to have worked with her and her group in such an inspiring environment. Thank you to Dr. Zaijun Chen, Dr. Jeong Hyun Huh, Dr. Kasper Van Gasse and Zhenhai Wang to be part of this experience.

Beyond the lab walls, I would like to thank all those people who accompanied me throughout these three years journey. Thank you to all my friends and colleagues from Politecnico di Milano: Andrea Mazzanti, Dr. Yuchen Wang, Samuele Martani, Lisa Marta Molteni and Francesco Canella. I also want to express my gratitude to Dr. Maria Ramos Vazquez for her unconditional support and for her help in the revision of this thesis.

Finally, I am deeply grateful to my parents, Donatella and Giulio, for encouraging me every day during these three years.

Contents

List of Figures

List of Tables

Abbreviations

- AOM: Acousto-optic modulator
- BS: Beam splitter
- C_2H_2: Acetylene
- CCD: Charge-coupled device
- CEO: Carrier-envelop offset
- CHF_3: Fluoroform
- CW: Continuous wave
- DFB: Distributed feedback
- DFG: Difference frequency generation
- EOM: Electro-optic modulator
- Er: Erbium
- FFT Fast Fourier transform
- FM: Frequency modulation
- FPS: Frame per second
- FTIR: Fourier transform infrared spectroscopy
- FWHM: Full width at half maximum
- FSR: Free spectral range
- GaSe: Gallium selenide
- GPS: Global positioning system
- HITRAN: High-resolution transmission molecular absorption database
- HNLF: Highly-non-linear fiber

- HWHM: Half width at half maximum
- InGaAs: Indium gallium arsenide
- IR: Infrared
- MCT: Cadmium mercury telluride
- MIR: Mid-infrared
- NH_3: Ammonia
- OFC: Optical frequency comb
- PD: Photodetector
- PID Proportional integrative derivative
- PLL: Phase-locked loop
- PSD: Power spectral density
- PZT: Piezoelectric transducer
- QCL: Quantum cascade laser
- RAM: residual amplitude modulation
- Rb: Rubidium
- RF: Radio frequency
- RIN: Relative intensity noise
- SFG: Sum frequency generation
- SFS: Self-frequency shifted
- SMART: Scanning micro-cavity resonator
- SNR: Signal-to-noise ratio
- ULE: Ultra-low expansion
- WM: Wavelength modulation

Introduction

For more than half a century, laser spectroscopy has been the main tool to identify and measure molecules and their dynamics. In the last twenty years, high-resolution and broadband spectroscopy performances could accelerate due to the advent of the optical frequency comb, an optical pulsed source that can be represented by thousand narrow line continuous wave laser all equally spaced, which frequencies can be known with a fractional accuracy of 10^{-16} or better. Originally developed to provide a direct link between the optical and radio-frequency domains (2005 Nobel prize for Physics to T. W. Hansch and J. L. Hall "for their contributions to the development of laser-based precision spectroscopy, including the optical frequency comb technique" [1][2]), optical frequency combs have spread in many other research areas, such as attosecond science, optical waveform generation, remote sensing and distance measurements, low-phase-noise microwave synthesis, optical communications and astrophysics. In between all the possible application of these sources, precision and broadband spectroscopy holds a central role since it allows a variety of applications from fundamental physics testing to biology and medicine. The availability of a frequency comb, hundreds of thousands of precise and accurate optical modes in a single laser source, allows a unique combination of large bandwidth and high spectral resolution [3]. Two main groups of techniques have emerged for frequency combs application in spectroscopy. In the first group, the optical frequency comb assists a continuous-wave (CW) as an absolute frequency reference. Once the CW laser is locked to the n-th comb mode, it can be precisely scanned across a desired molecular absorption by fine tuning of the comb mode spacing frequency (the so called comb repetition frequency). These kind of techniques are preferable when a single or few absorption lines have to be measured with the highest frequency precision and sensitivity. The second groups of techniques employs the optical frequency comb to directly probe atomic and molecular samples (from here the name direct-comb spectroscopy). Its great advantage relies on the large number of comb components which allows a massive parallel detection to acquire spectroscopic information with fast acquisition times.

This PhD research was aimed to develop novel spectroscopic methods in the near- and mid-infrared spectral regions based on optical frequency comb sources that combine high frequency precision, high sensitivity, ultrabroad bandwidth and high measurement speed in a single powerful analytical tool for high-fidelity mapping of the internal atomic and molecular energy structure. These novel class of spectrometers could be used in future in different applications, including atmospheric trace gas measurements, astrochemistry, breath analysis, industrial process monitoring and fundamental laboratory spectroscopy. Both direct and assisted comb spectroscopy approaches have been investigated, using fiber frequency combs and quantum cascade lasers (QCL).

QCL are, now, a key tool for mid-infrared and terahertz ranges. These are spectroscopic regions where many strong absorption lines are accessible, stronger than the near-infrared counterparts, offering a high sensibility in detecting most of the molecules [4]. QCL allowed to fill the gap that for long time characterised these spectral regions, with an electrically pumped system that provides high power, high efficiency and wide tunability in a compact device. In order to reach high resolution and high accuracy spectroscopy with QCL, its frequency of emission needs to be stabilised and controlled. In this sense, optical frequency combs result in an obvious solution, especially, when the goal its towards metrology application. A part of this PhD research has been devoted to find and test the best stabilisation strategies for a QCL emitting at 8.6 μm in order to investigate the fluoroform molecule with the highest spectral resolution and accuracy. This molecule presents attractive properties to be later utilised as target for ultra-high resolution spectroscopy for physical constant variance testing, in particular, the proton-electron mass ratio [5]. In this work, line centre frequencies of 95 transitions have been measured, with a best accuracy of 400 Hz, in relative terms 2×10^{-11} [6]. Thanks to frequency modulation and modulation transfer stabilisation methods, the same molecule has been used as a frequency reference. The stability of the QCL locked to the sub-Doppler profile reached a best of 4×10^{-12} [7], measure limited by the Rb-clock used as a frequency reference.

A second part of this research has been dedicated to direct-comb-spectroscopy methods in the near-infrared spectral region. This choice offers the possibility to parallelise acquisition over a ultra-broad spectral span, thank to the use of the whole frequency comb. However, efforts have to be paid and new strategies have to be found, in order to be able to resolve the single mode of a comb. Ordinary spectrometers can rarely resolve this structure, only for very high repetition frequencies, because of they low spectral resolution.

A novel direct comb technique based on a scanning micro-cavity resonator (SMART) [8] has been characterised in terms of resolution and bandwidth. It has been experimentally demonstrated a resolution limited only by the frequency comb linewidth (in the specific experiment 50 kHz over a 4 THz bandwidth [9]). This simple, compact and accurate method to resolve the mode structure of an optical frequency comb allows a straightforward absolute calibration of the optical-frequency axis with a negligible instrumental lineshape that can be used in any spectral region from UV to THz.

Additionally, a new application for another existing technique, dual-comb spectroscopy, has been explored, bringing to the realisation of a high-spectral resolution hyperspectral imaging system. Thanks to the multiple frequency component of the frequency comb and, also, thanks to the acquisition performed on a camera, a multi-parallel detection is possible, allowing to access a three dimensional space of information. A proof of concept experiment has been realised. It demonstrates the possibility to acquire in parallel 512 spacial element at a resolution of 350 MHz over a 0.6 THz bandwidth, with the possibility to coherently average in time at least up to 1000 s. Both these direct-comb-spectroscopy methods can be applied to real-time gas sensing for different kind of application like environmental monitoring, breath analysis or combustion dynamics studies.

In conclusion, this PhD thesis deals with frequency comb spectroscopies describing and discussing results obtained for high-precision sub-Doppler spectroscopy of fluoroform and QCL frequency stabilisation against the same sub-Doppler absorption line, for direct-comb SMART spectroscopy and for dual-comb hyperspectral imaging.

This thesis is structured as indicated:

- **Chapter 1**
  In this chapter, the main focus is on molecular absorptions, their intensity profile and their detection. In particular, it deals with the main causes of line broadening and shift, in linear and non-linear absorption regimes. About spectroscopic methods, a particular attention is given to frequency modulation and wavelength modulation detection strategies.

- **Chapter 2**
  The second chapter presents optical frequency combs. In particular, it describes their principles and representation in time and frequency domain; it reviews the state of art technologies to generate them in any spectral region; it illustrates how to employ frequency combs in spectroscopy.

- **Chapter 3**
  This third chapter describes high-resolution frequency comb-assisted Doppler-free spectroscopy of CHF_3. Two different spectroscopic techniques are applied: a direct measurement scheme and a wavelength modulation method.

- **Chapter 4**
  The fourth chapter presents a possible solution for the realization of a frequency standard in mid-infrared spectral region based on frequency stabilization of a QCL against a sub-Doppler absorption line of CHF_3 at 8.6 μm. A detailed analysis on the frequency stability and reproducibility is presented for two different strategies: frequency modulation and modulation transfer spectroscopy methods.

- **Chapter 5**
  The fifth chapter reports on a new direct-frequency-comb spectrometer based on a scanning micro-cavity resonator (SMART). In particular, it analyses frequency accuracy and broadband capabilities of this new tool for single comb mode detection by performing spectroscopic investigation of acetylene at around 1.5 μm.

- **Chapter 6**
  The last chapter illustrates a new application for dual-comb spectroscopy: the

hyperspectral imaging. In this case, a particular attention has been addressed to high-frequency resolution and high signal to noise ratio. In particular, hyperspectral imaging of acetylene and ammonia molecules at 1.5 μm is performed.

Chapter 1

Laser absorption spectroscopy

Most of our knowledge about the atomic structure of atoms comes from spectroscopic investigations. This tool is based on registration and analysis of the absorbed and emitted spectra after that an electromagnetic field has interacted with a spectroscopic target. Wavelength measurements of spectral lines allow to determine energy level structures. Line intensities give information, for example, about transition probability and, as a consequence, about the space charge distribution of electrons in atoms. Linewidths offer the possibility to understand lifetime of the involved energy levels or how the atom interact with environment (other atoms, magnetic and electric field). These are only few examples of information that one can extrapolate from a spectroscopic investigation.

A correct model of absorption phenomena is mandatory in order to extract understandable data. This first chapter deals with absorption mechanisms seen through different physical microscopic and macroscopic variables, describing broadening and shifting mechanisms in order to understand line shapes of absorption spectra. After that, detection strategies are presented with particular attention in modulation spectroscopy techniques.

1.1 Linear absorption

Assuming a monochromatic electromagnetic (EM) wave with an amplitude E_0 at angular frequency ω (Fig. 1.1), in a classical representation, it can be written as

$$E(z,t) = E_0 \cos(\omega t - kz). \tag{1.1}$$

This radiation interacts with an atom represented by a two-level system, upper level $|a\rangle$ and lower level $|b\rangle$, which have eigenstates at energy E_a and E_b with $E_a > E_b$. For wavelength $\lambda = 2\pi c/\omega \gg d$, being d the dimension of the considered atom, the phase of the EM wave does not change much within the volume of an atom because $kz = (2\pi/\lambda)z \ll 1$ and so it is possible to neglect the spatial variation of the field amplitude (dipole approximation). If the origin of the reference system is set in the centre of the atom, we can set $kz \simeq 0$ so that we can rewrite Eq. 1.1 as

$$E(z,t) = E_0 \cos(\omega t) = A_0(e^{iwt} + e^{-iwt}), \qquad with \quad |A_0| = \frac{1}{2}E_0. \tag{1.2}$$

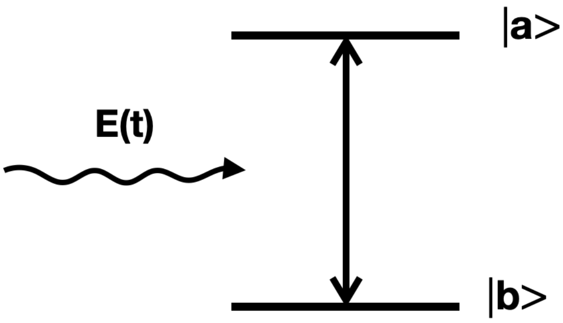

Figure 1.1: Two-level system interacting with an EM field.

The Hamiltonian operator of the atom interacting with the EM field

$$H = H_0 + V \tag{1.3}$$

can be express as a sum of an unperturbed Hamiltonian of the free atom without EM field, H_0, and an operator V that takes into account the light-matter interaction. In the dipole approximation, the operator V can be expressed as

$$V = \mu \cdot E = \mu \cdot E_0 \cos(\omega t), \tag{1.4}$$

where $\mu = -er$ is the dipole operator.

If the interaction of the EM field is weak, in order to study dynamical behaviour of the system, it is possible to approximate it by perturbation theory. In this way, unperturbed atomic eigenfunctions can be employed to study rate of transitions between states [10]. By means of Fermi's Golden Rule, it is possible to express transition rates W_{ab} between states a and b as follows

$$W_{ab} = \frac{2\pi}{\hbar^2} |H^{'}_{ab}|^2 \delta(\omega_{ab} - \omega), \tag{1.5}$$

with

$$H^{'}_{ab} = \int u_a^* V u_b d\tau = -E \int u_a^* r u_b d\tau = -E\mu_{ab}, \tag{1.6}$$

where $\delta(\omega_{ab} - \omega)$ *Kronecker's delta* (different from zero when $\omega_{ab} = \omega$) and $\omega_{ab} = (E_a - E_b)/\hbar$. The matrix element $H^{'}_{ab}$ can be expressed as function of the *dipole element* μ_{ab} as

$$|H^{'}_{ab}|^2 = \frac{e^2 E_0^2}{12} |\mu_{ab}|^2. \tag{1.7}$$

We can describe this interaction also as a function of the density of energy per unit volume $\rho(\omega)$. In this way, it is possible to write transition rates of the induced absorption using *Einstein's coefficient* of stimulated absorption B_{ab} so that

$$W_{ab} = B_{ab}\rho(\omega), \tag{1.8}$$

$$B_{ab} = \frac{\pi e^2}{3\epsilon_0 \hbar^2} |\mu_{ab}|^2, \tag{1.9}$$

with a density of energy per unit volume $\rho(\omega) = I/c$ and being $I = \frac{1}{2}\epsilon_0 c E^2$ the energy flux of the EM wave [10].

If we take into account that levels a and b can have a sub-level structure, with g_m $|a_m\rangle$ and g_n $|b_n\rangle$ sub-levels, it is possible to introduce the line strength S_{ab} as

$$S_{ab} = e^2 \sum_{m=1}^{g_m} \sum_{n=1}^{g_n} |\mu_{a_m b_n}|^2. \tag{1.10}$$

In this way, Einstein's coefficient B_{ab} can be written in a more general formula as

$$B_{ab} = \frac{\pi}{3\epsilon_0 \hbar} \frac{1}{g_a} S_{ab}. \tag{1.11}$$

Assuming now an ensemble of atoms or molecules with a density per unit volume equal to N, where the lower level $|b\rangle$ has a N_b population density and the upper level $|a\rangle$ has a N_a population density, with $N_a + N_b = N$ and $N_a - N_b = \Delta N$, the absorbed power per unit volume can be express through the transition rate as

$$P(\omega)_{abs} = \hbar\omega W_{ab} \Delta N. \tag{1.12}$$

The intensity decay of a plane EM wave propagating through a medium characterized by an absorption coefficient $\alpha(\omega)$ $[m^{-1}]$ is given by the Lambert–Beer law [10] as follows

$$I(\omega) = I_0 e^{-\alpha(\omega) z}. \tag{1.13}$$

Energy conservation requires that

$$-\frac{dI}{dz} = I\alpha = P_{abs} = \hbar\omega W_{ab} \Delta N, \tag{1.14}$$

$$\alpha(\omega) = \frac{2\hbar\omega W_{ab} \Delta N}{\epsilon_0 c E^2}. \tag{1.15}$$

The absorption coefficient can be also obtained from the atomic susceptibility, in particular, it is related to its imaginary part, χ", [11] as:

$$\alpha(\omega) = \frac{k\chi"}{2n^2}. \tag{1.16}$$

This is valid only in the linear absorption regime, where $\alpha(\omega)$ does not depend on the incoming intensity. Non-linear absorption will be analysed in section 1.2.

Another way of describing the interaction of radiation with matter involves the definition of the cross-section parameter σ $[m^2]$.It is expressed in units of area and represents the probability of a molecule, as a target, to be hit by the incoming photon flux. The total power absorbed by the ensemble is given by

$$P^{tot} = P_{abs} N = \sigma(\omega) I(\omega), \tag{1.17}$$

so that

$$\sigma(\omega) = \frac{\alpha(\omega)}{N}. \tag{1.18}$$

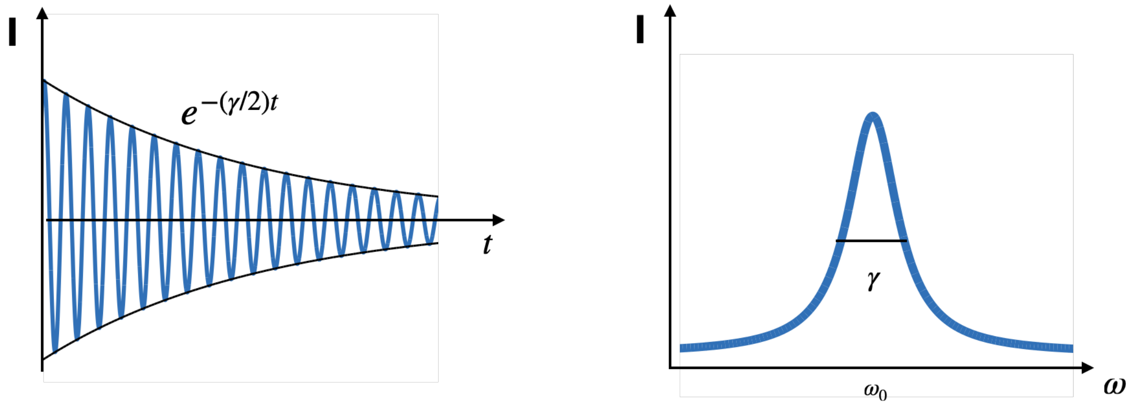

Figure 1.2: Left: Damped oscillator as a function of time. Right: Fourier transform of the damped oscillator.

Spectral absorption lines are never strictly monochromatic but they always present a spectral distribution around the central frequency ω_0 of transitions. This is called line profile. Causes of broadening are several and they can mainly divided in two classes: homogeneous broadening, where all atoms/molecules manifest the same broadening, and inhomogeneous broadening, where different atoms/molecules experience different effects.

1.1.1 Natural linewidth

An atom/molecule can emit energy as spontaneous radiation. The probability of these events is the cause of natural linewidths. In order to understand the spectral distribution of this kind of decay, it can be useful to make a comparison with the classical model of a damped oscillator to describe the atomic electron motion. An oscillator, defined by its mass m, its force constant k and its damping factor γ, is described by its differential equation of motion, with $x(t)$ being the amplitude of the oscillation,

$$\ddot{x} + \gamma\dot{x} + \omega_0^2 x = 0, \tag{1.19}$$

where $\omega_0^2 = k/m$. The solution of 1.19 with initial condition $x(0) = x_0$, $\dot{x} = 0$ and a small damping parameter γ can be approximated as

$$x(t) = x_0 e^{-(\gamma/2)t} \cos(\omega_0 t). \tag{1.20}$$

This dumped oscillation (Fig. 1.2a) can represent an atomic transition with ω_0 being the central frequency of transitions between states at energies E_a and E_b, such that $\omega_0 = (E_a - E_b)/\hbar$. Since oscillation $x(t)$ is no longer constant but it decreases, the frequency of the emitted radiation is no more monochromatic. Its spectral distribution can be retrieved by a Fourier transformation of $x(t)$. The amplitude $A(\omega)$ is given by

$$A(\omega) = \frac{1}{\sqrt{2\pi}} \int_{-\infty}^{\infty} x(t) e^{-i\omega t}. \tag{1.21}$$

If $x(t) = 0$ for $t < 0$, the previous integral can be solved giving

$$A(\omega) = \frac{x_0}{\sqrt{8\pi}} \left(\frac{1}{i(\omega - \omega_0) + \gamma/2} + \frac{1}{i(\omega + \omega_0) + \gamma/2} \right). \tag{1.22}$$

The intensity $I(\omega) \propto A(\omega)A^*(\omega)$ (Fig 1.2 b) and in the proximity of ω_0, where $(\omega_0 - \omega)^2 \ll \omega^2$, the terms with $(\omega + \omega_0)$ can be neglected, so that it is possible to retrieve the intensity profile [10]

$$I(\omega - \omega_0) = \frac{C}{(\omega - \omega_0)^2 + (\gamma/2)^2}, \tag{1.23}$$

being C a normalization constant. Setting $C = I_0\gamma/2\pi$, the line profile becomes Lorentzian

$$L(\omega) = \frac{\gamma/2\pi}{(\omega - \omega_{ab})^2 + (\gamma/2)^2}, \tag{1.24}$$

so that

$$I(\omega - \omega_0) = I_0 L(\omega - \omega_0). \tag{1.25}$$

This line broadening can be linked to the finite lifetime of energy levels. Multiplying equation 1.19 by $m\dot{x}$, we have

$$m\ddot{x}\dot{x} + m\omega_0^2 x\dot{x} = -\gamma m\dot{x}^2. \tag{1.26}$$

The left side is the time derivative of the total energy W, the sum of the kinetic and the potential energies of an harmonic oscillator, and it can be written as follows

$$\frac{d}{dt}\left(\frac{m}{2}\dot{x}^2 + \frac{m}{2}\omega^2 x^2\right) = \frac{dW}{dt} = -\gamma m\dot{x}^2. \tag{1.27}$$

Inserting $x(t)$ from equation 1.20, neglecting terms with γ^2 and time averaging, the time-averaged radiant power P is given as

$$P(t) = -\frac{\gamma}{2} m x_0^2 \omega_0^2 e^{-\gamma t}. \tag{1.28}$$

This radiant power must be compared with the radiant power emitted by spontaneous emission. In fact, an atom in the excited state E_i can go through spontaneous emission with a rate given by A_i Einstein coefficient so that given a population N_i of atoms in the excited state, they decay as

$$dN_i = -A_i N_i dt, \tag{1.29}$$

and integrated with $N_i(0) = N_0$, they become

$$N_i(t) = N_0 e^{-A_i t}. \tag{1.30}$$

The radiant power P is proportional to $N(t)$

$$P(t) = N_i(t)\hbar\omega_{ab} A_i = ce^{-A_i t}. \tag{1.31}$$

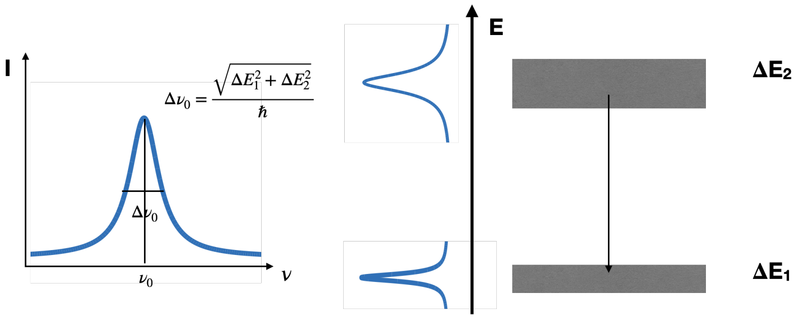

Figure 1.3: Left: line with natural linewidth $\Delta\nu_0$. Right: two levels system with uncertainties ΔE_1 and ΔE_2.

Comparing equation 1.28 and 1.31, we can state that the natural linewidth is due to a finite lifetime of the excited state with $\gamma \propto A_i$.

The same result can also be retrieved from the uncertainty principle (Fig. 1.3)[11]. An energy level uncertainty ΔE can be related to the mean lifetime τ_i as $\Delta E_i \simeq \hbar/\tau_i$. The transition frequency $\omega_{ik} = (E_i - E_k)/\hbar$ has therefore an uncertainty expressed as

$$\delta\omega = \Delta E/\hbar = 1/\tau. \tag{1.32}$$

If the lower level E_k is not in the ground state, it has a finite lifetime τ_k so that the total frequency uncertainty can be written as

$$\delta\omega_n = \sqrt{(1/\tau_i^2 + 1/\tau_k^2)}. \tag{1.33}$$

1.1.2 Collisional Broadening

When two atoms A and B approach each other, their energy levels shift because of interaction [11]. In general, these shifts are different for each energy level and they can be positive or negative depending on the kind of interaction (repulsive or attractive).

Typical potential curves of interaction as a function of the distance R between A and B are present in Fig. 1.4 [11]. This interaction at distances $R < R_c$ is called collision and the R_c radius is the collision radius. If no energy is transferred between the pair, this collision is said elastic. Without any recombination mechanism, the partner interacts for a typical collision time $\tau_c \simeq R_c/v$, which depends on the relative velocity v.

During the collision time, the atom A changes its frequency of resonance. In particular, the energy difference between the energy levels k and i becomes a function of the interatomic distance $R(t)$ at the time of the transition so that

$$\Delta E_{ik} = (E_i(R) - E_k(R)) \tag{1.34}$$

As a consequence, the intensity profile, $I(\omega)$, due to collisions can by expressed [11] by

$$I(\omega) \propto \int A_{ik}(R) P_{col}(R) \left[E_i(R) - E_k(R)\right] dR. \tag{1.35}$$

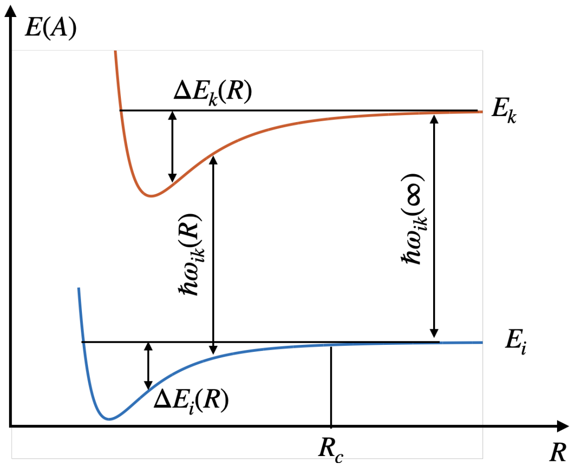

Figure 1.4: Potential curve as a function of atoms distance R.

$A_{ik}(R)$ is the spontaneous transition probability and it is function of R because of the change of the electronic wave-function due to the presence of the second atom B. $P_{col}(R)$ is the probability that the distance between the atoms is in the range between R and $R + dR$ during the iteration time.

Besides elastic collisions, inelastic collisions may also take place. In this case, a part or all the excitation energy is transferred from atom A to atom B. Such collision results in a decrease number atoms in the excited states level E_i, and from this the name of quenching collisions.

Inelastic collision probability A_i^{col} is given by

$$A_i^{col} = N_B \sigma_i v, \tag{1.36}$$

with

$$v = \sqrt{\frac{8kT}{\pi\mu}}, \qquad \mu = \frac{M_A M_B}{M_A + M_B}. \tag{1.37}$$

The total probability A_i that level E_i is depopulated is due to spontaneous emission and inelastic collision so that

$$A_i = A_i^{rad} + A_i^{coll}. \tag{1.38}$$

This probability of depopulation causes a corresponding line broadening, similar to natural linewidth, keeping a Lorentzian profile, such that [11]

$$I(\omega) = \frac{C}{(\omega - \omega_0)^2 + [(\gamma_n + \gamma_{col})/2]^2}. \tag{1.39}$$

Summarizing with elastic and inelastic collision intensity profiles of absorption, $I(\omega)$ becomes

$$I(\omega) = \frac{C^*}{(\omega - \omega_0 - \delta\omega)^2 + [(\gamma_n + \gamma_{col})/2]^2}, \tag{1.40}$$

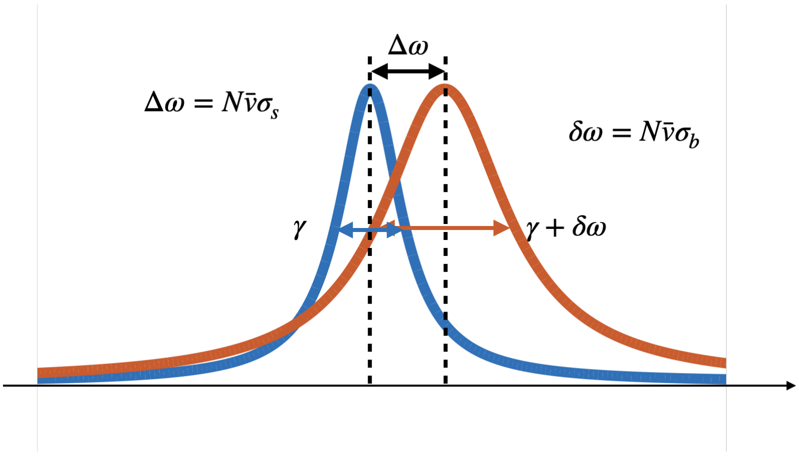

Figure 1.5: Lorentzian line shape shift and broadening due to collisions. In blue an unperturbed transition, in red after collision broadening and shift.

with $C^* = (I_0/2\pi)(\gamma + N_B v\sigma_b)$. The line shift $\delta\omega$

$$\delta\omega = N_B v\sigma_s \tag{1.41}$$

and line broadening γ

$$\gamma = \gamma_n + N_B v\sigma_b \tag{1.42}$$

can be calculated with the number density N_B of collision parameters B and the collision cross-section σ_s for line shift and the σ_b for broadening.

1.1.3 Transit time broadening

In transitions with a long spontaneous lifetime, e.g. rotational-vibrational transitions, the transit time $T = d/|\boldsymbol{v}|$ of a molecule through a laser beam of diameter d must be taken in consideration in broadening mechanisms. The linewidth of molecular transitions is no longer limited by the spontaneous transition probabilities, but by the time of interaction with laser beam.

This can be seen as an harmonic oscillator that interacts with Gaussian distribution of the EM field

$$E = E_0 e^{-r^2/w^2}\cos(\omega t), \tag{1.43}$$

where $2w$ is the diameter of the beam. Coming back to the frequency spectrum of a damped oscillator of equation 1.21 and substituting $x(t) = \alpha E$, one obtain an intensity profile [11]

$$I(\omega) = I_0 \exp\left(-(\omega-\omega_0)^2 \frac{w^2}{2v^2}\right). \tag{1.44}$$

This is a Gaussian profile with a FWHM equal to

$$\delta\omega_{tt} = \frac{2v}{w}\sqrt{2\ln 2} \simeq 2.4v/w \to \delta\nu_{tt} \simeq 0.4v/w. \tag{1.45}$$

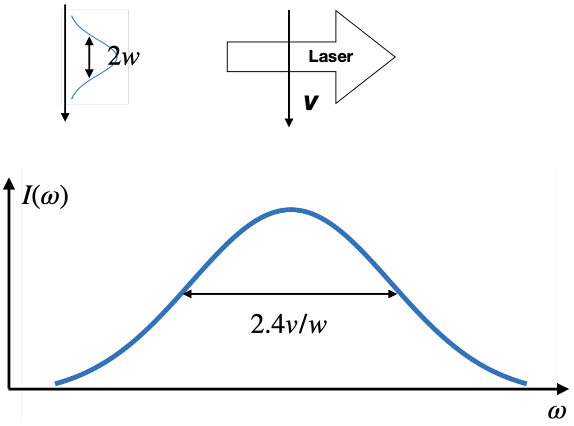

Figure 1.6: Intensity profile of an atom traversing a laser beam with a Gaussian profile with linewidth $2w$.

Until now, we have considered a plane wave front for the interacting radiation and molecules moving parallel to these planes. However, the phase surfaces of a Gaussian beam are curved. If this effect is included in the calculation as an additional phase shift depending on the location of different molecules respect to the wavefront, we obtain the transit time broadened halfwidth, including the wavefront curvature effect

$$\delta\omega = \frac{2v}{w}\sqrt{2\ln 2}\left[1+\left(\frac{\pi w^2}{R\lambda}\right)^2\right]^{1/2} = \delta\omega_{tt}\left[1+\left(\frac{\pi w^2}{R\lambda}\right)^2\right]^{1/2}. \tag{1.46}$$

1.1.4 Doppler linewidth

In general ,natural linewidth can not be observed because its Lorentzian profile is concealed by other broadening effects. One of these major contribution come from Doppler width, which is due to the thermal motion of molecules.

Considering a molecule with a velocity $\boldsymbol{v}$ relative to the frame of reference of the observer, the central frequency of molecular emission ω_0 in the molecular coordinate system shifts due to Doppler effect to

$$\omega_e = \omega_0 + \boldsymbol{k}\cdot\boldsymbol{v}, \tag{1.47}$$

where $\boldsymbol{k} = \frac{2\pi}{\lambda}\hat{\boldsymbol{u}}_k$ is the wave vector of the emitted radiation.

An observer sees an increasing ω_e if molecules move towards him/her ($\boldsymbol{k}\cdot\boldsymbol{v} > 0$) and decreasing if molecules move in opposite direction ($\boldsymbol{k}\cdot\boldsymbol{v} < 0$). Similarly, the frequency of a plane EM wave $\boldsymbol{E} = \boldsymbol{E_0}\exp(i(\omega t + \boldsymbol{k}\cdot\boldsymbol{r}))$ is shifted and in moving molecule frame of reference becomes

$$\omega^{'} = \omega - \boldsymbol{k}\cdot\boldsymbol{v}. \tag{1.48}$$

Molecules can absorb only frequencies $\omega^{'}$ equal to ω_0 so that the absorbed frequency $\omega = \omega_a$ is given by (Fig. 1.7)

$$\omega_a = \omega_0 + \boldsymbol{k}\cdot\boldsymbol{v}. \tag{1.49}$$

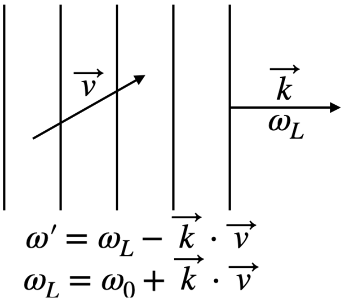

Figure 1.7: Shifted frequency due to Doppler effect, where ω' is the frequency in molecules frame of reference and ω_L is the absorbed frequency.

Absorption happens at higher frequency if molecules move parallel to the wave propagation. If z-direction is chosen coincident with light direction so that $k = \{0, 0, k_z\}$ (and $k = 2\pi/\lambda$) equation 1.49 becomes

$$\omega_a = \omega_0(1 + v_z/c). \tag{1.50}$$

At thermal equilibrium, the number of molecules per unit volume $n_i(v_z)dv_z$ in level E_i with a velocity between v_z and $v_z + dv_z$ is given by

$$n_i(v_z)dv_z = \frac{N_i}{v_p\sqrt{\pi}} e^{-(v_z/v_p)^2} dv_z, \tag{1.51}$$

where N_i is the density of the molecules in E_i level, $v_p = (2kT/m)^{1/2}$ is the most probable velocity, m is the mass of the molecule, T is the absolute temperature and k is Boltzmann's constant. Using equation 1.50 for velocity v_z and frequency ω, then

$$n_i(\omega)d\omega = \frac{N_i c}{\omega_0 v_p\sqrt{\pi}} \exp\left[-\left(\frac{c(\omega-\omega_0)}{\omega_0 v_p}\right)^2\right] d\omega. \tag{1.52}$$

Since absorbed power $P(\omega)d\omega$ is proportional to the density $n(\omega)d\omega$ of molecules, the intensity profile of a Doppler-broadened spectral line becomes [11]

$$I(\omega) = I_0 \exp\left[-\left(\frac{c(\omega-\omega_0)}{\omega_0 v_p}\right)^2\right]. \tag{1.53}$$

This is a Gaussian profile with a FWHM $\delta\omega_D$ equal to

$$\delta\omega_D = 2\sqrt{\ln 2}\omega_0 v_p/c = \frac{\omega_0}{c}\sqrt{8kT\ln 2/m}. \tag{1.54}$$

This linewidth can be also expressed in frequency units using the mass of a mole,$M = N_A m$, and gas constant, $R = N_A k$ (N_A Avogadro's constant) , as follows

$$\delta\nu_D = 7.16 \times 10^{-7}\nu_0\sqrt{T/M}. \tag{1.55}$$

1.1.5 Voigt profile

When different broadening contributions are present, a spectral line can not be strictly represented by a Gaussian or by a Lorentzian profile.

For example, let's include the finite lifetime of molecules (Lorentzian broadening) in the case of a Doppler effect (Gaussian broadening). From equation 1.50, not all molecules absorb at the same frequency but instead they absorb at $\omega^{'} = \omega_0(1 + v_z/c)$. Because each molecules has energy levels with finite lifetimes, the frequency response of these molecules is represented by a Lorentzian profile 1.25 with central frequency ω'. Let $n(\omega')d\omega' = n(v_z)dv_z$ be the number of molecules per unit volume with velocity between v_z e $v_z + dv_z$, the spectral intensity distribution $I(\omega)$ of total absorption is then expressed by

$$I(\omega) = I_0 \int n(\omega^{'})L(\omega - \omega^{'})d\omega^{'}. \tag{1.56}$$

Thanks to equations 1.51 and 1.24 the above equation can be written as

$$I(\omega) = C \int_0^{\infty} \frac{\exp\left\{-\left[(c/v_p)\left(\omega_0 - \omega^{'}\right)/\omega_0\right]^2\right\}}{\left(\omega - \omega^{'}\right)^2 + (\gamma/2)^2} d\omega^{'}, \tag{1.57}$$

with

$$C = \frac{\gamma N_i c}{2 v_p \pi^{3/2} \omega_0}. \tag{1.58}$$

This expression can be also re-written using the complex error function $\widetilde{w}$

$$\widetilde{w} = e^{-z}\left(1 + \frac{2i}{\sqrt{\pi}} \int_0^z e^{s^2} ds\right) \tag{1.59}$$

as

$$I(\omega) = \frac{2\pi\sqrt{\ln 2}}{\sqrt{\pi}\Gamma_G} \operatorname{Re}\left[\widetilde{w}(x + iy)\right], \tag{1.60}$$

with

$$x = \frac{\sqrt{\ln 2}(\omega - \omega_0)}{\Gamma_G} \qquad y = \sqrt{\ln 2}\frac{\Gamma_L}{\Gamma_G}. \tag{1.61}$$

This intensity profile, convolution of Lorentzian and Gaussian profiles, is called Voigt profile (Fig. 1.8).

1.2 Non-linear absorption

At sufficiently large laser intensities, the pumping rate becomes higher than the relaxation rate resulting in a decrease of the population in absorbing levels. This results in a nonlinear dependence, a saturation of the absorbed radiation power on the incident power. In the following section the basic physics of nonlinear absorption ae discussed. The spectral profile of such partially saturated transitions are different for homogeneous and inhomogeneous broadened lines so they will be treated separately.

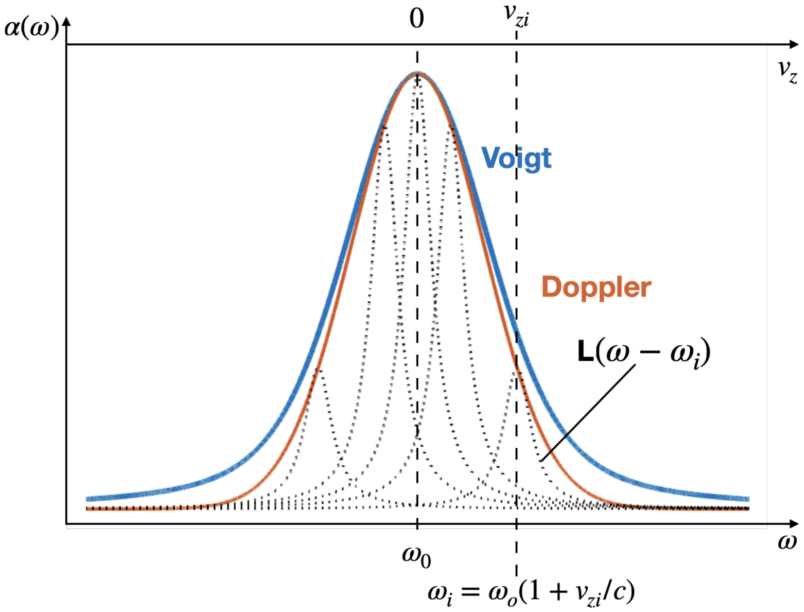

Figure 1.8: Voigt profile as result of the convolution between a Lorentzian transition $L(\omega)$ of molecules with different velocity components v_{zi}.

1.2.1 Saturation of level population

Considering a two level system with population densities N_1 and N_2 of respective levels, these two levels are coupled each other by absorption and emission processes as shown in fig.1.9.

With probability $P = B_{12}\rho(\omega)$ for transition $|1\rangle \rightarrow |2\rangle$ from absorption of a photon $\hbar\omega$ and relaxation probability γ_i for level $|i\rangle$, the rate equation for population densities is

$$\frac{dN_1}{dt} = -\frac{dN_2}{dt} = -PN_1 - \gamma_1 N_1 + PN_2 + \gamma_2 N_2. \tag{1.62}$$

At the stationary regime $(dN_i/dt = 0)$ and with $N = N_1 + N_2$, we obtain

$$(P + \gamma_1)N_1 = (P + \gamma_2)(N - N_1) \Rightarrow N_1 = N\frac{P + \gamma_2}{2P + \gamma_1 + \gamma_2}, \tag{1.63a}$$

$$(P + \gamma_2)N_2 = (P + \gamma_1)(N - N_2) \Rightarrow N_2 = N\frac{P + \gamma_1}{2P + \gamma_1 + \gamma_2}. \tag{1.63b}$$

For high pumping rate $(P \rightarrow \infty)$, the population density approaches to $N/2$ so that absorption coefficient $\alpha = \sigma(N_1 - N2)$ approaches zero.

Without any pumping mechanism $(P = 0)$, the population densities are

$$N_{10} = \frac{\gamma_2}{\gamma_1 + \gamma_2}N, \qquad N_{20} = \frac{\gamma_1}{\gamma_1 + \gamma_2}N. \tag{1.64}$$

With $\Delta N = N_1 - N_2$ and $\Delta N_0 = N_{10} - N_{20}$ we could write

$$\Delta N = N\frac{\gamma_2 - \gamma_1}{2P + \gamma_1 + \gamma_2}, \tag{1.65a}$$

$$\Delta N_0 = N\frac{\gamma_2 - \gamma_1}{\gamma_1 + \gamma_2}, \tag{1.65b}$$

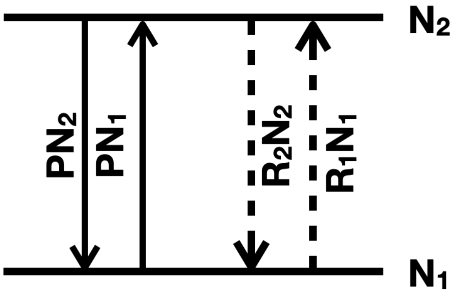

Figure 1.9: Two level system with pumping and relaxing processes.

which gives

$$\Delta N = \frac{\Delta N_0}{1 + 2P/(\gamma_1 + \gamma_2)} = \frac{\Delta N_0}{1+S}. \tag{1.66}$$

The saturation parameter

$$S = \frac{2P}{(\gamma_1 + \gamma_2)} = \frac{P}{\overline{\gamma}} = \frac{I_0}{I_{sat}} \tag{1.67}$$

represents the ratio between the pumping rate P and the average relaxation rate $\overline{\gamma} = (\gamma_1 + \gamma_2)/2$ or the ratio between the incoming intensity and the saturation intensity, defined as:

$$I_{sat} = \frac{3c\epsilon_0\hbar^2}{\mu_{12}^2} \frac{\gamma_1\gamma_2}{\gamma_1 + \gamma_2}. \tag{1.68}$$

We can also calculate the saturated absorption coefficient $\alpha(\omega) = \sigma_{12}\Delta N$ as

$$\alpha = \frac{\alpha_0}{1+S}, \tag{1.69}$$

being α_0 the unsaturated absorption coefficient without pumping.

1.2.2 Saturation of homogeneous line profiles

According to eq.1.12, the power absorbed per unit volume on transition $|1\rangle \rightarrow |2\rangle$ by atoms with population densities N_1 and N_2 in a radiation field with a spectral energy density $\rho(\omega)$ is

$$P = \hbar\omega B_{12}\rho(\omega)\Delta N = \hbar\omega B_{12}\rho(\omega)\frac{\Delta N_0}{1+S} = \hbar\omega\overline{\gamma}\frac{\Delta N_0}{1+S^{-1}}, \tag{1.70}$$

with $S = B_{12}\rho(\omega)/\overline{\gamma}$.

We can also introduce a frequency dependent saturation parameter S_ω in order to take into account the Lorentzian profile of absorption probabilities, so that

$$S_\omega = \frac{B_{12}\rho(\omega)}{\overline{\gamma}}L(\omega - \omega_0) = S_0\frac{(\gamma/2)^2}{(\omega-\omega_0)^2 + (\gamma/2)^2}, \tag{1.71}$$

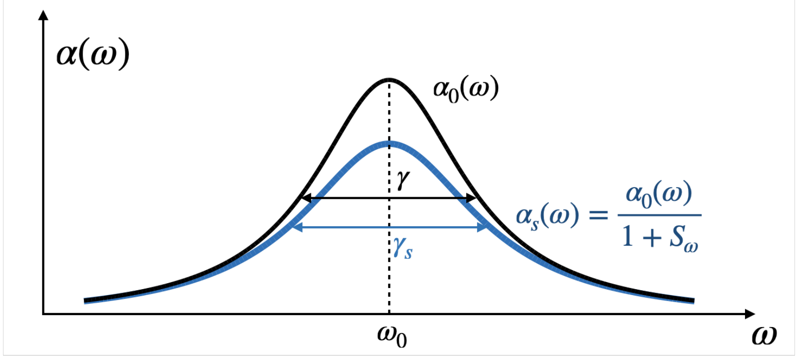

Figure 1.10: Homogeneous line profile before (black) and after saturation effects (blue).

with $S_0 = S(\omega_0)$. Substituting in eq.1.70 we obtain

$$P(\omega) = \frac{\hbar\omega\overline{\gamma}\Delta N_0 S_0(\gamma/2)^2}{(\omega-\omega_0)^2 + (\gamma/2)^2(1+S_0)} = \frac{C}{(\omega-\omega_0)^2 + (\gamma_s/2)^2}. \tag{1.72}$$

This is again a Lorentzian profile but with an increased FWHM: $\gamma_s = \gamma\sqrt{1+S_0}$.

From eq.1.72 is possible to retrieve the absorption coefficient α as follows

$$\alpha_s(\omega) = \alpha_0(\omega_0)\frac{(\gamma/2)^2}{(\omega-\omega_0)^2 + (\gamma_s/2)^2} = \frac{\alpha_0(\omega)}{1+S_\omega}, \tag{1.73}$$

where

$$\alpha_0(\omega) = \frac{\alpha_0(\omega_0)(\gamma/2)^2}{(\omega-\omega_0)^2 + (\gamma/2)^2}; \qquad \alpha_0(\omega_0) = \frac{2\hbar\omega B_{12}\Delta N_0}{\pi c\gamma}. \tag{1.74}$$

This shows that the saturation decreases the absorption coefficient by $(1+S_\omega)$ factor. At the line centre, this factor has its maximum value so that saturation is stronger; at the line wing saturation is weaker. This effect brings to a line broadening.

1.2.3 Saturation of inhomogeneous line profiles

The absorption cross-section for a molecule with a Maxwell-Boltzmann distribution of velocity around v_z, through a monochromatic light wave $E = E_0\cos(\omega t + kz)$ and without saturation can be written as

$$\sigma_{12} = \sigma_0\frac{(\gamma/2)^2}{(\omega-\omega_0-kz)^2 + (\gamma/2)^2}, \tag{1.75}$$

where $\sigma_0 = \sigma(\omega = \omega_0 + kz)$ is the maximum cross-section at the line centre of the Doppler-shifted molecular transition and γ is the natural linewidth of the transition.

Due to saturation, the density of population of energy levels changes: while the lower level $|1\rangle$ with density $N_1(v_z)dv_z$ decreases in velocity interval $dv_z = \gamma/K$, the upper level $|2\rangle$ with density $N_2(v_z)dv_z$ increases correspondingly.

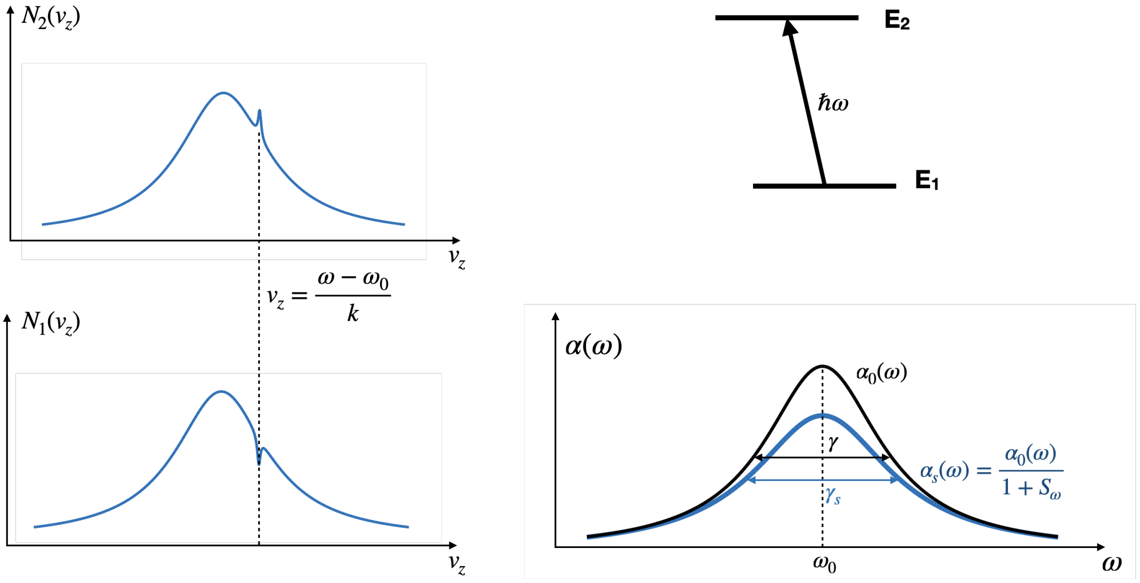

a) b)

Figure 1.11: Velocity-selective Bennet hole formation. a) Holes in upper and lower population states $N_i(v_z)$ due to saturation. b) Resulting saturation profile (blue curve).

With eq.1.66 and eq.1.71, it is possible to write the new population densities of levels $|1\rangle$ and $|2\rangle$ as

$$N_1(\omega, v_z) = N_0^1(v_z) - \frac{\Delta N^0}{\gamma_1 \tau} \left[\frac{S_0(\gamma/2)^2}{(\omega - \omega_0 - kz)^2 + (\gamma_s/2)^2} \right], \tag{1.76a}$$

$$N_2(\omega, v_z) = N_0^2(v_z) + \frac{\Delta N^0}{\gamma_2 \tau} \left[\frac{S_0(\gamma/2)^2}{(\omega - \omega_0 - kz)^2 + (\gamma_s/2)^2} \right], \tag{1.76b}$$

where $\gamma = \gamma_1 + \gamma_2$ denotes the homogeneous width of the transition and $\gamma_s = \gamma\sqrt{1 + S_0}$ (Fig.1.11(a)). The quantity

$$\tau = \frac{1}{\gamma_1} + \frac{1}{\gamma_2} = \frac{\gamma}{\gamma_1 \gamma_2} \tag{1.76c}$$

is called the longitudinal relaxation time and

$$T = \frac{1}{\gamma_1 + \gamma_2} = \frac{1}{\gamma} \tag{1.76d}$$

is the transverse relaxation time.

Subtracting (1.76b) from (1.76a) yields for the saturated population difference

$$\Delta N(\omega_s, v_z) = \Delta N^0(v_z) \left[1 - \frac{S_0(\gamma/2)^2}{(\omega - \omega_0 - kz)^2 + (\gamma_s/2)^2} \right]. \tag{1.77}$$

This distribution presents a minimum at $v_z = (\omega - \omega_0)/k$ which is called *Bennet hole* (Fig 1.11 a). This hole has an homogeneous width $\gamma_s = \gamma\sqrt{1 + S_0}$ and a depth at the center $\Delta N_0 S_0/(1 + S_0)$.

The total absorption coefficient can be calculated as follows

$$\alpha(\omega) = \int \Delta N(v_z)\sigma_{12}(\omega, v_z)dv_z. \tag{1.78}$$

Using the mathematical expression given for $\Delta N v_z$ from eq.1.77, σ_{12} from eq.1.75 and $\Delta N^0(v_z)$ from eq.1.51), yields

$$\alpha(\omega) = \frac{\Delta N \sigma_0}{v_p\sqrt{\pi}} \int \frac{e^{-(v_z/v_p)^2} dv_z}{(\omega - \omega_0 - kz)^2 + (\gamma_s/2)^2}, \tag{1.79}$$

which is again a Voigt profile but with a different amplitude and linewidth (from γ to γ_s) (Fig. 1.11 b).

The integral eq.1.79 can be approximated taking into account that the Doppler profile is much larger than the homogeneous width γ_s, so that the numerator does not vary much within the interval $\Delta v_z = \gamma_s/k$[11]. Therefore, we can take out the exponential from the integral and solve it using $v_z = (\omega - \omega_0)/k$ as follows

$$\alpha_s(\omega) = \frac{\alpha^0(\omega_0)}{\sqrt{1+S_0}} \exp\left\{ - \left[\frac{\omega - \omega_0}{0.6\delta\omega_D} \right]^2 \right\}, \tag{1.80}$$

where the unsaturated absorption coefficient is given by

$$\alpha_0(\omega_0) = \Delta N_0 \frac{\sigma_0 \gamma c \sqrt{\pi}}{v_p \omega_0},$$

and the Doppler width is equal to

$$\delta\omega_D = \frac{\omega_0}{c}\sqrt{\frac{8kT\ln 2}{m}}.$$

Bennet holes can not be directly detected; however it is possible to observe them if two laser beams are used. The first beam, the pump laser, burns a hole into the population density; whereas the second beam one, a weak probe laser, scans the created hole. It is possible to use the same laser for pump and probe if the incident beam is reflected back into the sample (Fig. 1.12).

If the intensity of the retro-reflected beam is weak with respect to the incoming beam, the absorption coefficient can be expressed as [11]

$$\alpha(\omega) = \alpha^0(\omega) \left[1 - \left(1 - \frac{1}{\sqrt{1+S}} N g_V(\omega - \omega_0) \right) \right], \tag{1.81}$$

where $g_V(\omega - \omega_0)$ is normalised Voigt lineshape profile and N a normalisation factor for the saturation profile called Lamb dip. Lamb dip profile has a Gaussian contribution coming from a transit time, Γ_{tt}, and a Lorentzian contribution due to pressure broadening and saturation $\Gamma_L = \gamma_0[1 + (1 + P/P_s)]$.

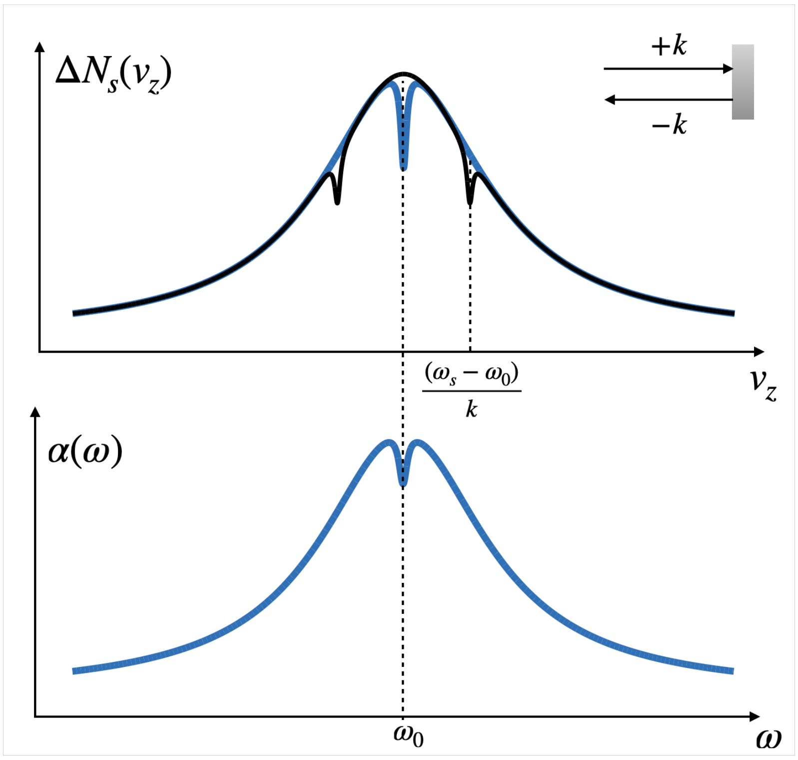

Figure 1.12: Top: Bennet holes in case of two counter-propagating waves for $\omega \neq \omega_0$ and $\omega = \omega_0$ (blue curve). Bottom: Resulting absorption profile with the characteristic Lamb's dip.

1.3 Laser absorption methods

Different strategies and techniques can be used to record absorption profiles. The simplest solution relies on the measurement of the intensity of light as a function of frequency before,$I_0(\omega)$, and after, $I(\omega)$, an interaction with a sample. According to Lambert-Beer's law in eq.1.13, the absorption can be expressed as

$$\alpha(\omega)z = \ln \frac{I(\omega)}{I_0(\omega)}. \tag{1.82}$$

In case of weak absorption this equation can also be written as

$$\alpha(\omega)z = \frac{I_0(\omega) - I(\omega)}{I_0(\omega)}. \tag{1.83}$$

Intensity detection is usually done by a photodetector onto which a laser power P generates a current equal to

$$i_{det} = \eta_c P = \eta_c \int I dA, \tag{1.84}$$

being $\eta_c[A/W]$ the photodiode's responsivity. Of course, current measurement is affected by noise coming from different sources, but its fundamental limit is coming from shot-noise. This noise can be explained by considering the quantum nature of light and the statistics of its arrival on the detector. In this way [12], the shot noise can be written as:

$$i_{shot} = \sqrt{2e\Delta f i_{det}}, \tag{1.85}$$

where e is the electron charge and Δf the detector's electronic bandwidth. However, shot noise limit is never reached by direct absorption spectrometry due to technical noise, also called Flicker noise, which has a $1/f$ frequency dependence and it dominates low frequencies where direct absorption spectrometry is performed.

1.3.1 Modulation techniques

Direct absorption spectroscopy is detecting signals at very low frequencies, precisely between $1/T_0$ and f_det, with T_0 the measurement time and f_det the maximum detection frequency. Since technical noises have a roughly $1/f$ frequency dependence, the detection sensibility is limited at low frequencies. This limitation can be easily overcome by shifting the detection to higher frequencies, something that can be achieve by modulation techniques.

When a probing light is frequency modulated, the sample response is encrypted at the same frequency (and its overtones) and, by applying demodulation techniques, this information can be reconstructed without any lost of details and gaining signal-to-noise ratio.

A frequency modulated light is generated by applying a time-dependent phase shift. The electric field of an electromagnetic wave, $E(t)$, at optical carrier frequency

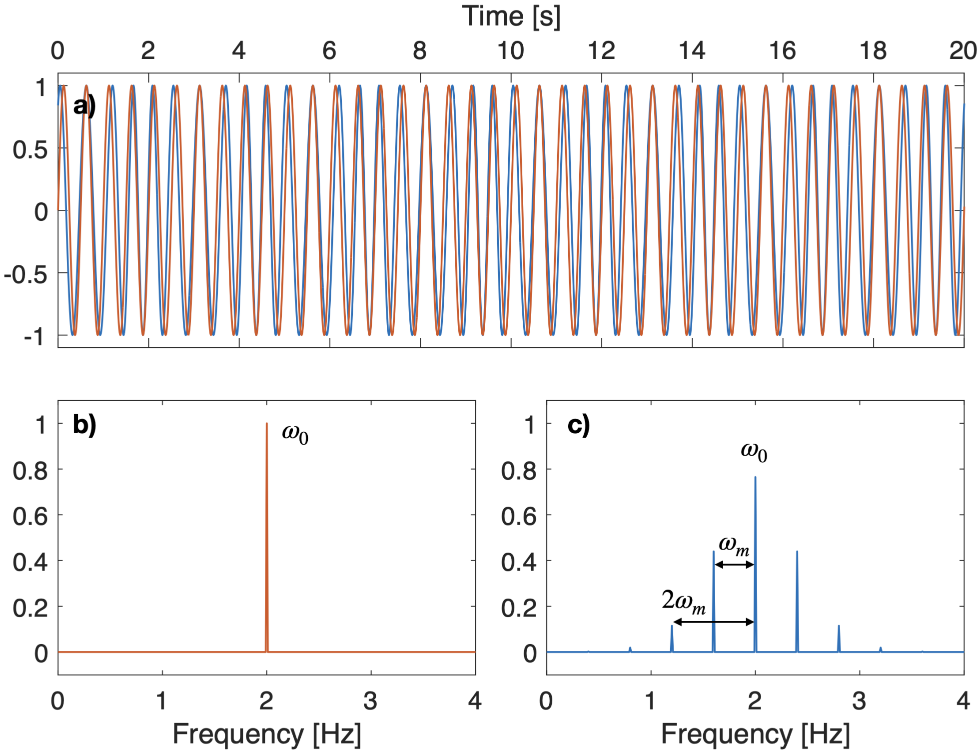

Figure 1.13: Modulated frequency. a) Unmodulated frequency at $\omega_0/2\pi = 2Hz$ in blue and modulated frequency with frequency modulation $\omega_m/2\pi = 0.4Hz$ with a modulation index of 1, in blue, as a function of time. b) Frequency spectrum of blue signal. c) Frequency spectrum of red signal.

ω_0 in presence of a sinusoidal modulation at frequency ω_m and with modulation index M is given by

$$\begin{aligned} E(t) &= E_0 \exp(i\omega_0 t + M \sin(\omega_m t)) \\ &= E_0 \exp(i\omega_0 t) \sum_{n=-\infty}^{+\infty} J_n(M) \exp(in\omega_m t), \end{aligned} \tag{1.86}$$

where J_n is the nth-order Bessel function [13]. Thus, the field consists of a carrier at frequency ω_0 and a series of sidebands of amplitude given by J_n separated from the carrier by an amount $n\omega_m$ (fig. 1.13).

The transmitted optical field through a sample can be expressed as [13]

$$E_T(t) = E_0 \exp(i\omega_0 t) \sum_{n=-\infty}^{+\infty} T(\omega_n) J_n(M) \exp(in\omega_m t), \tag{1.87}$$

where $T(\omega_n) = exp(-\delta_n - i\phi_n)$ is the effect of the sample at frequency ω_n, being δ_n the amplitude attenuation and ϕ_n the phase shift.

As long as there is no absorption or phase shift between laser carrier and modulation sidebands, the detector will not have a signal at the modulation frequency. If that is not the case, for example close to resonances of absorption or cavities, radio frequency power will appear in the detector's signal at the modulation frequency. By using an appropriate phase-sensitive detector, such as a lock-in amplifier of a frequency mixer, a signal at ω_m can be detected [13]

$$\begin{aligned} |E_{\omega_m(t)}|^2 = E_0^2 \Bigg(& J_0^2 \exp(-2\delta_0) + \sum_{n=-1}^{\infty} J_n^2 (\exp(-2\delta_n) + exp(-2\delta_{-n})) \\ & + 2\cos(\omega_m t) \sum_{n=0}^{\infty} J_n J_{n+1} \left[\exp(-2\delta_{-n})(\delta_{-n-1} - \delta_{-n}) \right. \\ & \left. + \exp(-2\delta_n)(\delta_n - \delta_{n+1}) + \exp(-2\delta_n) - \exp(-2\delta_{-n})\right] \\ & + 2\sin(\omega_m t) \sum_{n=0}^{\infty} J_n J_{n+1} \left[\exp(-2\delta_{-n})(\phi_{-n-1} - \phi_{-n}) \right. \\ & \left. + \exp(-2\delta_n)(\phi_{n+1} - \phi_n)\right] \Bigg). \end{aligned} \tag{1.88}$$

Assuming that the absorption and dispersion associated with the spectral transition of linewidth Γ are weak, so that $|\delta_0 - \delta_n \ll 1$ and $|\phi_0 - \phi_n| \ll 1$ eq.1.88 reduces to:

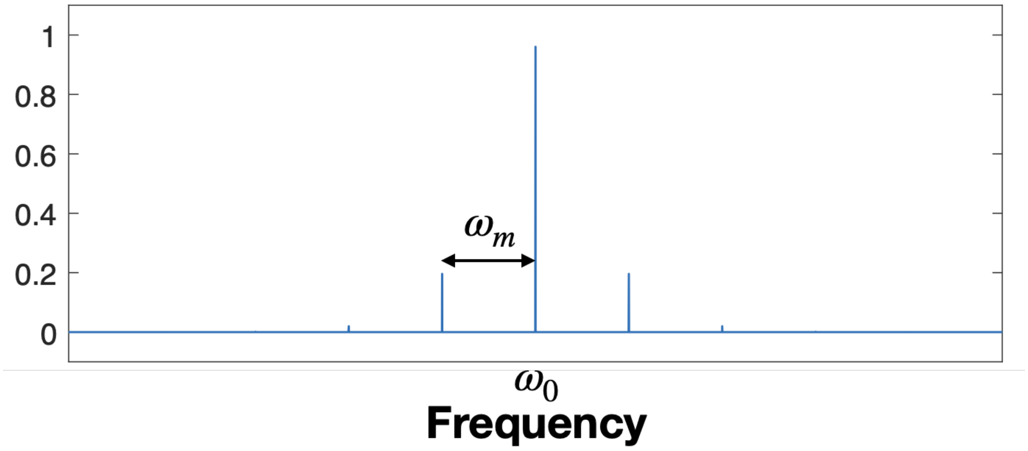

Figure 1.14: Frequency modulation. Carrier ω_0, modulation index $M = 0.4$, modulation frequency $\omega_m = 0.4\omega_0$.

$$|E_{\omega_m(t)}|^2 = E_0^2 \exp(-2\delta_0)\Bigg[1 + 2\cos(\omega_m t)\sum_{n=0}^{\infty} J_n J_{n+1}(\delta_{-n-1} - \delta_{n+1} + \delta_{-n} - \delta_{-n}) \\ + 2\sin(\omega_m t)\sum_{n=0}^{\infty} J_n J_{n+1}(\phi_{-n-1} - \phi_{-n} + \phi_{n+1} - \phi_n)\Bigg]. \quad (1.89)$$

This expression consists in a constant part and two time-varying contributions at ω_m. One component is sensitive to the absorption defined as out-phase term ($\cos \omega_m t$) and the other component is sensitive to the dispersion, which is defined as in-phase term ($\sin \omega_m t$).

Modulation techniques can be divided in two groups depending on the modulation index M. In the case of frequency modulation, the modulation index is small, $M < 1$, while for wavelength modulation the modulation index is large, $M >> 1$.

1.3.2 Frequency modulation

For frequency modulation [14], the modulation index is small and thus the light spectrum consists of a strong carrier and one set of sidebands $\omega_{\pm 1} = \omega_0 \pm \omega_m$. One of these sidebands occurs at higher frequency, in phase with the modulation, and the other at lower frequency with an opposite phase. Because M is small, the terms $J_n(M)$ are negligible for $n > 1$ [13] and the other terms can be expressed as $J_n(M) \approx M^n/2^n n$, so equation 1.89 becomes

$$\begin{aligned} |E_m^2(t)| = E_0^2 \exp(-2\delta_0)[1 + M(\delta_{-1} - \delta_1)\cos(\omega_m t + \psi) \\ + M(\phi_{-1} - \phi_1 - 2\phi_0)\sin(\omega_m t + \psi)]. \end{aligned} \quad (1.90)$$

By choosing the right phase, ψ, it is possible to select absorption signal, or the dispersion signal relative to the absorption line.

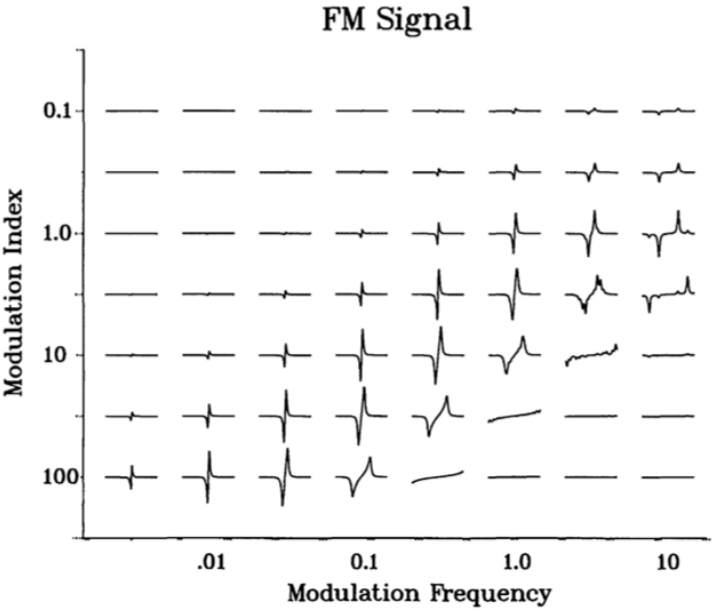

Figure 1.15: FM absorption signal for different combinations of modulation indices, M, and modulation frequencies ω_m. The signal is generated from an absorption with linewidth $\Gamma = 1$ [13].

The choice of modulation frequency, ω_m, and modulation index has to be chosen carefully depending on the laser noise and, more important, the resonance linewidth, Γ.

Keeping ω_m constant, the increase of M, shifts more power to the sidebands but for $M > 1$ it starts to create additional sidebands at $2\omega_m$, $3\omega_m$ and so on. Fig.1.15 shows how FM absorption signal changes in the case of a Lorentzian absorption of width $\Gamma = 1$.

Frequency discriminators are necessary in a feedback system controller, allowing to convert fluctuations in frequency to voltage signals that can be processed by electronics making use, for instance, of a Proportional Integrative Derivative (PID) controller.

It is also possible to use the carrier signal. In this case, the absorption signal is measured and a side of this feature can be used as a frequency discriminator. This choice presents different problems. First the error signal is recorded at DC, where amplitude noise is significant; then,amplitude noise of the laser directly couples into the error signal and the feedback loop can not distinguish from amplitude and frequency noise. Moreover, the narrow locking range presents another limitation.

Frequency modulation allows to overtake these problems. It enables to detect signals at high frequency were technical noise is lower and amplitude modulation can be neglected in first order. Also, signals have a high signal-to-noise ratio and a large acquisition range. All these characteristics allow a robust lock.

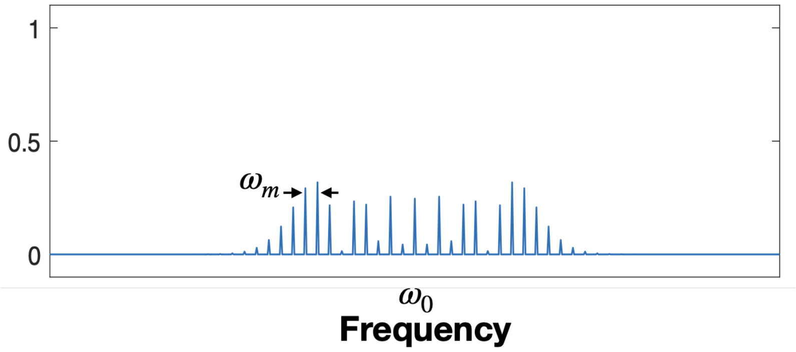

Figure 1.16: Wavelength modulation with carrier ω_0, modulation index $M = 10$ and modulation frequency $\omega_m = 0.001\omega_0$.

1.3.3 Wavelength modulation

Wavelength modulation is defined by a large modulation index $M >> 1$ and $M\omega_m < \Gamma$. In this case, side-band formalism used for frequency modulation is not convenient. Instead, it is better to describe wavelength modulation as a monochromatic wave whose frequency is modulated in time [13]. It is useful to define the instantaneous frequency as:

$$\omega_i(t) = \frac{d}{dt}(\omega_0 t + M\sin(\omega_m t)) = \omega_0 + \Delta F\cos(\omega_m t), \tag{1.91}$$

where $\Delta F = M\omega_m$ is the maximum frequency deviation. In this model, wavelength modulation is not carrying phase information about the analyte. This can be seen from eq.1.89 by assuming that adjacent sidebands experience the same difference in absorption and dispersion. In this way: $\delta_{n+1} - \delta_n = \Delta\delta(\omega_0)$ and the absorption term in eq.1.89 becomes:

$$\delta_{-n-1} - \delta_{n+1} + \delta_{-n} - \delta_n = -2(2n+1)\Delta\delta, \tag{1.92}$$

and the dispersion term, assuming $\phi_{n+1} - \phi_n = \Delta\phi$ is

$$\phi_{-n-1} - \phi_{-n} + \phi_{n+1} - \phi_n = 0, \tag{1.93}$$

providing that $\Delta F \ll \gamma$. Thus, eq.1.89 can be rewritten as:

$$|E_{\omega_m(t)}|^2 = -E_0^2 4\Delta\delta\sum_{n=0}^{\infty}(2n+1)J_n(M)J_{n+1}(M) = -2\Delta\delta(\omega_0)M. \tag{1.94}$$

The linearisation of the absorption profile $\delta(\omega)$ around ω_0 implies that $\Delta\delta = \omega_m d\delta/d\omega$ and so:

$$|E_{\omega_m(t)}|^2 = -E_0^2 2\left.\frac{d\delta}{d\omega}\right|_{\omega_0} M\omega_m. \tag{1.95}$$

Also the intensity of higher harmonic frequencies can by express as a function of absorption frequency derivatives. In this case, the n-th harmonic can be approximated by the n-th derivative (from here the name “derivative spectroscopy”). In addition, since the instantaneous frequency varies sinusoidally, the Taylor series is more or less automatically the Fourier series [13]. As a consequence, the detected signal of wavelength modulation spectroscopy can be expressed by the n-th Fourier coefficient of the absorption lineshape function.

If the assumption of $\Delta F < \Gamma$ is no longer valid, high order terms of absorption must be taken into consideration [13], but also dispersion signal starts to be measurable.

Chapter 2

Optical frequency comb

Almost all of the most precise and accurate measurements in physics are based on frequency due to the development of very precise frequency counters referenced to atomic clocks. In the past, in order to extend the range of applications of frequency counters from the radio-frequency domain to the optical domain, harmonic frequency chains were employed. At each step, a given frequency was multiplied by harmonic generation inside non-linear element, and phase-locked to the reference oscillator.

By repeating multiplication and phase-locking many times, it was possible to covert an atomic clock reference to higher frequencies [15]. Because of the difficulties related to keep the phase-locking along all the chain, it was not before 1995 when a visible laser light was first coherently referenced to a caesium atomic clock using this method [16]. In addition, these complex chains, which required a lot of space and instruments, were designed for a single particular frequency.

The advent of the optical frequency comb synthesizer [2][19] changed completely this pictures. The precise control of a mode-locked laser allows to relate its optical frequency to two radio frequencies, creating a direct bridge between optical domain to radio frequency domain.

Frequency combs revolutionised the field of metrology and spectroscopy, making possible, or easier, to transfer optical references from optical domain to radio-frequency domain and vice-versa, allowing precise and absolute measurements in any part of the electromagnetic spectrum.

2.1 Optical frequency comb synthesizer

The name optical frequency comb refers to a spectral structure of equidistant peaks all sharing the same phase dynamics (Fig. 2.1). Such a structure is represented in time by the Fourier components of a periodic waveform, a train of pulses. Its first and most common generation method relies on a mode-locked laser, a laser process that ensures a fix phase relation between different frequencies (or modes).

A mode-locking laser creates optical pulse trains with an electric field described by the convolution of an envelope function $A_0(t)$ with a series of periodic delta function, all oscillating around the carrier frequency ν_0 [20]:

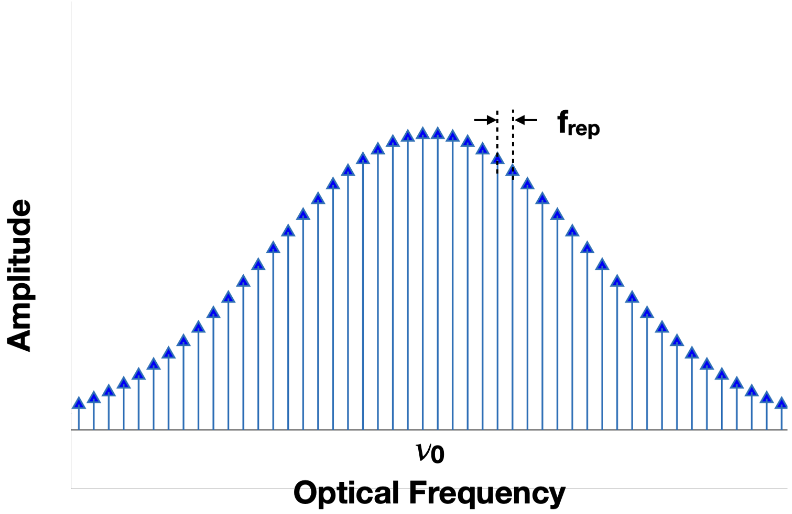

Figure 2.1: Frequency comb spectrum centred at ν_0 and with a repetition rate f_{rep}.

$$E(t) = \left[A_0(t) \sum_{m=-\infty}^{+\infty} \delta(t - mT)) \right] e^{i2\pi\nu_0 t}. \tag{2.1}$$

Its periodicity, T, is related to the cavity length L, through the effective refractive index n and speed of light, c, as

$$T = \frac{2nL}{c}. \tag{2.2}$$

Fig. 2.2.(a) shows the electric field of the generated pulse train as a function of time. In the spectral domain (Fig. 2.1) the same periodic structure appears as:

$$E(\nu) = \left[A_0(\nu - \nu_0) f_{\text{rep}} \sum_{k=-\infty}^{+\infty} \delta(\nu - \nu_0 - k f_{\text{rep}}) \right], \tag{2.3}$$

with a tooth separation of f_{rep} called repetition rate, which is precisely the free spectral range of the laser cavity

$$f_{\text{rep}} = \frac{1}{T}. \tag{2.4}$$

The centre of the spectrum is ν_0 and it can be defined as $\nu_0 = n_0 f_{\text{rep}} + f_{\text{CEO}}$ with the constrain that $0 \leq f_{\text{CEO}} \leq f_{\text{rep}}$. Thanks to this definition, the frequency comb spectrum can be written as:

$$E(\nu) = \left[A_0(\nu - \nu_0) f_{\text{rep}} \sum_{n=-\infty}^{+\infty} \delta(\nu - n f_{\text{rep}} - f_{\text{CEO}}) \right] = A_0(\nu_n - \nu_0), \tag{2.5}$$

where $\nu_n = n f_{\text{rep}} + f_{\text{CEO}}$. In this way, it possible to see a frequency comb as a precise series of mode all equidistant of f_{rep} and with an offset from 0 given by f_{CEO}. Also, f_{CEO} has a physical origin. It derives from the pulse to pulse phase slippage $\Delta\phi_{CEO}$.

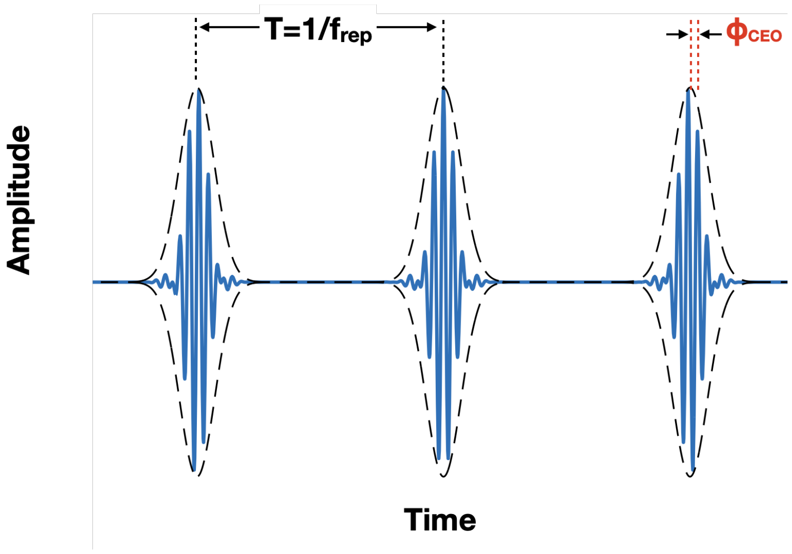

Figure 2.2: Time domain frequency comb with period T and pulse to pulse phase change ϕ_{CEO}.

Going back to the time comb equation, by taking two time instants separated by a pulse period T, t_m and t_{m-1}, their phase difference is

$$\Delta\phi_{CEO} = \phi_m - \phi m - 1 = 2\pi\nu_0 T = \frac{2\pi(n_0 f_{\text{rep}} + f_{\text{CEO}})}{f_{\text{rep}}} = \frac{2\pi f_{\text{CEO}}}{f_{\text{rep}}}. \tag{2.6}$$

Summarizing, the n-th order frequency comb mode is defined by two quantities f_{rep} and f_{CEO} like:

$$\nu_n = n f_{\text{rep}} + f_{\text{CEO}}. \tag{2.7}$$

The repetition rate, f_{rep}, can be easily measured and controlled. It can be detected by a fast photodiode and phase-locked to a radio frequency reference. In alternative, it is possible to generate a beatnote signal between one comb mode, N, and a narrow linewidth CW laser at ν_{CW}. This beatnote can be stabilised via active feedback and, as consequence, the repetition frequency results stabilized at $f_{\text{rep}} = (\nu_{CW} + \nu_{CEO})/N$.

Tuning the f_{CEO} parameter is not trivial and it requires a precise mismatching between group velocity and phase velocity. A common solution is to measure it and closing a control loop over the intracavity laser power.

In most of the cases f_{CEO} is measured by self-referencing [21][22]. This method (Fig. 2.3) is based on the generation of an octave spanning frequency comb spectrum by non-linear broadening. Then, by frequency doubling the comb modes at lower frequency and combining them with the higher part of the spectrum, it is possible to obtain:

$$2\nu_n - \nu_{2n} = [2(n f_{\text{rep}} + f_{\text{CEO}})] - [2n f_{\text{rep}} + f_{\text{CEO}}] = f_{\text{CEO}}. \tag{2.8}$$

The resulted beatote correspond exactly to the carrier-envelop offset frequency. It is possible to measure f_{CEO} without ocatve spanning frequency comb but it requires higher-order non-linearities [23].

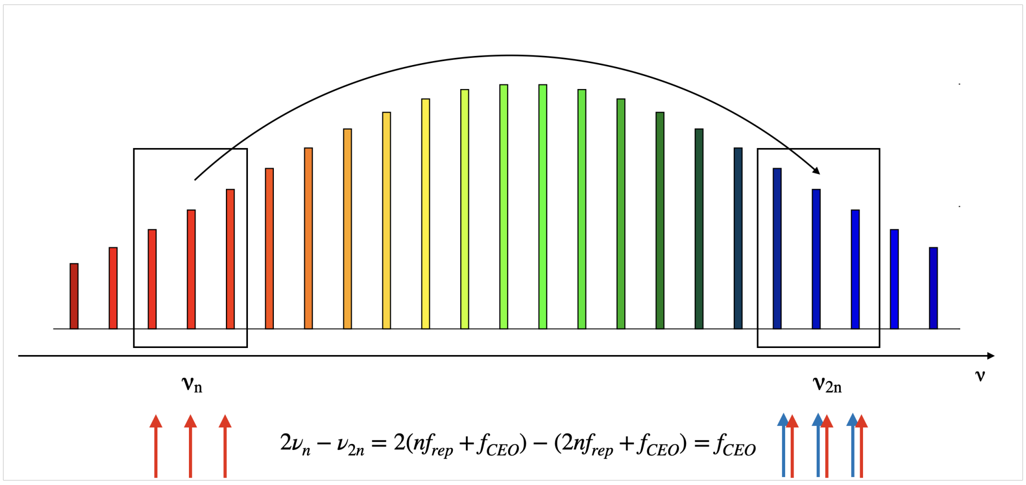

Figure 2.3: CEO frequency detection principle. Red side (low frequency) of the spectrum is frequency doubled and compared with blue part (high frequency). The beatnote between the two is equal to f_{CEO}.

2.2 Frequency comb sources

The growing number of applications with optical frequency combs resulted in a growing interest in developing new laser sources or revisiting existing ones with focus on creating a fully stabilised frequency comb.

Frequency comb technology started and founded a full development in the near-infrared spectral region (800nm - 2μm) with mode-locking laser. Ti:Sapphire lasers have been the first ones demonstrating a spectral broadening larger than the octave necessary to achieve self-referencing [24]. After this first demonstration, the full maturity in this spectral region has been possible due to the rapid development of fiber laser technology, especially in the telecommunication region at 1.5 μm. Mode-locked fiber lasers doped with ytterbium, erbium, thulium or holmium are now commercially available with a wide range of performance, in terms of power, repetition rate, compactness, price.

In the near-infrared spectral region, different technologies are being tested at a research level. Soliton Kerr combs in high quality microresonators have demonstrated the octave covering [25]. The microresonator is constituted by a ring or disk of sub-millimeter diameter which balances loss and gain in an active media, along with nonlinearity and dispersion. In these systems, which are pumped by a strong electromagnetic field, the third-order nonlinearity generates optical sidebands by four-wave mixing processes, that can again generate other sidebands by four-wave mixing. This cascade and coherent process brings to the generation of a train of pulses. Thanks to the high finesse of the resonators, the threshold power can be particularly low if all fields involved are resonant with the cavity mode. This solution allows to generate repetition rates from 10 GHz to 1 THz, being difficult or even impossible to achieve by mode-locked lasers. Moreover, they demonstrated the possibility of integrating an optical frequency comb on a chip [26].

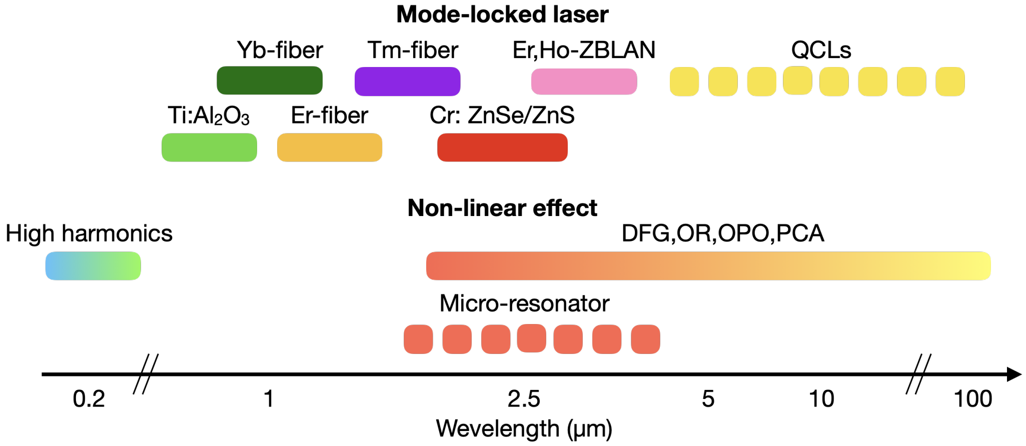

Figure 2.4: State of the art of optical frequency comb. Graphical representation of available technology for each spectral window.

Other solutions demonstrated a potential for integration, such as III–V-on-Si mode-locked lasers [27]. An alternative generation process relies on generating a train of pulses thanks to fast electro-optic modulators (frequency-agile combs [28][29]). They exhibit flat-top spectra with a small bandwidth but a freely selectable line spacing and a central frequency that can be rapidly tuned.

Mid-infrared frequency combs (2-20 μm) are not technologically mature [30]. Direct generation from fiber or bulk laser sources is recent and limited. They are based on chromium doped chalcogenide crystals like ZnSe [31] or ZnS [32]. Other femtosecond lasers have been demonstrated but a full stabilisation was not achieved. Interesting performance has been obtained from Er^{3+} and Ho^{3+} doped fluoride fibers. Femtosecond laser operation was successfully demonstrated [33][34] but not self-referencing.

One of the most common approaches is, instead, frequency downconversion by non-linear processes from visible and near infrared frequency combs. Difference frequency generation has been explored with different configurations. It is possible to mix a frequency comb with a continuous wave laser inside a nonlinear crystal [35][36]. Alternatively, difference frequency generation can be obtained by combining two parts of the same frequency comb using periodically poled lithium niobate as a nonlinear medium [37][38], up to 5 μm, or gallium selenide for longer wavelengths(up to 17 μm) [39][40]. Novel materials are also emerging [41]. Difference frequency generation solutions inherit the repetition frequency from the starting frequency comb and they offer an inefficient power conversion and a bandwidth limited by phase matching conditions. A way to boost efficiency is to use optical parametric oscillators pumped by a femtosecond laser [42] [43]. In this way, it is possible to obtain higher power per mode by adding an optical resonator and controlling round-trip dispersion.

A more integrated option is provided by quantum cascade [44] and interband [45] cascade laser frequency combs, that can produce 100-200 comb lines with gigahertz line spacing. However, they can be designed to work with a central frequency anywhere between 3 and 9 μm. Microresonators and waveguides generate or broaden mid-infrared spectra, with on-chip silicon or silicon nitride platforms [26].

Far-infrared and terahertz regions (20 μm - 1 mm) have been, for a long time, generated only by non-linear frequency conversion starting from near-infrared frequency combs. The two main generation processes involve photomixing in photoconductive antennas [46] or optical rectification in crystals [47]. Both of these processes produce frequency combs with the same line spacing of the near-infrared used to generate them and their power is usually limited to few microwatts. In the recent years, an improvement in performance has been possible due to the design of photoconductive emitters with plasmonic enhancement [48]. An alternative solution to access this spectral region is the use of terahertz quantum-cascade frequency comb lasers [49]. High power, electrically pumped, and versatile wavelength are the key advantages of this kind of source. The generation by four-wave mixing is usually limited at few hundreds of phase-coherent lines, but it has been demonstrated the possibility to reach a bandwidth closer to the octave by a careful design of the dispersion compensation.

Visible and near-ultraviolet frequency combs are usually generated starting from near-infrared frequency combs. The process involves harmonic- or sum- frequency generation in non-linear crystals or spectral broadening in non linear waveguides or fibers. In this way, it is possible to generate frequency combs down to 200 nm. Reaching shorter wavelengths requires high-harmonic-generation in rare gas, a process with a very low efficiency. Due to the low efficiency and the high intensity required for this process, an enhancement cavity is needed for applications with high repetition rate. This approach increases system complexity and requires a phase-matching optimisation, in order to build up harmonic generation along all the interaction length [50][51].

2.3 Frequency comb spectroscopy

The advent of frequency combs revolutionised the measurement of frequency and time by providing a direct link between optical and radio-frequency domains. Starting from precision spectroscopy of atoms like hydrogen, frequency comb spectroscopy started to become a very important tool, allowing not only high precision measurements. It is a broadband source easy to calibrate. It can ensure negligible instrumental line shape contribution to the recorded spectra. It can be generated by ultra-short pulses, essential non-linear processes or to record very fast dynamics. Because of the high coherence of this source, it generates spectra with a better signal-to-noise ratio and it can reduce measurement time.

Many different techniques have been developed to exploit at the best a frequency comb source. All of them can be grouped in two main category. “Comb assisted spectroscopy”, where the frequency comb is used as a supporting absolute frequency reference, and “direct comb spectroscopy”, in which the comb is used as probing beam.

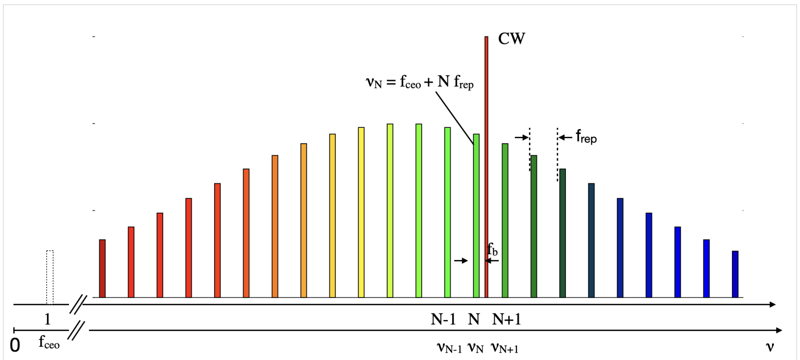

Figure 2.5: Comb assisted spectroscopy principle. A CW laser frequency beats with the closed comb mode, f_{beat}. $\nu_{CW} = nf_{\text{rep}} + f_{CEP} \pm f_{beat}$.

2.3.1 Comb assisted spectroscopy: absolute frequency determination

Optical frequency combs provide an accurate and precise link between optical and microwave frequencies [24][52]. Thanks to this, a simple way to perform high precision spectroscopy is to use the optical frequency comb as a frequency ruler to measure an unknown frequency referencing it to a frequency standard [53]. An unknown frequency of a continuous wave laser ν_1 can be measured by detecting the beatnote with a frequency comb [54] as:

$$\nu_1 = \nu_{comb} \pm f_{beat} = nf_{\text{rep}} + f_{\text{CEO}} \pm f_{beat}. \tag{2.9}$$

Once the frequency comb is stabilized, f_{rep} and f_{CEO} are known. The beatnote can be measured by a photodetector and the sign can be identified by applying a small change in one of the known frequencies and identifying if the beatnote increases or decreases. The order n of the comb line can be determined by a coarse measurement of ν_1, for example with a wavemeter. It is enough that the precision of this coarse measurement is better than half of the repetition frequency of the optical frequency comb. Alternatively, it is possible to measure the variation of the beatnote frequency after a small variation of the repetition frequency, according to: $\Delta f_{beat} = n\delta f_{\text{rep}}$ and as a consequence $n = \Delta f_{beat}/\delta f_{\text{rep}}$.

Absolute frequency scanning are possible after referencing the CW laser to a frequency comb. If the CW laser frequency is controlled by feedback or feed-forward loop, it is possible to tune it in an absolute way by changing one of the parameter of the frequency comb. According to Eq. 2.9, the CW laser frequency variation can be expressed as

$$\Delta\nu_1 = n\Delta f_{\text{rep}} + \Delta f_{\text{CEO}} \pm \Delta f_{beat}. \tag{2.10}$$

It is possible to modify f_{CEO} or f_{beat} and, in this way, having a one-to-one tuning. Alternatively, it is possible to change f_{rep} and exploit the lever mechanism related to n, obtaining a 1:n tuning. If necessary, another possibility given by this approach is to phase-lock the continuous wave laser to the optical frequency comb. In this way, it is possible to transfer the frequency stability from the latter to the former.

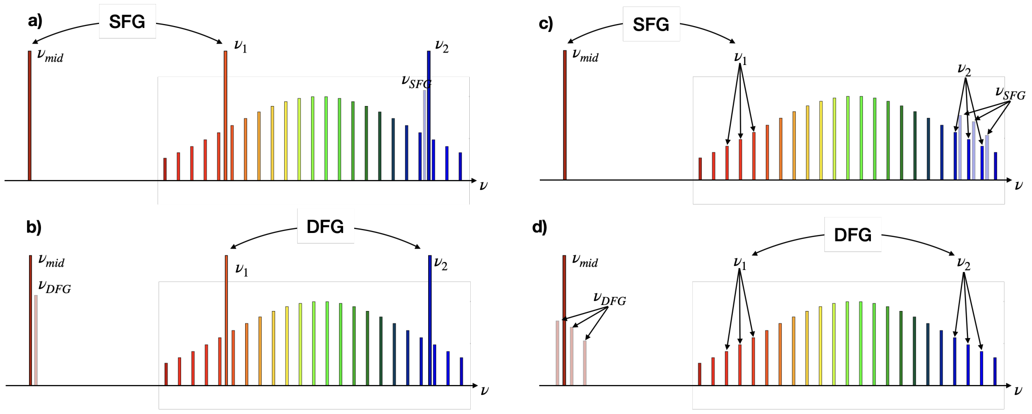

Figure 2.6: Comb assisted spectroscopy in mid-infrared. a) SFG mediated by CW laser; b) DFG mediated by CW laser;c) direct link with SFG comb; d) direct link with DFG comb.

This is very useful, especially when the CW laser is a semiconductor device, and it presents a free running linewidth of some megahertz.

Frequency combs were initially conceived for precision spectroscopy of the hydrogen atom in which it reached its best accuracy at the level of 10^{-15} [55]. However, they are now commonly used for precise frequency measurements of atomic resonances and molecular ro-vibronic transitions throughout all the spectral regions. It is in the mid-infrared where frequency comb spectroscopy offers the major number of opportunities thanks to the presence of strong ro-vibrational transitions for a large number of molecules. Moreover, because of the precise measurement of energy levels, precision spectroscopy in mid-infrared allows to test fundamental physical laws and to improve precision in the determination of fundamental constants, as well as to test their possible low variations.

Direct mid-infrared generation of frequency combs does not reach the accuracy level of the visible and near-infrared ones. To overtake this limitation, the easiest way consists of using non-linear optics to link a mid-infrared laser beam, ν_{mid}, to a visible/near-infrared frequency comb. Fig. 2.6 summarises the possibilities for this non-linear link. A first approach makes use of two addition CW lasers in the infrared, ν_1 and ν_2, whose frequency difference coincides with the mid-infrared laser, $\nu_{mid} = \nu_1 - \nu_2$. Both these lasers can be referenced to a frequency comb in order that $\nu_{1,2} = f_{\mathrm{CEO}} + n_{1,2} f_{\mathrm{rep}} + \Delta f_{1,2}$. At this point, the non-linear link can be performed by sum frequency generation [56], SFG, or difference frequency generation [37], DFG. In the first case, $\nu_{SFG} = \nu_{mid} + \nu_1$ and it is possible to detect a beatnote with ν_2 according to $f_{beat} = |\nu_2 - \nu_{SFG}| = |\nu_{mid} - (n_2 - n_1) f_{\mathrm{rep}}|$. In the second case, $\nu_{DFG} = |\nu_2 - \nu_1|$ and the beatnote is $f_{beat} = |\nu_{mid} - \nu_{DFG}| = |\nu_{mid} - (n_2 - n_1) f_{\mathrm{rep}}|$. Both approaches lead to the absolute determination of mid-infrared laser frequency given by

$$\nu_{mid} = |(n_2 - n_1) f_{\mathrm{rep}} \pm f_{beat}|. \tag{2.11}$$

It is also possible to avoid the use of two additional single frequency lasers. In this case, the SFG or DFG can be directly done with a portion of the near-

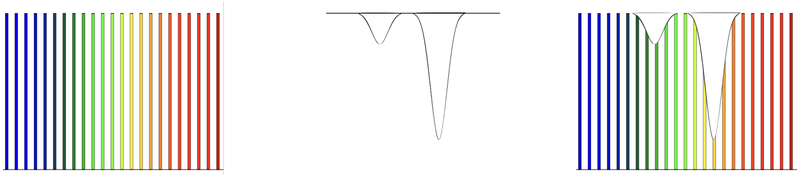

Figure 2.7: Direct comb spectroscopy scheme. A frequency comb is interacting with a sample.The spectrum can be retrieved by the power change of each mode.

infrared frequency comb. The two non-linear processes generate a shifted version of the starting frequency comb, however the beatnote detection leads to the same result as for the previous cases $f_{beat} = |\nu_{mid} - (n_2 - n_1)f_{\text{rep}}|$. Both of these second configurations need an additional delay line in order to synchronise the arrival of the pulses at the photodetector, in the SFG case, or at the non-linear crystal for DFG.

DFG and SFG approaches lead to similar performances in terms of optical power and beatnote signal. SFG has advantages in detection, since the beatnote recording is performed in the near-infrared where detectors present better performance in terms of noise and bandwidth. Instead, DFG has the advantage of removing, virtually, any noise contributions from the frequency comb. Using intermediate CW lasers increases system complexity, costs and the need of additional servo controls. However, the possibility of having high power lasers helps to get high signal to noise ratio beatnote.

2.3.2 Direct comb spectroscopy

Direct comb spectroscopy [17] is characterised by the use of the frequency comb as a probing beam (Fig. 2.7). Starting from this concept, many different techniques can be implemented. The easier configuration is a linear spectroscopy with a single comb line resonant with a transition [57] and all the other frequency comb modes detuned from this resonance. The absolute frequency can be determined by measuring the repetition frequency, the carrier envelop offset frequency and a coarse frequency estimation of the comb line in resonance with the transitions (with a precision better than half repetition frequency). The response of the sample can be measured with a single detector, and a scan of the spectrum can be obtained by changing one of the two parameters of the frequency comb, for example, the carrier envelop offset frequency. The same experiment can be executed in a Doppler-free configuration by using two counter-propagating beams for the excitation. Two photon excitation experiments [17] can be done with the same single detector approach. In this case, there are many pairs of comb lines with the same sum frequency which are contributing to the excitation. Since only one frequency can be resonant with the sample, this first group of techniques can be used for sparse spectra with very narrow lines, like gas-phase atomic systems. However, in comparison with a CW laser, direct comb spectroscopy brings some advantages like an intrinsic reference to a frequency standard or related to the use of ultrashort pulses, especially for non-linear processes.

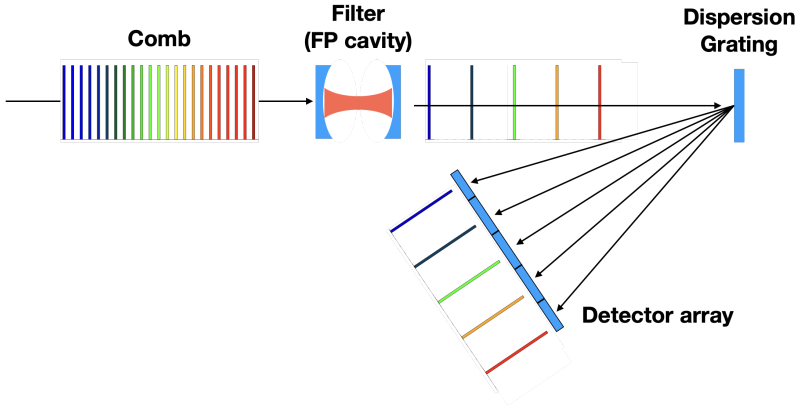

Figure 2.8: Direct comb spectroscopy by dispersion. In this case, the dispersion element is a grating. Since its resolving power does not allow to resolve single comb modes, a Fabry-Perot cavity is used as a tunable filter to artificially increase the comb line spacing. The detection is performed by an array of detectors.

From this first example, it is clear that direct comb spectroscopy can offer much more than a single frequency detection. Indeed, it is possible to combine spectrometers to direct frequency comb. In this way, parallel detection over the entire bandwidth of a frequency comb is achievable. However, in order to obtain the absolute calibration of the spectrum, single comb line detection must be achieved. This requires a spectrometer resolution better than the repetition rate.

Dispersion spectrometers are simple and robust tools for multichannel parallel acquisition for broadband direct frequency comb spectroscopy. Gratings and crossed dispersers, like virtual imaging phase array étalons, have been successfully implemented but resolutions as high as 600 MHz have been reported [58]. This allows to resolve single comb lines only for chip based devices with high repetition rates. Alternatively, a Fabry–Pérot cavity can be used to increase artificially comb line spacing by filtering only some of them. This allows to relax the resolution requirements for the spectrometer (Fig. 2.8). Vernier techniques [59] match cavity free spectral range with frequency comb line spacing with a ratio $m/(m-1)$ being m an integer. An alternative method, which does not require a relative match between free spectral range and comb repetition rate, is characterised by the use of a scanning high finesse micro-cavity [8]. However, it must be designed with a free spectral range much larger but with a resonance smaller than the comb repetition rate. Due to this, only few comb lines are resonant with the cavity and a low dispersion spectrometer is sufficient for the detection. Moreover, the same cavities can be used for the enhancing interaction length in order to increase the response of weak absorbing samples.

An alternative type of spectrometer is based on interference and Fourier transform (Fig. 2.9). Michelson interferometers [60] have been one of the most profitable spectroscopic instruments over the last 50 years, in any spectral region and for any spectral data. The performance of this instrument is related only to the moving arm. In particular, the resolution, $\delta\nu$, is limited by the maximum excursion of the moving

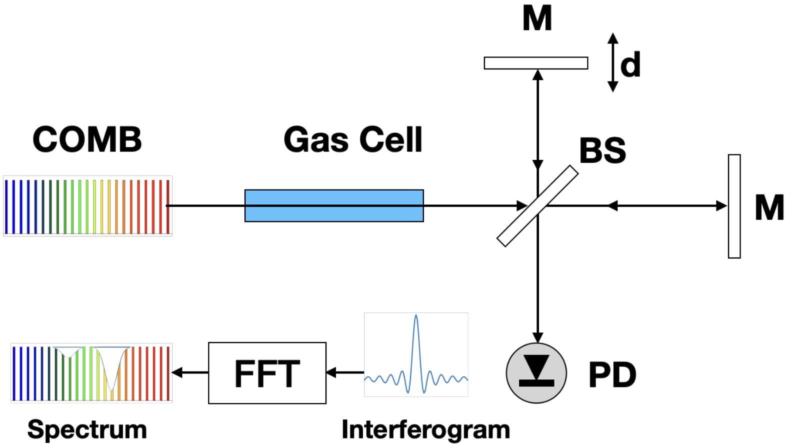

Figure 2.9: Direct comb spectroscopy by Fourier transform. Frequency comb is sent to a Michelson interferometer with a moving mirror. Time trace is recorded by a photodetector, PD, and after Fourier transform, the comb spectrum is retrieved.

arm, d, such that $\delta\nu = d/c$, and the frequency bandwidth is down-converted from optical domain to radio-frequency domain with a factor v/c, where v is the mirror speed and c the speed of light. This means that, in order to achieve high resolution and high bandwidth, the instrument is usually bulky and slow. The use of frequency comb as a source of Michelson interferometers has been demonstrated to bring significant improvements [61]. A coherent source has higher brightness compared to incoherent lamps, leading to increased signal-to-noise ratio or decreased measurement times. If the single comb mode is resolved, the instrumental line-shapes can be neglected. Frequency scale calibration can be done due to the measurement of the repetition frequency and offset frequency. The absolute frequency assignment can be done using a reference, like a known CW laser or a known absorption profile. As a final consideration, both absorption an dispersion spectra can be measured [61].

With frequency combs, a new kind of interference spectrometer has been realised, the dual-comb interferometer [62]. Two mutually coherent frequency combs with a slightly different repetition rate, a sampling comb and a local oscillator, are combined on a photodetector to create an interference signal (Fig. 2.10). This approach is logically similar to a Michelson interferometer but it does not require any moving part.

In the time domain, due to the different repetition rate, a pair of pulses from the two frequency combs arrive on the detector with automatically increasing delay, a delay $\delta f_{\mathrm{rep}}/f_{\mathrm{rep}}^2$ from one pulse pair to the other pulse pair. The result is an interferogram stretched in time by a factor $f_{\mathrm{rep}}/\delta f_{\mathrm{rep}}$. In this way, optical delays between 0 and$1/f_{\mathrm{rep}}$ are periodically scanned. In the frequency domain, the difference in repetition rate results in two frequency combs with a different line spacing. When these two are combined at the photodetector, the result are beatnotes between different pairs of comb lines. This series of beatnotes represents the down-converted version of the sampling comb, with a new line spacing given by the difference in repetition frequency.

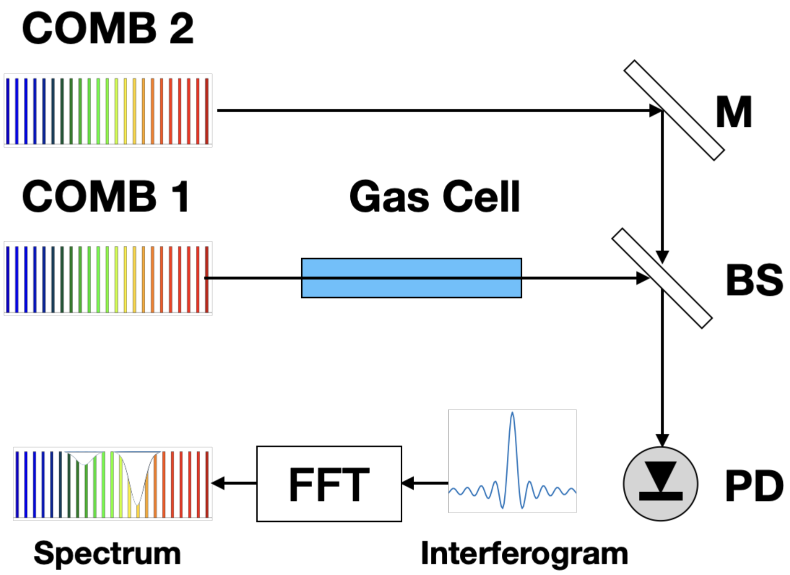

Figure 2.10: Direct comb spectroscopy by dual-comb. COMB1 at f_{rep1} interacts with the sample and it beats with COMB2 at f_{rep2}. The beating is recorded by a photodetector, PD, and by Fourier transform the comb spectrum is retrieved.

A fundamental difference with Michelson interferometer is that the resolution is not limited by the geometry but only by time. This makes dual-comb spectroscopy the only technique able to resolve single comb lines for any kind of bandwidth and repetition frequency. The challenge to apply this technique is the temporal coherence between two frequency combs. The widely adopted technique in frequency metrology to reference the comb to a radio-frequency clock does not provide the required short-term relative stability. Different techniques have been designed to overtake this problem. Feed-back control to narrow-line-width CW lasers [63], feed-forward control of the relative carrier–envelope offset frequency [64], fluctuation tracking and analog [65] or digital [66] processing are solutions to control the relative fluctuations of two independent sources. Alternatively, it is possible to design dual-comb systems with built-in passive mutual coherence (dual-wavelength unidirectional mode-locked lasers [67], bidirectional mode-locked lasers [68], micro-resonators [69], electro optic modulators [70]).

Chapter 3

Comb-assisted Doppler-free spectroscopy of CHF_3

Comb assisted spectroscopy allows to perform high-resolution spectroscopy always referenced to a frequency standard. In this experiment, a quantum cascade laser (QCL) emitting around 8.6 μm is used to probe a gas molecule, the fluoroform (CHF_3), in order to measure with high precision and accuracy its absorption spectrum. In this chapter, after a brief introduction to this molecule, experimental results about direct and wavelength modulated Doppler-free absorption spectroscopy are going to be presented. High resolution spectroscopy of fluoroform represents the first step towards a new test of constancy of a physical quantity, the proton-electron mass ratio [5].

3.1 Fluoroform CHF_3

Fluoroform is a molecule belonging to the class of “holoforms ”, chemical compounds with a general formula of CHX_3 being X an halogen atom. In particular, fluoroform is the lightest of these compounds, using a fluorine (F) as a halogen atom.

This molecule has been identified as a candidate target to investigate the proton-electron mass ratio, $\beta = m_p/m_e$, [5] a constant that links the strength of the strong

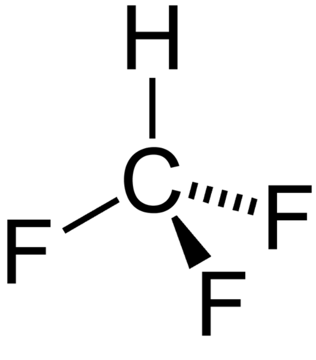

Figure 3.1: Structure of a fluoroform molecule.

interaction with the electro-weak one. A possible method to measure β is by measuring the line centre frequency of a roto-vibrational transition in comparison with the time standard (the hyperfine transition in the Cs electronic ground state at rest at 0 K). The proposed experiment uses a Ramsey-fringes technique on a slow molecular beam at a low rotational temperature for a sub-Doppler spectroscopy experiment, a two-photon spectroscopy. This molecular beam can be obtained by combining buffer-gas cooling and Stark manipulation. While buffer cooling can work with any kind of molecule, Stark manipulation requires a high electric dipole moment. Taking all this in consideration, CHF_3 results in a suitable candidate for this experiment, since it presents a high electric dipole moment, μ =1,67 Debye, and it shows a fundamental and strong ro-vibrational band (CF_3) degenerate stretch, (ν_5) at 8.6 μm (1158.75 cm^{-1}).

Fluoroform spectroscopic parameters, such as line position or line strength, were known in literature with a poor resolution [71]. It was only in 2018 that the first high resolution Fourier transform spectroscopy experiment was performed, with the best resolution of 0.001 cm^{-1} (30 MHz) [72].

With the idea of improving the state of the art of line centre frequencies in the spectral region around 8.6 μm, it is performed a saturated absorption spectroscopy experiment, by using a QCL assisted by an optical frequency comb.

3.2 Doppler-free comb assisted spectroscopy of CHF_3

Saturation spectroscopy can be a powerful tool for precise measurements of line centre frequencies. As it is presented in section 1.2, there is a possibility to burn a hole in to the Doppler-broadened absorption. This narrow dip allows to determine the line centre frequency of the transition with more precision. Moreover, it allows to distinguish the different transition that can be present inside the same Doppler broadened profile.

3.2.1 Experimental setup

The experimental setup for Doppler-free comb assisted spectroscopy of CHF_3 [73] is presented in Fig. 3.2.

The probing beam for the experiment is a Quantum Cascade Laser (QCL) emitting from 1155 cm^{-1} to 1160 cm^{-1} (34.68 - 34.80 THz), with 50 mW of maximum optical power and 2 MHz linewidth.

After passing through a 30 dB optical isolator, the QCL output power split by a 50/50 beam splitter. The transmission, pump beam , is coupled to a a 25 cm long cell filled with CHF_3 gas (98% purity) at few Pascals of pressure. The beam waist diameter at the middle of the cell has been measured within 2.1 mm by a CCD infrared camera. A second 50/50 beam splitter (BS_2) reflects a part of the cell transmission to a liquid-nitrogen-cooled HgCdTe (MCT) detector (1-MHz electrical bandwidth), PD_{lin}, to record the single-pass absorption. The transmission from BS_2

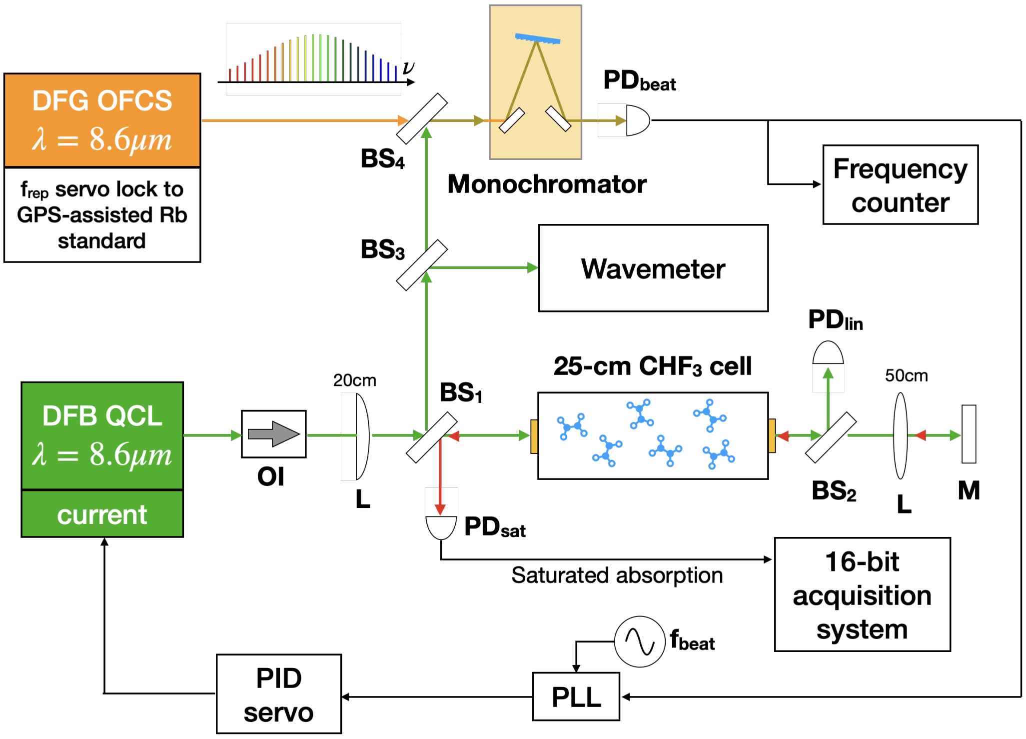

Figure 3.2: Experimental setup for Doppler-free spectroscopy of CHF_3 at 8.6 μm. DFB QCL:distributed feedback quantum cascade laser; DFG OFC: difference-frequency-generation optical frequency comb; M: mirror; BS: beam splitter; L: lens; OI: optical isolator; PD: photodetectors; PID: proportional-integrative-derivative servo; PLL phase locked loop.

is reflected back to the cell and, by superimposing it to the pump, it generates the saturation profile. The phase fronts have been matched by using a 50 mm lens before the mirror, its measured probe beam waist diameter is 1.8 mm. After interacting with the sample, the probe beam is reflected by BS_1 onto a four-stage thermo-electrically cooled MCT detector (50 MHz bandwidth), PD_{sat}, in order to detect the saturated absorption signal.

To precisely measure and control the QCL emission frequency, the first reflection of BS_1 is combined to a Difference Frequency Generation Optical Frequency Comb (DFG-OFC) at 8.6 μm with a radio-frequency stabilized repetition frequency. The radio frequency reference is a GPS-disciplined Rb clock with a fractional stability (1-s Allan deviation) and accuracy of 8×10^{-12} and 10^{-13}, respectively.

After filtering by means of a 0.01 μm monochromator, the combined beams are focused in a 200 MHz bandwidth MCT detector, PD_{beat}, ($5.7 \cdot 10^4$ V/W responsivity and 50 nV/pHz noise floor at a temperature of 77 K). This beatnote is stabilized at 70 MHz against a frequency synthesizer through a phase-detector. The signal is then fed to a proportional-integrative-derivative (PID) servo controller which acts on the QCL driving current.

3.2.2 Quantum cascade laser

The development of QCLs allowed a new and easier access to mid-infrared (3-15 μm) spectral region. They provide a tunable single frequency laser source with a modest/high power and narrow linewidth [74][75].

A commercial single spatial mode and single longitudinal mode Distributed Feedback Quantum Cascade Laser (DFB-QCL or QCL) emitting at 8.6 μm is used in this experiment. The DFB-QCL operates at room temperature (thermally controlled at mK level stability) with a maximum output power of 50 mW. This source is tunable in power and wavelength by changing injected current and working temperature. A commercial current driver has been employed. It provides a low-noise current (3 nA/$\sqrt{Hz}$) and 2 MHz modulation bandwidth.

The laser linewidth can be retrieved from the frequency noise power spectral density [76]. By defining the β-line as $8\ln(2)f/\pi^2$, the laser linewidth at full width at half maximum, FWHM, can be calculated as the integral from $1/T_0$, with T_0 the measurement time, to the β-line of the frequency noise power spectral density $S_{\delta\nu}(f)$, so that

$$\mathrm{FWHM} = \sqrt{8\ln(2)A}, \tag{3.1}$$

with

$$A = \int_{1/T_0}^{\infty} H\left(S_{\delta\nu}(f) - 8\ln(2)f/\pi^2\right) S_{\delta\nu}(f)df, \tag{3.2}$$

and $H(x)$ the Heaviside unit step function ($H(x) = 1$ for $x > 0$ and $H(x) = 0$ for $x < 0$).

The frequency noise is obtained by converting an intensity noise measurement with an amplitude to frequency discriminator. If $S_{\delta\nu}(f)$ is the power spectral density of frequency noise [Hz^2/Hz], it can be converted in power spectral density of

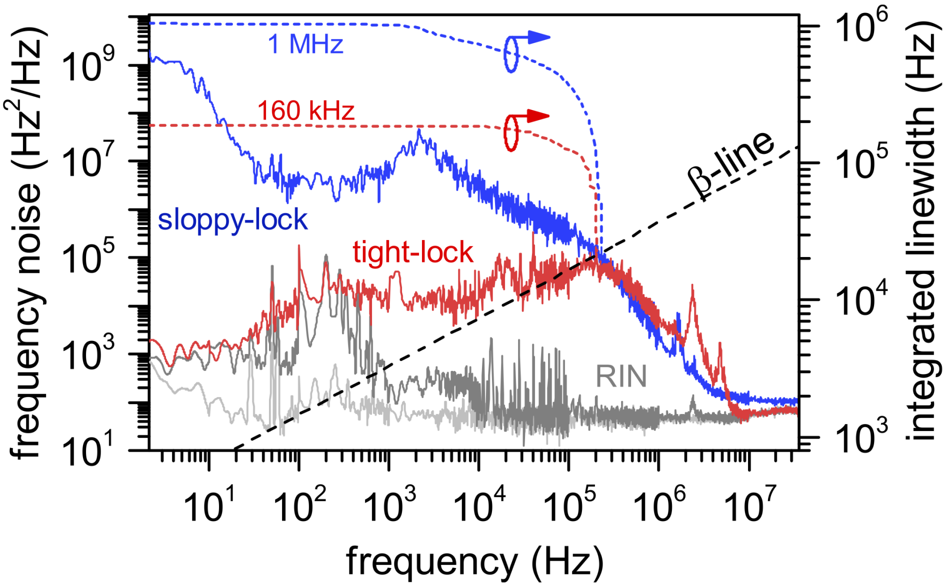

Figure 3.3: Right axis: frequency noise PSD of the QCL laser in sloppy-lock (blue) and in tight-locked (red line) conditions together with the RIN contribution (dark grey), the noise floor (light grey), and the β-line, $8 \ln 2\pi 2f$(dashed black). Left axis: calculated emission linewidth versus integration bandwidth.

amplitude $S_I(f)$ [V^2/Hz] by a slope, D [V/Hz], as

$$S_{\delta\nu}(f) = \frac{S_I(f)}{D^2}. \tag{3.3}$$

Attention has to be paid to the detector noise floor and the relative intensity noise (RIN) of the laser (power spectral density over average power). It is possible that one of these two noise sources can overcome the converted frequency noise. In this case, the measurement can only set an upper limit for the laser linewidth.

For this experiment, the used discriminator is the slope of an absorption line of the CHF_3. The laser is interacting with the gas sample and the transmission is recorded with a photodetector. Then, the signal is analysed by an electric spectrum analyser to retrieve the intensity noise.

Fig. 3.3 shows the measured power spectral densities of the QCL with relative RIN and noise floor. From these measurements a linewidth of 1 MHz can be inferred.

3.2.3 Difference frequency generation optical frequency comb

The self-referenced optical frequency comb at around 8.6 μm is synthesized by a difference frequency generation process (DFG) [77]. This generation approach presents different advantages in the mid-IR spectral region. First, it creates an harmonic frequency comb due to the cancellation of the CEO frequency. Moreover, all the

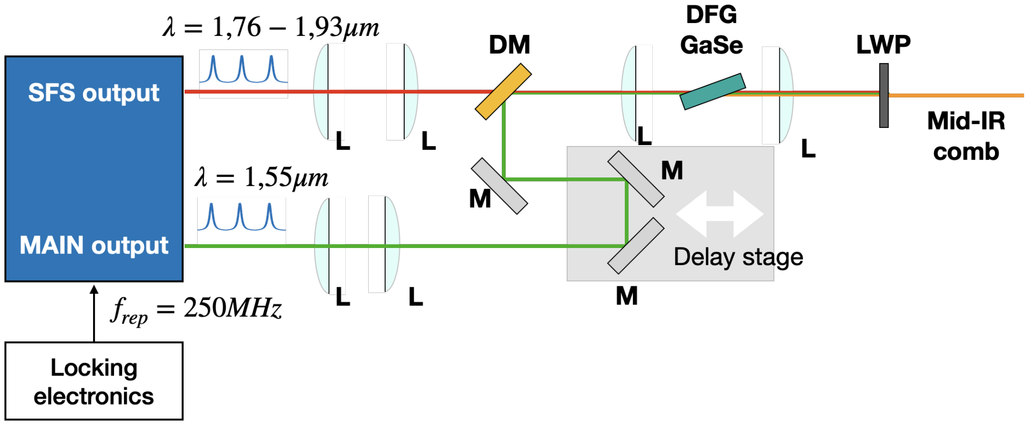

Figure 3.4: Difference frequency generation frequency comb setup: SFS self-frequency shiftet soliton; HWP half-wave plate; DM: dichroic mirror; GaSe gallium selenide crystal ; LWP: low wavelength pass filter; L: lens.

common noises between pump and signal arms are suppressed. In this way, a narrow linewidth harmonic frequency comb is generated.

The laser source is a commercially available Erbium doped fiber mode-lock laser emitting around 1.55 μm. The repetition rate, f_{rep}, is around 250 MHz and it can be locked to a radio frequency synthesizer referenced to a GPS-disciplined Rb frequency clock.

This laser source is equipped with two independent amplification stages. The main output provides 0.5 W average output power and 50 fs pulse train at 1.55 μm (pump). The second output is coupled to a non-linear Raman fiber and it produces 100 fs tunable self-frequency shifted (SFS) soliton covering between 1.76–1.93 μm with an optical power varying from 100 to 250 mW depending on wavelength (signal). Fig. 3.4 illustrates the difference frequency generation setup.

In order to reach the mid-infrared region, the main 1.55 μm output and the Raman shifted soliton are combined in a non-linear crystal, GaSe, which combines high non-linearity, good transparency at mid-infrared wavelengths and high damaging threshold.

By adjusting Raman soliton wavelength and phase matching angle, it is possible to tune the DFG central wavelength of emission. Fig. 3.5(b) shows the generated mid-infrared frequency combs, with their average output power and their bandwidth, for different Raman solition wavelengths. The output radiation can be centred between 8 μm and 14 μm, with and increasing bandwidth from 0.8 to 3 μm. This enlarged bandwidth towards longer wavelengths is the result of the improved group velocity matching between pump and signal pulses in the crystal.

The maximum output power peaks at 7.8 μm with 4 mW remains over 1 mW up to 10.2 μm and decreases down to 110 μW at the maximum DFG wavelength of 13.6 μm. This output power drop is the result of different factors [77]. At first, the SFS soliton reduces its power at shorter wavelengths. Then, GaSe starts to absorb at wavelengths longer than 12 μm. Finally, the diffraction length of the idler pulse

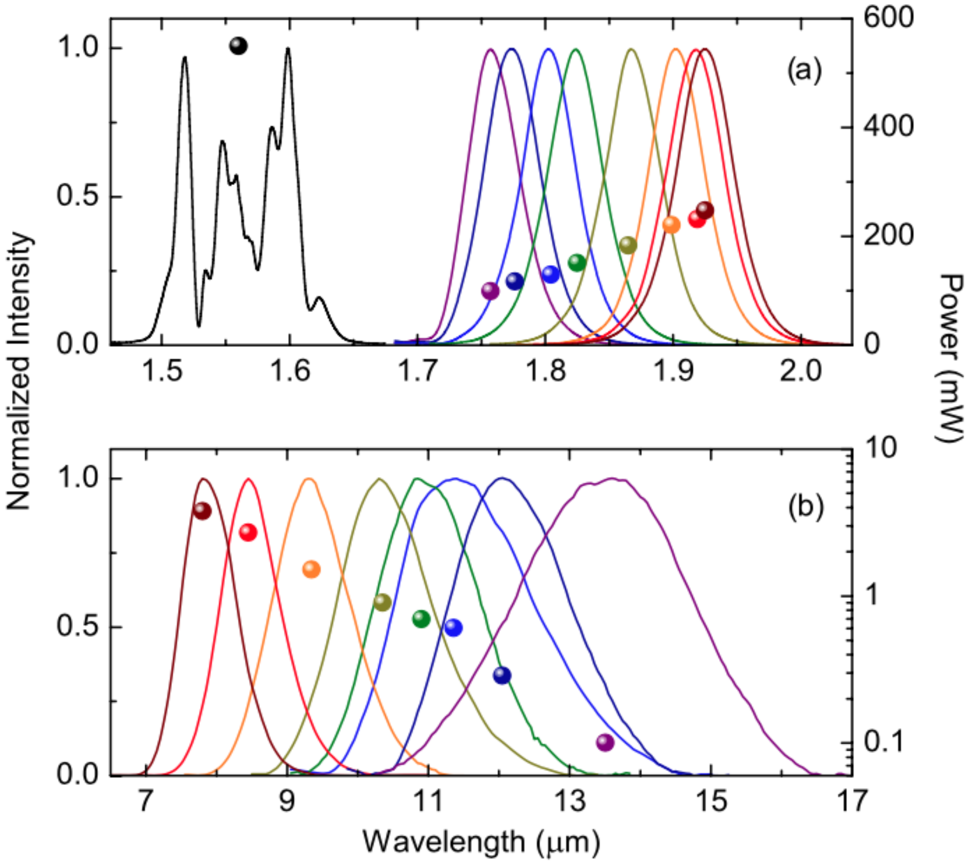

Figure 3.5: Top: Pump (black curve) and signal (coloured curves) normalised spectra recorded by a grating monochromator. Bottom: Generated mid-IR radiation. The dots represent the average power of each spetrum (left axis).

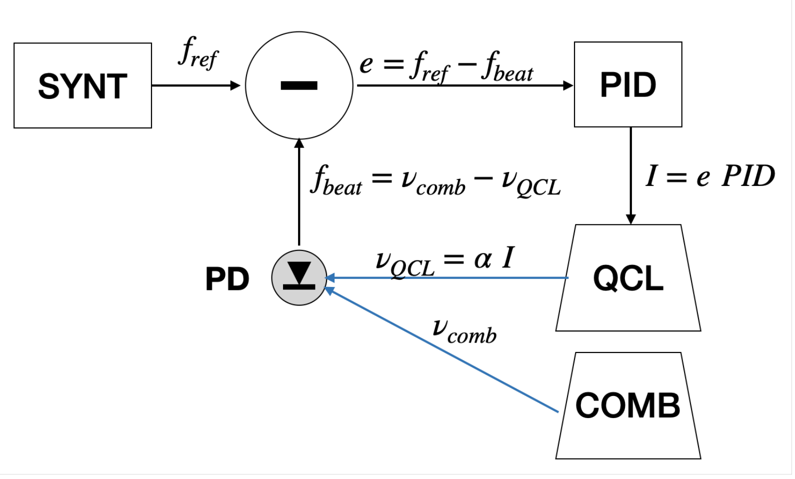

Figure 3.6: Block scheme of the QCL-comb locking. SYNT: synthesiser; f_{ref} reference frequency; e: error signal; PID: proportional-integrative-derivative controller; I: current; QCL: quantum cascade laser; ν_{QCL} frequency of emission of QCL; PD: photodetector; f_{beat}: beatnote frequency between QCL and COMB.

becomes comparable with the spot size dimension inside the crystal.

DFG comb modes are measured with a linewidth of 20 kHz by heterodyne detection with a 4 kHz linewidth QCL [78].

3.2.4 Quantum cascade laser - optical frequency comb lock

Frequency comb modes present a higher stability compared to the QCL. For this reason, they are used as a transfer oscillator to phase lock the QCL in order to shrink its linewidth and, at the same time, to obtain an absolute reference for the laser frequency.

Fig. 3.6 shows the building block of the implemented phase-locking-loop. A beat note between QCL and OFC is created by superimposing them in a 200-MHz bandwidth MCT detector, PD_{beat}, (5.7·104 V/W responsivity and 50 nV/pHz noise floor at a temperature of 77 K). Before the detector, combined radiations pass through a monochromator, in order to filter the frequency comb far from the QCL wavelength. The measured signal is band-passed at 70 MHz (10 MHz bandwidth) and amplified by 50 dB. In order to achieve a tight phase locking ,the beatnote is shifted in frequency with a local oscillator set at 890 MHz, it is divided by 16 obtaining a final beatnote centred at 60 MHz. Then, the divided beatnote is compared with a local oscillator using a phase-detector. In this way, it has been possible to divide the phase noise of the beatnote by 16 in order to fall in the 2π range of the phase detector. The output signal from the phase detector is sent to a Proportional-Integrative-Derivative(PID) digital controller whose output is closing a loop to the QCL current driver. The comparison between unlocked beatnote and the phase locked condition is shown in Fig. 3.7(a) with 1 kHz resolution bandwidth and in Fig. 3.7(b) with 1Hz resolution.

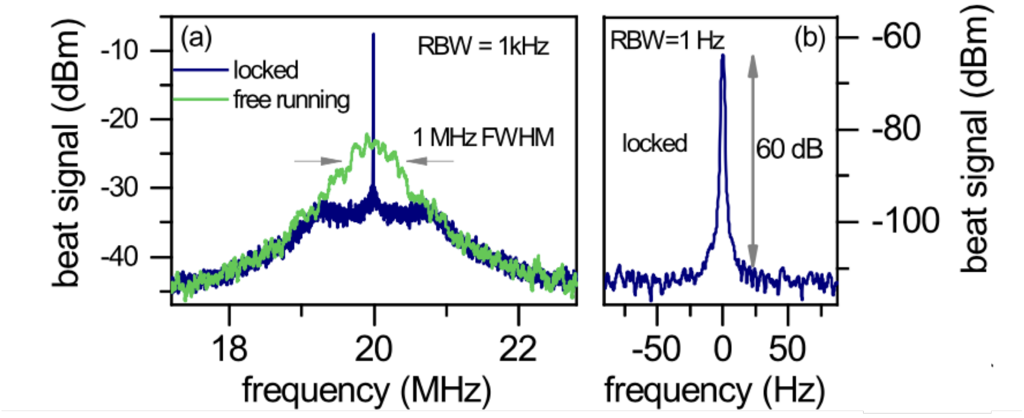

Figure 3.7: Beatnote signal between the QCL and the DFG-OFC, when the QCL is is free running (green curve) and in phase-lock (blue curve) at 1kHz resolution. (b) Phase-locked beatnote at 1 Hz resolution.

According to Eq. 3.3 and by using a Doppler broadened CHF_3 line as frequency discriminator, the QCL frequency noise has been measured [79]. In the case of tight locking (Fig. 3.3), the retrieved frequency indicates a 160 kHz integrated linewidth.

After locking, the QCL frequency is tuned by acting on the frequency comb repetition rate, so that a δf_{rep} is transferred as $\delta f_{QCL} = n\delta f_{\text{rep}}$ where n is the comb mode order (in this case $n \approx 140000$).

3.2.5 Experimental results

By changing the QCL current it is possible to produce an un-calibrated frequency scan. Fig. 3.8 shows the transmitted spectrum through the CHF_3 absorption cell at 10 Pa. This scan is approximately 60 GHz wide, and it shows the very complex and dense spectrum of the CHF_3 around 8.6 μm. The power level is not constant across this frequency range. This will be taken in consideration during absorption line fitting by adding a linear baseline, sufficient to correct this very slow variation around the single line profile. Fig. 3.9 presents a shorter un-calibrated scan, around 1 GHz wide, performed thanks to a frequency ramp provided to QCL external current input. Here, it is possible to appreciate the presence of Lamb-dips inside Doppler broadened profiles, a much narrow feature that indicates the saturation of these absorptions. Besides this, it is also clear a not constant baseline that creates a distortion of all the profiles.

Thanks to a rough registration of the spectrum as a function of the current provided to the QCL, it is possible to set the current value that prepares the system close to an absorption line. From this starting point, and after locking the QCL to the optical frequency comb, it is possible to perform a calibrated scan and register in detail the CHF_3 transmission, with Doppler broadened and Lamb-dip profiles.

Fig. 3.10 shows the transmission of the line ${}^{r}R_{40}(64)$, with a pressure of 4 Pa (blue dots). This transmission profile, T, is fitted by a saturation profile model

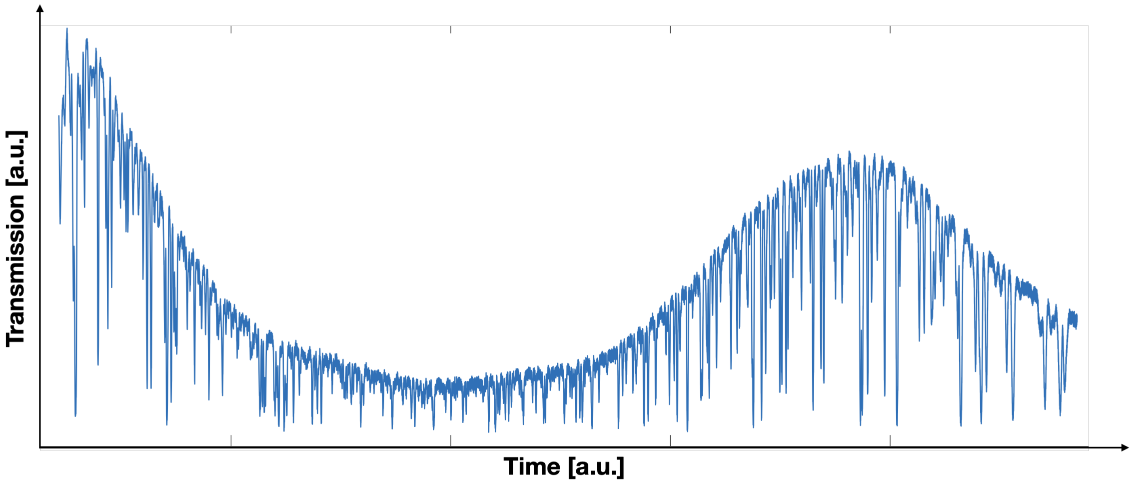

Figure 3.8: Transmission of QCL through CHF_3 absorption cell as a function of time. The un-calibrated scan spans about 60 GHz.

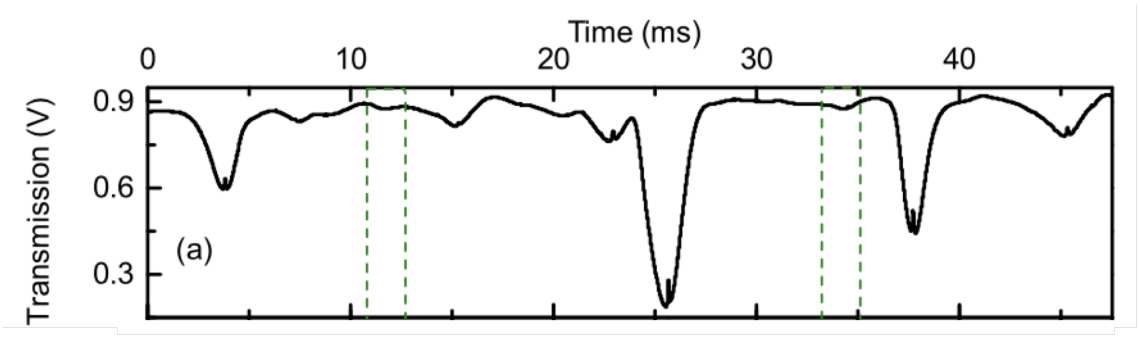

Figure 3.9: Transmission of QCL through CHF_3 absorption cell as a function of time. The un-calibrated scan spans about 1 GHz.

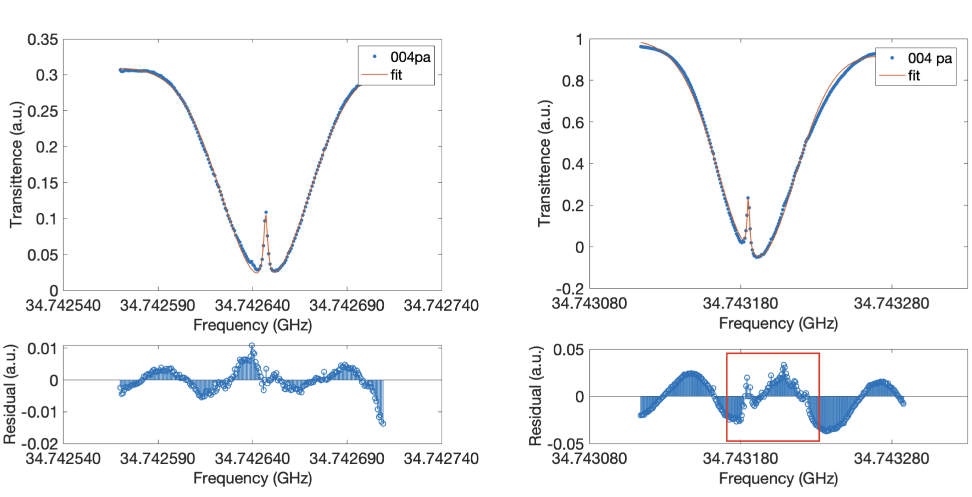

Figure 3.10: QCL transmission through CHF_3 absorption cell as a function of absolute frequency (blue dots) with its fit (red curve) and fitting residuals on the bottom. Right: absorption line ${}^rR_{40}(64)$. Left: absorption line ${}^rR_{36}(38)$.

according to

$$T = (a + b\nu)e^{-\alpha(\nu)}. \tag{3.4}$$

The absorption profile, $\alpha(\nu)$ can be expressed as

$$\alpha(\nu) = N_1\alpha_0(\nu)(1 - N_2\alpha_s(\nu)), \tag{3.5}$$

being N_1 and N_2 normalisation factors, α_0 the Doppler broadened profile, α_s the saturation profile and a, b parameters to take into account a linear baseline. Both Doppler broadened and saturation profiles, are modelled with a Voigt function, keeping a constant Gaussian contribution. The linear profile is dominated by Doppler broadening with a full width at half maximum Γ_G =50 MHz. The sub-Doppler profile takes into account transit time broadening , Γ_{TT} =210 kHz, and the QCL linewidth, Γ_{QCL} =80 kHz, with an overall contribution of Γ_G =225 kHz.

Fitting residuals show a modulation along all the line. This can be attributed to an ethalon effect inside the system, due to a back propagating beam reaching the QCL or the detector. In addition, the presence of this modulation affects the fitting precision itself. Because convergence of fitting is related to the change of residuals in successive steps, the presence of an uncompensated background reduces sensitivity to fitting parameters related to absorption line.

An example of a different line, ${}^rR_{36}(38)$, is plotted in Fig. 3.10(left). In this case, it is evident a shift between Lamb's dip and Doppler-broadened line centres. Looking carefully at its residuals plot, it is possible to notice three different small picks in the right side of the main Lamb's dip (red box). These are additional but weaker saturated absorption profiles, which contribute to the same linear absorption.

A more detailed analysis has been conduced on the saturation profile as a function of gas pressure (Fig. 3.11) and power (Fig. 3.12) for the ${}^rR_{36}(38)$ line. For this narrow scan in the proximity of the Lamb's dip, it is possible to notice how the fitting is in good agreement with the data, with residuals without any structure limited by detection noise. In particular, a full width at half maximum (FWHM) and Dip contrast characterisations have been done as a function of pressure Fig. 3.13, Fig. 3.15 and power Fig. 3.14, Fig. 3.16.

Lamb's dip FWHM, Γ_s, varies with pressure, p, as

$$\Gamma_s(p) = (\gamma^* + pB_p) * \left\{ 1 + \left[1 + \frac{\Omega_0^2}{(\Gamma_G + pB_p)^2} \right]^{-1/2} \right\}, \tag{3.6}$$

and with power, P,

$$\Gamma_s(P) = \gamma_0 \left[1 + \left(1 + \frac{P}{P_s} \right)^{1/2} \right], \tag{3.7}$$

being γ^* the pressure independent linewidth, B_p the pressure broadening coefficient, ω_0 the Rabi frequency, Γ_G the Gaussian broadening contribution, γ_0 the Lorentzian linewidth and P_s the saturation power.

Also,the linewidth contrast, I_s, can be expressed as a function of pressure and power as

$$I_s(p) = N \left\{ 1 - \left[1 + \frac{\Omega_0^2}{(\Gamma_G + pB_p)^2} \right]^{-1/2} \right\} \tag{3.8}$$

and

$$I_s(P) = N \left[1 - \left(1 + \frac{P}{P_s} \right)^{1/2} \right]. \tag{3.9}$$

By fitting this equations into data points, it is possible to obtain the Rabi frequency, the pressure broadening coefficient ,the Lorentzian linewidth and the saturation power (Table 3.1) [73].

Parameter	DS
Satuartion power,P_s (mW)	0.3(1)
Lorentzian linewidth, γ_0 (MHz)	0.29(1)
Rabi frequency, Ω_0 (MHz)	0.7(2)
Pressure broadening, B_p (MHz/Pa)	0.016(2)

Table 3.1: Spectroscopic parameter of line ${}^rR_{40}(64)$.

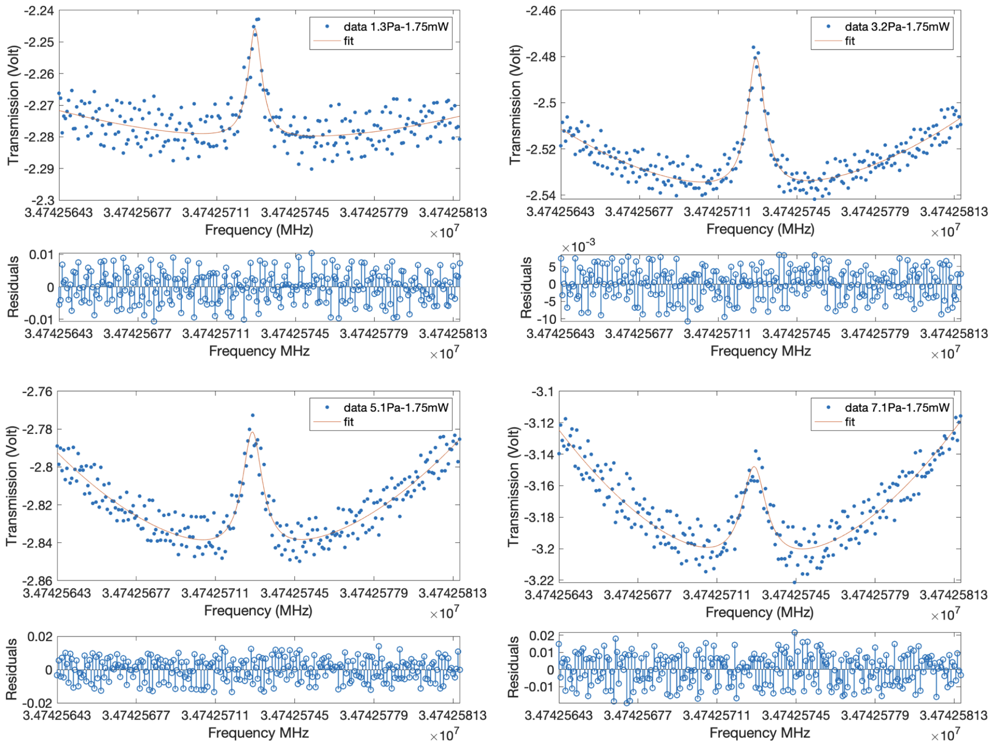

Figure 3.11: CHF_3 line ${}^{r}R_{40}(64)$ in the proximity of its saturated absorption profile (blue dots) accompanied by its best fitting (red line). Bottom panels show the residual of each fitting. Experimental data are reported for a pump power of 1.75 mW and for 4 different pressures 7.1 Pa, 5.1 Pa, 3.2 Pa and 1.3 Pa.

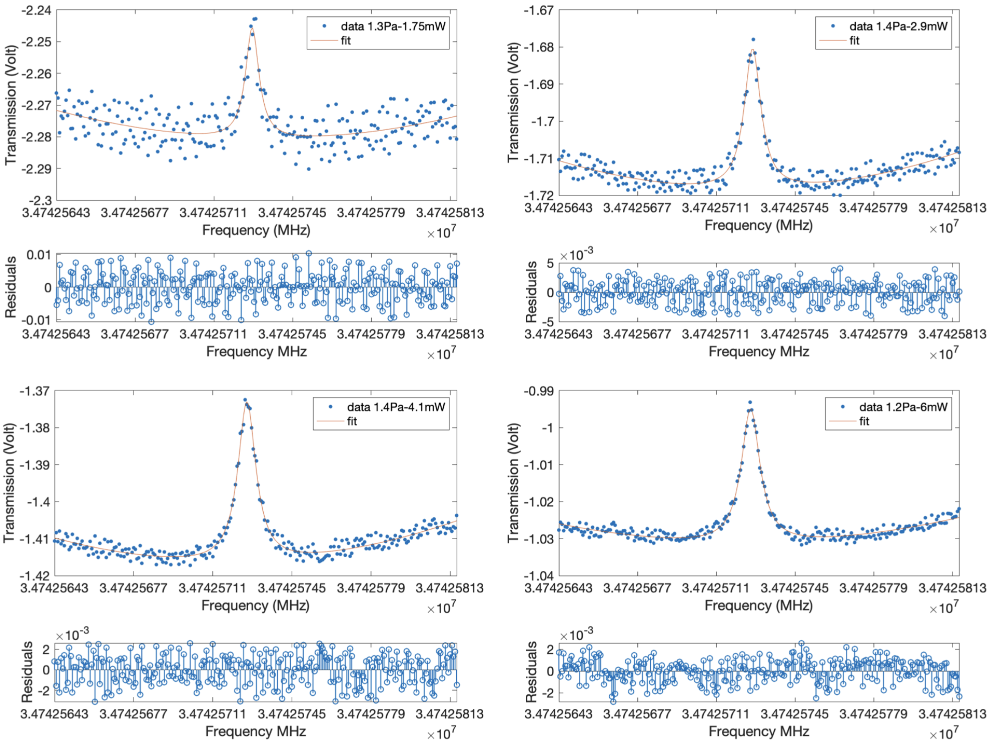

Figure 3.12: CHF_3 line ${}^{r}R_{40}(64)$ in the proximity of its saturated absorption profile (blue dots) accompanied by its best fitting (red line). Bottom panels show the residual of each fitting. Experimental data are reported for a gas pressure of 1.4 Pa and for 4 different powers 1.75 mW, 2.9 mW, 4.1 mW and 6 mW.

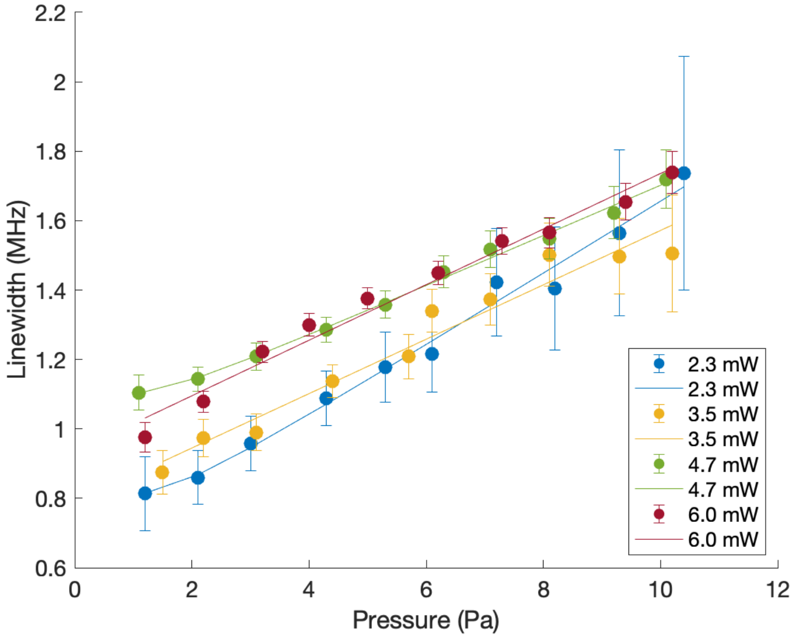

Figure 3.13: Fitted value of the FWHM of CHF_3 saturated absorption profiles (dots) with the corresponding fitting error (error bars) as a function of pressure. Each series of points has been fitted according to Eq. 3.6 (line).

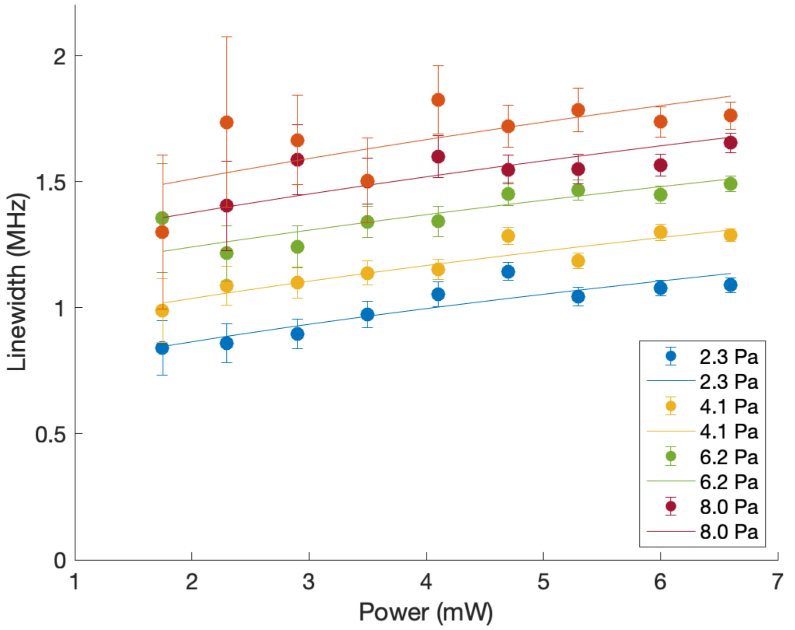

Figure 3.14: Fitted value of the FWHM of CHF_3 saturated absorption profiles (dots) with the corresponding fitting error (error bars) as a function of power. Each series of points has been fitted according to Eq. 3.7 (line).

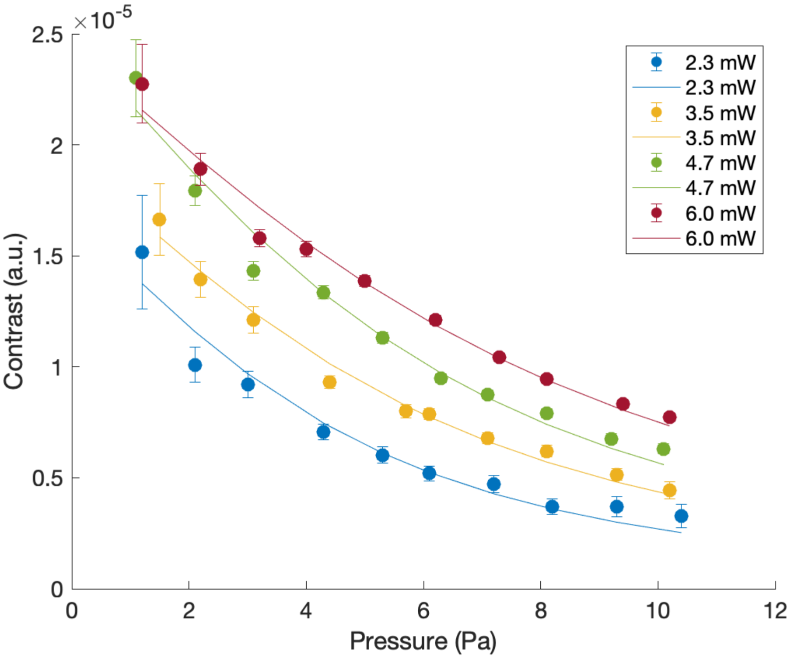

Figure 3.15: Fitted value of the CHF_3 Lamb's dip contrast (dots) with the corresponding fitting error (error bars) as a function of pressure. Each series of points has been fitted according to Eq. 3.8 (line).

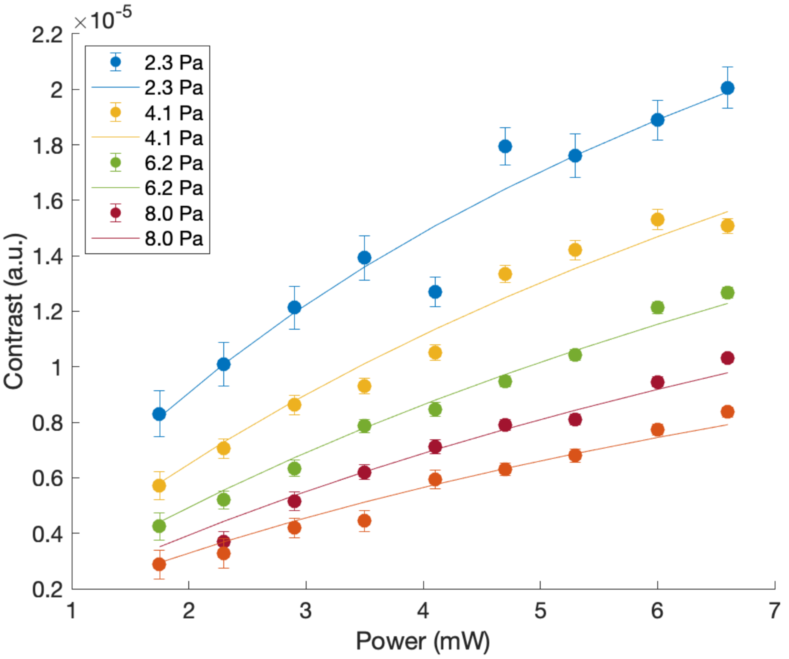

Figure 3.16: Fitted value of the CHF_3 Lamb's dip contrast (dots) with the corresponding fitting error (error bars) as a function of power. Each series of points has been fitted according to Eq. 3.9 (line).

3.3 Wavelength modulation spectroscopy

Direct absorption sensitivity is ultimately limited by technical noise from the photodetector and the laser intensity, which has 1/f dependence with the frequency (flicker noise). In order to improve the sensibility to saturation absorption profiles, a wavelength modulation scheme is implemented. According to section 1.3.3, for a wavelength modulation scheme a modulation index, M, greater than 1 is required. In order to achieve a good sensitivity, the quantity $M\omega_m$ needs to be comparable with full width at half maximum of the saturated profile (being ω_m the modulation frequency). In this case, with a saturated absorption linewidth around 1-2 MHz, a modulation frequency of 100 kHz and a modulation index of 2 are chosen. With these parameters, the demodulated signal can be well approximated to the frequency derivative of the profile. This ensures a much higher signal for saturated profile compared to the Doppler broadened one and, in addition, it removes any slow varying baseline.

3.3.1 Experimental setup

Fig. 3.17 shows the Doppler-free wavelength modulation (WM) spectroscopy setup [6]. The scheme is very similar to the direct spectroscopy setup (section 3.2.1) but with few and important modifications. These changes are implemented in order to eliminate some problems related with the previous experiment. As discussed in the previous chapter, the laser source is a continuous-wave tunable QCL emitting from 1156 to 1160 cm^{-1} (34.68 - 34.80 THz). The QCL is now equipped with a new current controller with a lower noise (2 $\mathrm{nA}/\sqrt{\mathrm{Hz}}$). This allowed to decrease the free running linewidth by a factor of 2, from 1 MHz to 500 kHz.

A more careful design of the optical setup is made in order to decrease parasitic back-reflections. In particular, the QCL beam linearly polarised along the vertical direction is focused inside a Faraday isolator. The power at the output, with a polarisation 45 degrees rotated, is then split by a ZnSe window placed at the Brewster angle. The horizontally polarised reflected beam passes through a quarter wave-plate and it is coupled to a 25-cm long gas cell. Instead, the transmitted beam, after passing through a polariser, is combined with the optical frequency comb. Before entering into the cell, the pump beam is collimated to a diameter of 8 mm by a curved mirror (1 m of radius of curvature).In this way, the corresponding transit time line broadening is 20 kHz (instead of 80 kHz of the previous experiment). After the cell, a mirror reflects back the pump beam. This beam, once attenuated, creates the probe beam with a power ratio 1:8. After probing the gas and passing through the quarter wave-plate, the vertically polarised beam is passing again from the Brewster ZnSe plate. The transmitted radiation is first scattered by a metallic diffuser and, then, it is focused by a plano-convex lens in a 10 MHz bandwidth thermo-electrically-cooled MCT detector.

The combination of Brewster angle power splitting, quarter wave-plate, polariser and diffuser provides a robust rejection to any unwanted back-propagating beam to the QCL and parasitic etalon effects to the detector.

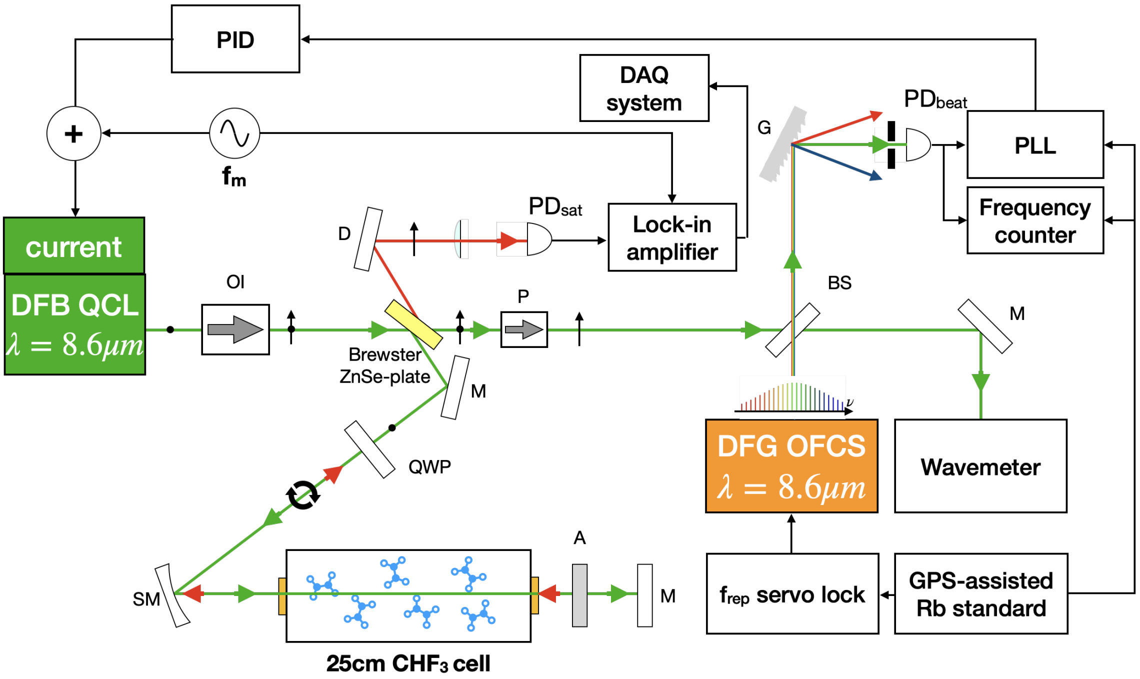

Figure 3.17: Experimental setup for Doppler-free wavelength modulation spectroscopy of CHF_3 .The vertical and the horizontal linear polarization are represented by black dots and arrows, while circular polarization is represented by a clockwise arrow. DFB QCL: distributed feedback quantum cascade laser; DFG OFCS difference frequency comb synthesiser; OI: optical isolator; M: mirror; SM: spherical mirror; D: diffuse reflector; P: polariser; QWP: quarter waveplate; ; A: attenuator; PD: photodetector; PID: proportional-integrative-derivative; BS: beam splitter; DAQ: data acquisition system; G: diffraction grating, f_m: frequency synthesizer.

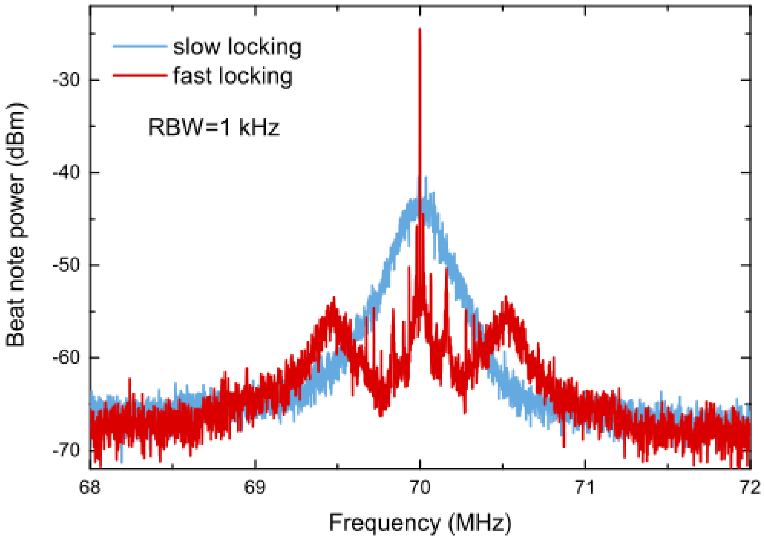

Figure 3.18: QCL- midIR OFC beatnote radio frequency spectrum (1 kHz resolution bandwidth). Blue: free running QCL. Red: QCL phase-locked to the OFC

In addition,the adopted absorption cell is different from the one of section 3.2.1. In particular, a reduced pressure leakage (at a level of 0.5 Pa/h) allows to work at pressure lower than 1 Pa and for longer time. Also the capacitive pressure transducer has been recalibrated.

As in the previous section, the beatnote between QCL and a filtered part of the DFG-OFC is measured by a 200 MHz bandwidth MCT detector, $\mathrm{PD}_{\mathrm{beat}}$. The beatnote frequency is compared, via a fast and low-noise phase detector, to a reference signal at 70 MHz provided by a RF synthesizer synchronized with the Rb standard. Thanks to the new current controller of the QCL, it is no more necessary to up-shift and frequency divide the beatnote frequency before entering the phase detector. The phase detector error signal is then feedback to the QCL current driver through a 1-MHz-bandwidth proportional-derivative-integrative (PID) servo controller. Fig. 3.18 shows the radio frequency spectrum comparison between slow and tight phase-lock control.

In tight phase lock, with a control bandwidth of 500 kHz (inferred from the bumps of the radio frequency spectrum), the beatnote narrows down to the instrument resolution bandwidth (1 kHz) and its signal-to-noise ratio (SNR) increases to 42 dB. This indicates, again, a coherent phase-lock between the QCL and the MIR OFCs, resulting in this case a QCL linewidth of 50 kHz.

To implement wavelength modulation (WM), the QCL current is sinusoidally modulated at a frequency of f_m =100 kHz with a depth of f =200 kHz and the measured WM signal is then demodulated in frequency and phase.

The same frequency-scanning approach of the previous experiment is used in this one. First, the QCL is phase-locked to the closest mid-infrared OFC tooth and then, by changing the frequency comb repetition frequency, it is possible to absolute scan the QCL.

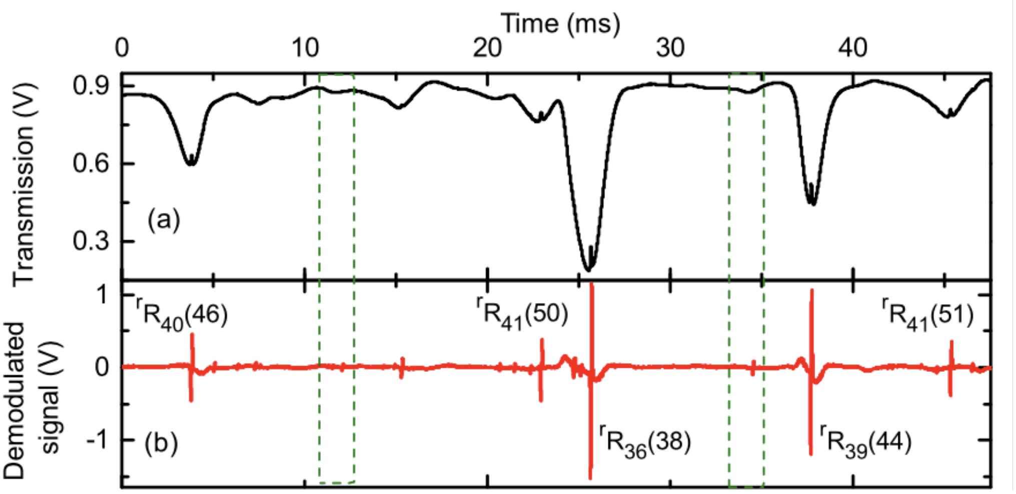

Figure 3.19: Comparison between direct (a) and wavelength modulation (b) spectroscopy of CHF_3 gas at 10 Pa.

3.3.2 Experimental results

As for section 3.2.5, a first un-calibrated scan is recorded. A comparison with direct measurement (corresponding to Fig. 3.9) is presented in Fig. 3.19. It is possible to notice the increased sensibility to saturated absorption profiles. These are visible as steep dispersion profiles, elevating from a slowly varying dispersion profile given by the Doppler broadened absorption. This is possible due to the selected frequency modulation amplitude, which is of the same order of magnitude as the Lamb's dip full width at half maximum but much lower than the Doppler profile. In addition, baseline modulation is suppressed.

Thanks to the higher sensibility to Lamb's dip profile, it is interesting to measure again the line $^rR_{36}(38)$, in comparison with Fig. 3.10. The direct absorption measurement was showing an asymmetry of the line and some structures in the residual, similar to small saturation dips, an indication of multiple absorptions inside the same Doppler broadened profile. With wavelength modulation, Fig. 3.20, it is possible to distinguish easily the presence of five saturation profiles, one strong and four much weaker.

Also, line $^rR_{40}(64)$ can be compared between direct measurements and wavelength modulations, Fig. 3.21. In this case, no additional Lamb's dip profiles are visible.

As in the previous section (3.2.5), absorption profiles are fitted as a function of the linewidth, line-centre and contrast. Wavelength modulation signal, P_{WM}, is modelled according to $P_{\mathrm{WM}} = (S_{1,D} + S_{1,L})$, being $S_{1,D}$ a function taking into account the dispersion signal of the Doppler broadened line and $S_{1,L}$ for the Lamb's dip profile. Because line $^rR_{40}(64)$ is a single isolated line and because the scan is done in the close proximity to the Lamb's dip, the term $S_{1,D}$ is approximated as linear, $a\nu + b$. The term $S_{1,L}$ instead is described by [80]

$$S_{1,L} = A_L \bar{\chi}_{1,L} + B_L(3\bar{\chi}_{0,L} + \bar{\chi}_{2,L}) + C_L \bar{\chi}_{3,L}, \tag{3.10}$$

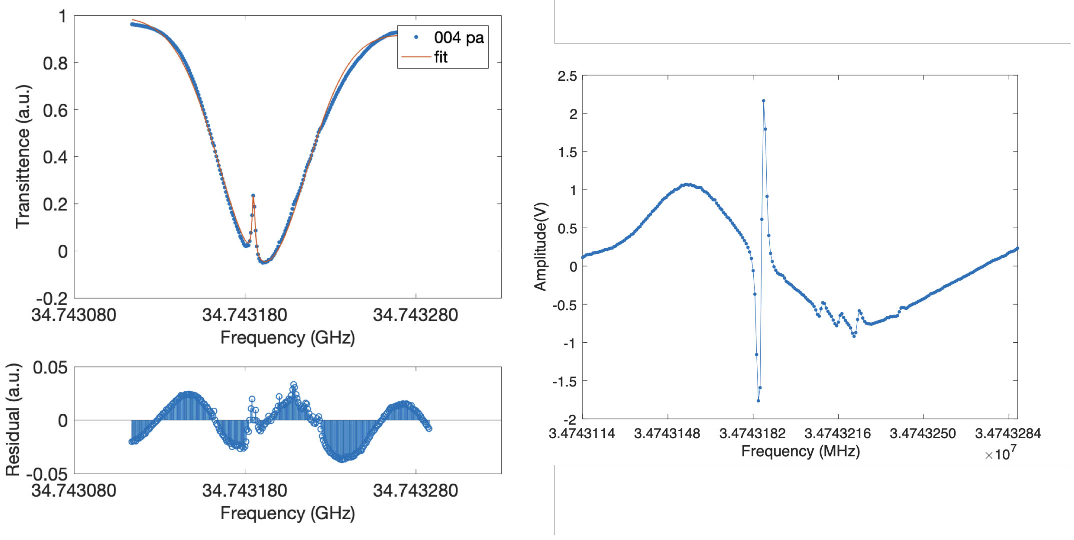

Figure 3.20: QCL transmission through CHF_3 absorption cell as a function of absolute frequency by direct spectroscopy (left) in comparison with WM dispersion signal (right) for absorption line $^{r}R_{36}(38)$. Left figure presents the fitted profile (red) and its residual plot (bottom panel).

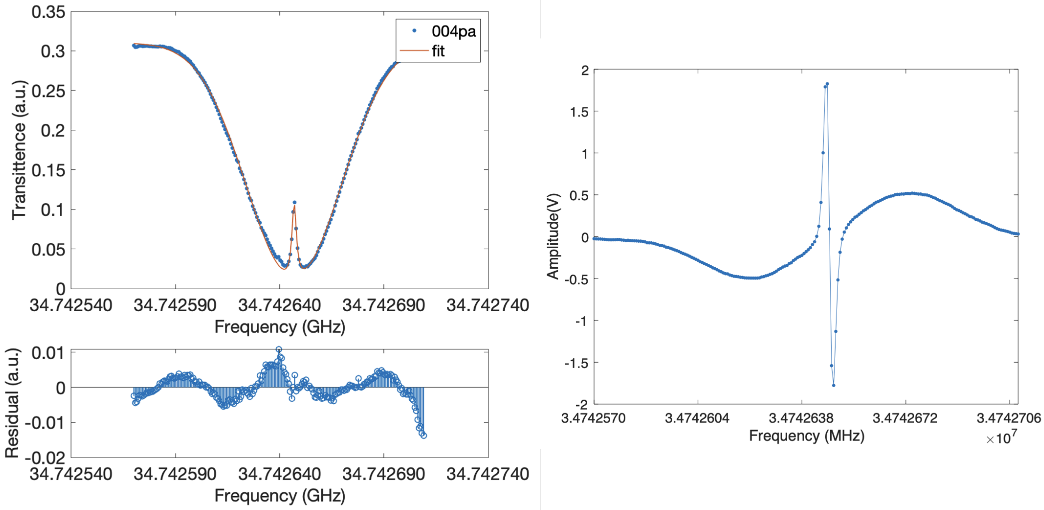

Figure 3.21: QCL transmission through CHF_3 absorption cell as a function of absolute frequency by direct spectroscopy (left) in comparison with WM dispersion signal (right) for absorption line $^{r}R_{40}(64)$. Left figure presents the fitted profile (red) and its residual plot (bottom panel).

where A_L, B_L, C_L are free coefficients. $\chi_{n,L}$ are even components of the n-th Fourier coefficient of wavelength modulated peak-normalised absorption lineshape function $\bar{\chi_L}(\bar{\omega_d}, \bar{\omega_a}, t)$:

$$\bar{\chi}_{n,L}(\bar{\omega_d}, \bar{\omega_a}) = \frac{2-\delta_{n0}}{1/\Omega_m} \int_0^{1/\Omega_m} \bar{\chi_L}(\bar{\omega_d}, \bar{\omega_a}, t) \cos(2\pi n \omega_m t) dt, \tag{3.11}$$

where δ_{n0} is the Kronecker delta, $\bar{\omega_d} = (\omega - \omega_0)/\Delta\omega_d$ is the normalised detuning, $\bar{\omega_a} = a_m/\Delta\omega_d$ is the normalised modulation amplitude and $\Delta\omega_d$ is the molecular linewidth [81]. For this experiment, a Voigt function for the Lamb's dip profile has been chosen. This function is chosen to take into account high harmonic distortions coming from the locking amplifier and from contributions of the residual amplitude modulation, both giving rise to $n = 0, 2, 3$ Fourier coefficient contributions.

Fig. 3.22 and Fig. 3.23 show fittings for measurements carried out at different pressures and powers. Residuals show, in some cases, a structure in correspondence of the line centre, indicating a not perfect convergence of the fitting or the presence of even higher order Fourier contributions. However, since these structures are very close to the noise level, they do not contribute significantly to line-centre or linewidth determination .

Lamb-dip FWHM as a function of pressure and power are shown in Fig. 3.24 and Fig. 3.25. Also in this case, FWHM is fitted as a function of pressure and power,in order to obtain the Rabi frequency Ω_0, the pressure broadening coefficient B_p, the Lorentzian linewidth γ_0 and the saturation power P_s according to Eq. 3.6 and Eq. 3.7. Table 3.2 summarizes these coefficients in comparison with direct spectroscopy [73].

Parameters	DS	WM
Saturation power,P_s (mW)	0.3(1)	0.3(1)
Lorentzian linewidth, γ_0, (MHz)	0.29(1)	0.20(1)
Rabi frequency, Ω_0, (MHz)	0.7(2)	0.8(2)
Pressure broadening, B_p, (MHz/Pa)	0.016(2)	0.013(2)

Table 3.2: Spectroscopic parameters of line ${}^rR_{40}(64)$.

Enhanced sensitivity and baseline fluctuations cancellation allowed also line centre determination for saturated absorption lines by wavelength modulation.

In this way, more than ninety absorption lines have been measured and, for many of them, it was possible to perform an assignment. Comparing with the best literature result about CHF_3 [72], a factor of more than 1000 has been gained in precision with a best fraction precision at the level of 3×10^{-11}. Table 3.3 [6] and Table 3.4 [73] report the measured lines.

	Frequency	**Wave number**	**Assignment**		**Obs. - Calc.**
	(MHz)	**(cm^{-1})**	**ν_5 band**	**ν_2 band**	**(10^{-4} cm^{-1})**
1	34 742 647.0(1)	1158.889 961(3)	$^{r}R_{40}(64)$		7.5
2	34 742 745(1)	1158.893 23(3)	–	–	
3	34 742 786.4(5)	1158.894 61(2)	–	–	
4	34 742 833(1)	1158.896 17(3)	$^{r}R_{39}(66)$		4.1
5	34 742 847(1)	1158.896 63(3)	–	–	
6	34 742 926(1)	1158.899 27(3)	$^{r}R_{41}(61)$		5.5
7	34 742 998(1)	1158.901 67(3)		$^{q}R_{36}(79)$	3.1
8	34 743 185.1(1)	1158.907 910(3)	$^{r}R_{36}(38)$		0.3
			$^{r}R_{37}(77)$		4.9
			$^{r}R_{41}(75)$		5.5
9	34 743 208.8(5)	1158.908 70(2)	–	–	
10	34 743 216.1(5)	1158.908 94(2)	–	–	
11	34 743 223.2(3)	1158.909 18(1)	–	–	
12	34 743 240.2(5)	1158.909 75(2)	–	–	
13	34 743 311.3(1)	1158.912 120(3)	–	–	
14	34 743 331.6(3)	1158.912 80(1)	–	–	
15	34 743 366.0(5)	1158.913 94(2)		$^{q}R_{36}(80)$	6.4
16	34 743 415.0(5)	1158.915 58(2)	–	–	
17	34 743 423(1)	1158.915 85(3)	–	–	
18	34 743 632.5(3)	1158.922 83(1)	$^{r}R_{39}(73)$		7.2
19	34 743 652(1)	1158.923 48(3)		$^{q}R_{36}(81)$	6.3
20	34 743 676(1)	1158.924 29(3)	$^{r}R_{37}(78)$		1.3
21	34 743 690.2(5)	1158.924 76(2)	$^{r}R_{40}(74)$		-2.0
22	34 743 771.4(5)	1158.927 48(2)	–	–	
23	34 743 795(1)	1158.928 25(3)	–	–	
24	34 743 813(1)	1158.928 86(3)		$^{q}R_{36}(87)$	0.4
25	34 743 907(1)	1158.931 99(3)	–		
26	34 743 978.9(5)	1158.934 39(2)	$^{r}R_{43}(78)$		7.8
			$^{r}R_{39}(76)$		4.0
				$^{q}R_{36}(86)$	3.2
27	34 743 991.0(5)	1158.934 79(2)		$^{q}R_{36}(83)$	0.7
28	34 744 023.8(5)	1158.935 89(2)	–	–	
29	34 744 067.9(5)	1158.937 36(2)		$^{q}R_{36}(84)$	3.7
				$^{q}R_{36}(85)$	5.7
30	34 744 107(1)	1158.938 66(3)	$^{r}R_{37}(79)$		3.5
31	34 744 110(1)	1158.938 76(3)	–	–	
32	34 744 130.6(1)	1158.939 449(3)	$^{r}R_{4}(5)$		-1.4
33	34 744 148(1)	1158.940 03(3)	$^{r}R_{38}(77)$		-7.3
34	34 744 310(1)	1158.945 43(3)	$^{r}R_{39}(67)$		7.1
			$^{r}R_{40}(46)$		9.0
35	34 744 326.0(1)	1158.945 967(3)	–	–	
36	34 744 333(1)	1158.946 20(3)	–	–	

Table 3.3: Measured line centre frequencies (and wave numbers) for sub-Doppler Spectroscopy of CF_3H at 6 Pa. The uncertainties, indicated in parenthesis, represent the quadrature sum of type A and B errors (at one standard deviation). For some of the transition it has been possible to perform a line assignment(4-th column) and to calculate the difference between observed (OBs.) and calculated (Calc.) values (5-th column).

	Line	**FTIR [72] (MHz)**	**This work [6] (MHz)**	**FTIR−This work (MHz)**
1	$^rR_1(1)$	34 708 835.2	34 708 837.8290±0.0017	-2.656
2	$^rR_2(2)$	34 712 895.6	34 712 899.8615±0.0013	-4.299
3	$^rR_3(3)$	34 716 957.2	34 716 956.0149±0.0011	1.136
4	$^rR_4(4)$	34 721 013.9	34 721 012.4370±0.0007	1.505
5	$^rR_5(5)$	34 72 5080.3	34 725 074.8574±0.0006	5.470
6	$^rR_6(6)$	34 729 147.3	34 729 149.9446±0.0005	-2.633
7	$^rR_7(7)$	34 733 247.0	34 733 244.9299±0.0006	2.044
8	$^rR_2(3)$	34 735 062.8	34 735 060.0431±0.0026	2.773
9	$^pQ_3(4)$	34 736 831.9	34 736 828.9994±0.0017	2.892
			34 736 830.7659±0.0017	1.126
			34 736 832.5359±0.0029	-0.644
10	$^rR_8(8)$	34 737 367.6	34 737 368.5083±0.0006	-0.887
11	$^rQ_3(5)$	34 738 549.4	34 738 540.8459±0.0009	8.557
			34 738 550.2162±0.0014	-0.813
			34 738 559.5832±0.0008	-10.180
12	$^rR_3(4)$	34 739 579.8	34 739 577.9827±0.0012	1.807
13	$^rR_9(9)$	34 741 532.6	34 741 530.7673±0.0008	1.870
–	$^rR_{40}(64)$	not measured	34 742 646.8843±0.0020	–
14	$^qR_{36}(38)$	34 743 190.8	34 743 208.7755±0.0027	-17.986
			34 743 215.9818±0.0030	-25.192
			34 743 223.1982±0.0026	-32.409
			34 743 185.0479±0.0011	5.742
15	$^rR_4(5)$	34 744 132.1	34 744 130.5099±0.0012	1.628
16	$^rR_{10}(10)$	34 745 730.9	34 745 717.9067±0.0009	13.024
			34 745 743.5605±0.0014	-12.629
17	$^pQ_3(8)$	34 746 250.8	34 746 243.7368±0.0022	7.034
			34 746 249.3207±0.0025	1.450
			34 746 254.8809±0.0014	-4.110
18	$^rR_5(6)$	34 748 733.4	34 748 729.0657±0.0014	4.287
			34 748 736.9559±0.0011	-3.603
19	$^rR_{11}(11)$	34 750 022.5	34 750 020.9530±0.0010	1.507
20	$^rR_0(2)$	34 750 517.4	34 750 520.0922±0.0013	-2.675
21	$^rR_1(3)$	34 752 456.8	34 752 459.4223±0.0017	-2.648
22	$^rR_6(7)$	34 753 385.5	34 753 384.7613±0.0009	0.771
23	$^rR_{12}(12)$	34 754 379.0	34 754 379.6108±0.0010	-0.567
24	$^rR_2(4)$	34 757 436.9	34 757 438.6647±0.0015	-1.738
25	$^rR_7(8)$	34 758 112.7	34 758 109.6132±0.0009	3.046
26	$^rR_{13}(13)$	34 758 839.7	34 758 839.4008±0.0010	0.255
27	$^pQ_4(18)$	34 761 251.2	34 761 250.6489±0.0021	0.538
28	$^rR_3(5)$	34 762 420.1	34 762 419.3883±0.0030	0.689
29	$^rR_8(9)$	34 762 918.0	34 762 917.1283±0.0016	0.904
30	$^rR_{14}(14)$	34 763 425.6	34 763 424.3134±0.0010	1.268
31	$^pQ_3(12)$	34 763 521.5	34 763 519.1044±0.008	2.410
			34 763 520.3190±0.003	1.196
			34 763 523.6288±0.007	-2.114
			34 763 526.9831±0.0025	-5.468
32	$^pQ_4(9)$	34 764 429.3	34 764 426.8173±0.0018	2.469
33	$^rR_4(6)$	34 767 444.6	34 767 424.0222±0.0014	20.577
			34 767 455.5706±0.0013	-10.972
34	$^rR_9(10)$	34 767 824.7	34 767 822.4955±0.0018	2.240
35	$^rR_{15}(15)$	34 768 164.7	34 768 162.9665±0.0017	1.734
36	$^PQ_3(13)$	34 769 164.8	34 769 162.1179±0.0018	2.690
			34 769 164.9234±0.007	-0.115
			34 769 167.7264±0.0019	-2.918
37	$^rR_5(7)$	34 772 579.7	34 772 567.4563±0.0006	12.288
			34 772 590.3380±0.0010	-10.594
38	$^rR_{10}(11)$	34 772 843.9	34 772 843.0484±0.0005	0.813
39	$^rR_{16}(16)$	34 773 090.9	34 773 089.8611±0.0004	1.029

Table 3.4: Measured line centre frequencies for sub-Doppler spectroscopy of CF_3H at 1 Pa (4-th column) in comparison with 30 MHz resolution FTIR measurement from ref. [72] at 5 Pa (3-rd column). The uncertainties of this work represent the type A statistical contribution (at one standard deviation). The last column presents the frequency difference between this work and ref. [72].

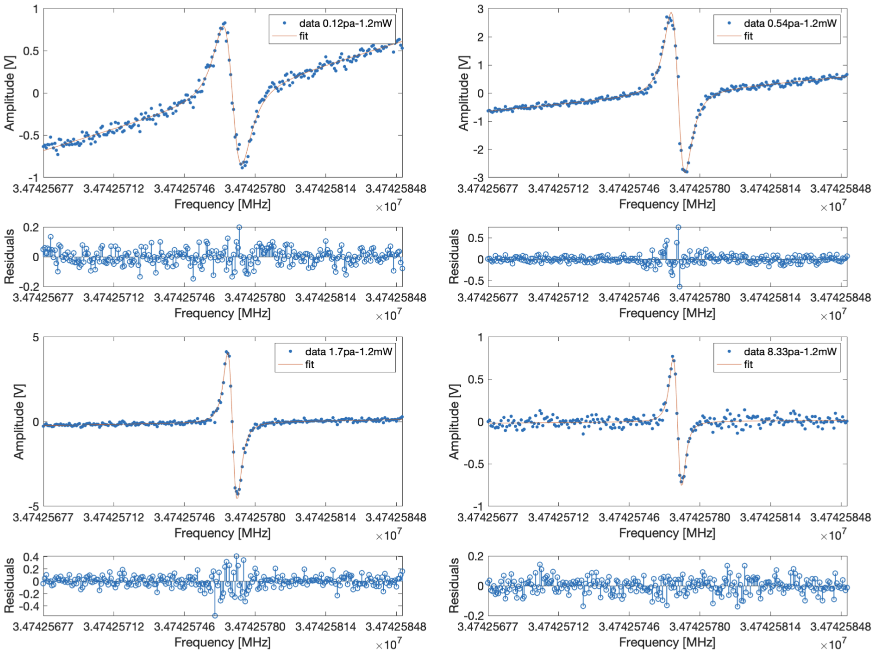

Figure 3.22: CHF$_3$ line $^rR_{40}(64)$ in the proximity of its saturated absorption profile (blue dots) accompanied by its best fitting (red line). Bottom panels show the residual of each fitting. Experimental data are reported for a pump power of 1.2 mW and for four different pressures 0.12 Pa, 0.54 Pa, 1,7 Pa, 8.3 Pa.

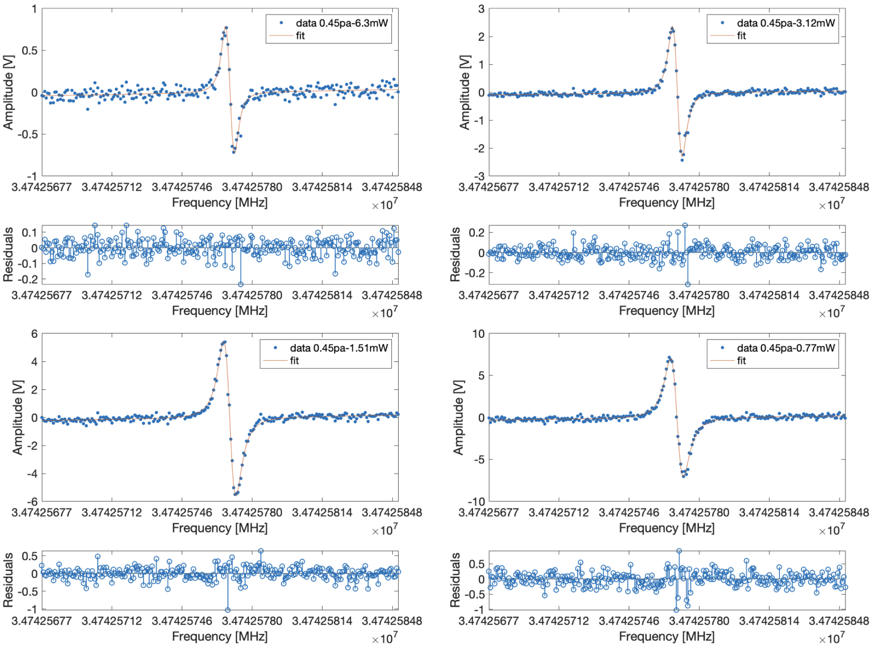

Figure 3.23: CHF$_3$ line ${}^rR_{40}(64)$ in the proximity of its saturated absorption profile (blue dots) accompanied by its best fitting (red line). Bottom panels show the residual of each fitting. Experimental data are reported for a gas pressure of 0.45 Pa and for four different powers 6.3 mW, 3.12 mW, 1.5 mW and 0.77 mW.

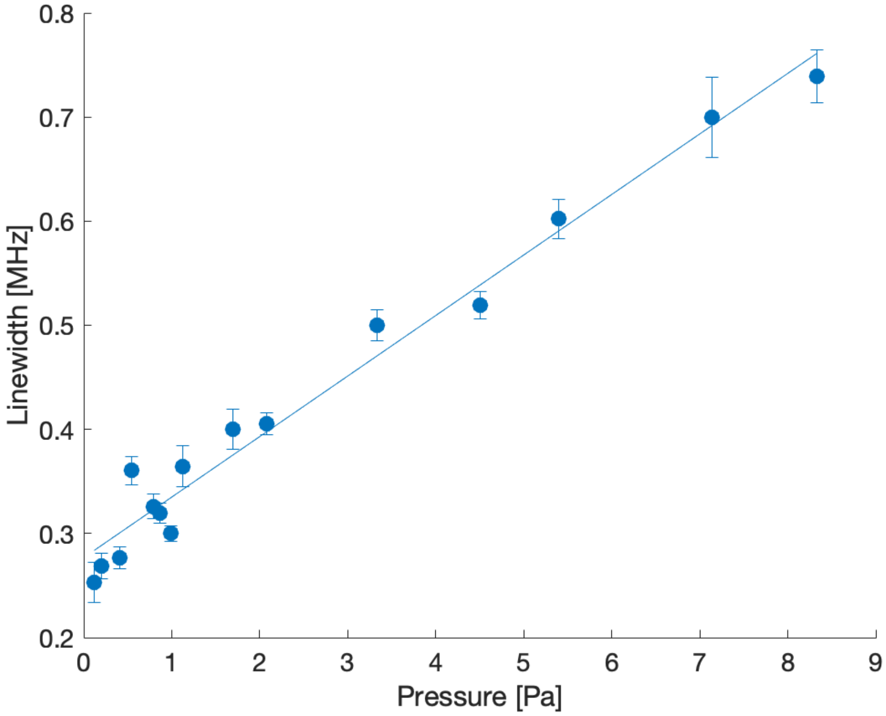

Figure 3.24: Fitted HWHM of the CHF_3 saturated absorption profile (dots) and corresponding fitting error (error bar) as a function of pressure for a pump power of 1.2 mW. The series is the fitted according to Eq. 3.6.

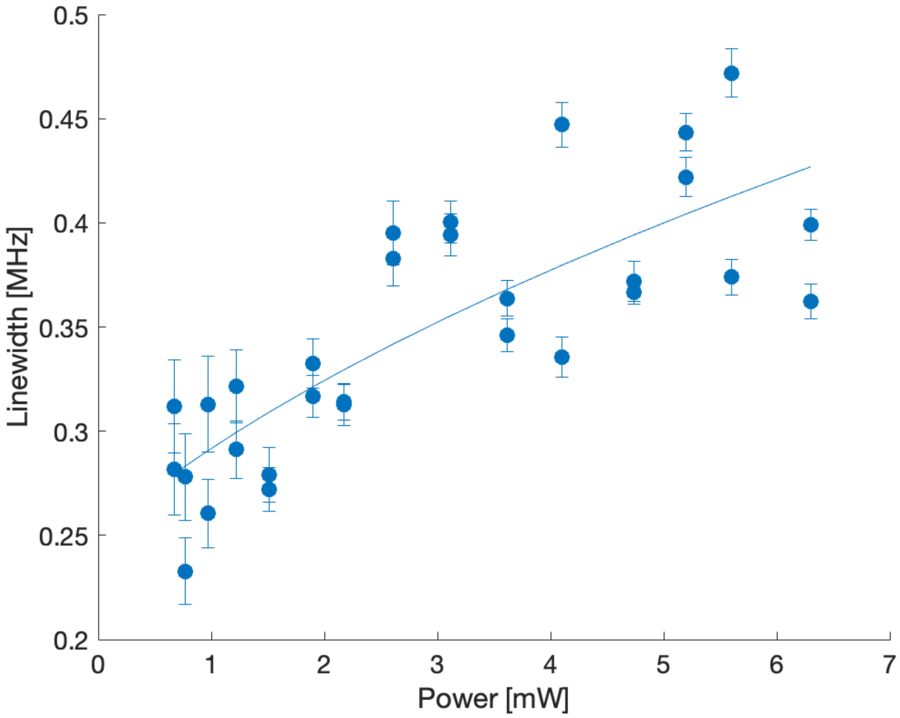

Figure 3.25: CHF_3 saturated absorption half width at half maximum as a function of power for a pressure of 0.45 Pa.

Chapter 4

Absolute frequency stabilization of a QCL to saturated absorption of CHF_3

Quantum cascade lasers (QCLs) are a new and mature technology to access mid-infrared (MIR) spectral region and they offer a compact and reliable alternative to difference frequency generation (DFG) system. They offer a continuous tuning over several hundred gigahertz at 100 mW-level powers simply by adjusting temperature or injection current and they can be design to emit anywhere between 3–25 μm covering all MIR range.

Although intrinsic emission linewidth of QCLs can be expected to be very narrow [82], excess technical noise, such as the pump current noise and internally induced QCL structure noise, broadens the QCL emission linewidth by several orders of magnitude up to few megahertz for 1 ms observation times.

Several methods have demonstrated a significant reduction of the QCL linewidth: all-electronic locking [83][84], phase-locking to a narrow linewidth laser [85][86] or to optical frequency comb based sources [87][88], frequency locking to a sub-Doppler molecular transition [89][90]or locking to a Fabry–Perot cavity [91][92].

After narrowing the emission linewidth, QCL sources have been demonstrated to be extremely suitable for high-sensitivity and high-resolution spectroscopy, or for frequency metrology, due to their good stability and high emission power.

In this chapter, an approach to narrow QCL emission linewidth and to absolutely referenced it to a strong molecular absorption line of CHF_3 is presented, whose centre frequency can absolutely be measured with a sub-kilohertz precision.

4.1 Absolute frequency stabilisation by frequency modulation

A frequency modulation is a modulation technique characterised by a modulation index, M, lower than one [14]. In this case, the spectrum results in a carrier and a single pair of sidebands. After interacting with an absorption feature and if the right

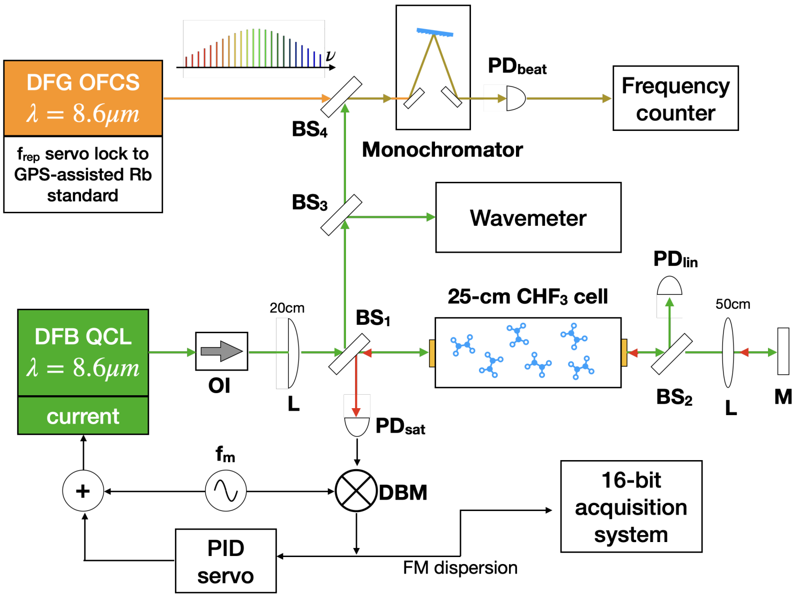

Figure 4.1: Experimental setup for frequency stabilisation against sub-Doppler rovibrational transition of CHF_3 at 8.6 μm by frequency modulation. QCL: quantum cascade laser; DFG OFC: difference frequency generation optical frequency comb; BS: beam splitter; L: spherical lens; M: gold mirror; OI: optical isolator; PD: photodetectors; PID: proportional integrative derivative controller; DBM dual balanced mixer; f_m modulation frequency synthesiser.

phase is chosen in the synchronous demodulation, the signal results proportional to the dispersion of this absorption, a signal that can be used easily as a frequency discriminator for servo control.

In this experiment, frequency modulation is applied to a QCL interacting with sub-Doppler absorption of CHF_3 around 8.6 μm [93]. The demodulated signal is then used to frequency lock the QCL and shrink its emission linewidth.

4.1.1 Experimental setup

The experimental setup for frequency stabilisation is shown in Fig.4.1. Summarising, a QCL emitting from 1155 cm^{-1} to 1160 cm^{-1} (34.68 - 34.80 THz) is coupled to an absorption cell containing CHF_3 in a double pass configuration. In this way, a saturated absorption is generated and it can be used as frequency reference.

By applying a signal at $f_m = 1.56$ MHz with an amplitude of $A = 0.006$ V to the QCL current input, thanks to the current to frequency conversion of this source, a frequency modulation is created with an estimated amplitude depth of $a_m = 1.5$ MHz, corresponding to a modulation index close to 1. The detector output, PD_{sat}, recording the double pass from the absorption cell, is demodulated in-phase and the signal is sent to a digital PID controller. The feedback loop is closed on the QCL current.

As for section 3.2, part of QCL radiation is combined with DFG frequency comb

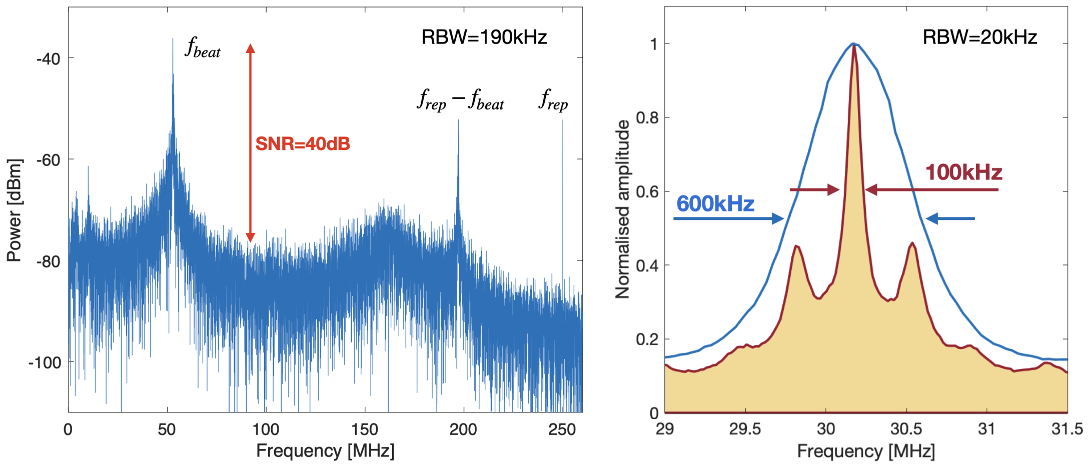

Figure 4.2: Radio frequency spectrum of the beat signal between the QCL and the optical frequency comb: (a) QCL in free-running operation (190-kHz resolution bandwidth); (b) QCL frequency stabilized against the FM saturated absorption of the $^{r}R_{36}(38)$ line (red) in comparison with a sloppy-lock (blue) (20 kHz resolution bandwidth).

in order to generate a beatnote on a MCT detector. In this case, the frequency comb is used to characterise the frequency stability of the QCL locked to the saturated absorption profile, allowing a direct comparison with the GPS-disciplined Rb clock.

4.1.2 Experimental results

Fig. 4.2 shows the radio frequency spectrum of the photocurrent measured by the detector when QCL is operating in free running. Three main peaks are visible: the low frequency beatnote signal, f_{beat}, at 53 MHz corresponds to the beating between QCL and comb closest mode; a second beatnote at 197 MHz relative to the second nearest comb mode; and the repetition frequency of the optical frequency comb at 250MHz.

The main beatnote presents a SNR of more than 40 dB, and it is characterised by a 600 kHz 3 dB linewidth at 50 μs of integration time (Fig. 4.2(b) blue curve). When the QCL laser is tightly locked to the saturated absorption of the line $^{r}R_{38}(36)$, its linewidth of emission shrinks down to 100 kHz (Fig. 4.2(b) red curve). This linewidth is mainly limited by a 350 kHz control-loop bandwidth which is strictly limited by FM demodulation electronics finite bandwidth of 100 kHz.

Frequency stability of the QCL after locking to the sub-Doppler profile of CHF_3 is characterised by measuring the main beatnote frequency (at 30.2 MHz) by a reciprocal electronic counter without any additional phase-locked-loop (transfer oscillator method).

Fig. 4.3(a) shows the corresponding Allan deviation (open circles) versus the integration time, τ. Allan deviation represents an average variance between different samples and, usually, it is employed to characterise the frequency stability of oscil-

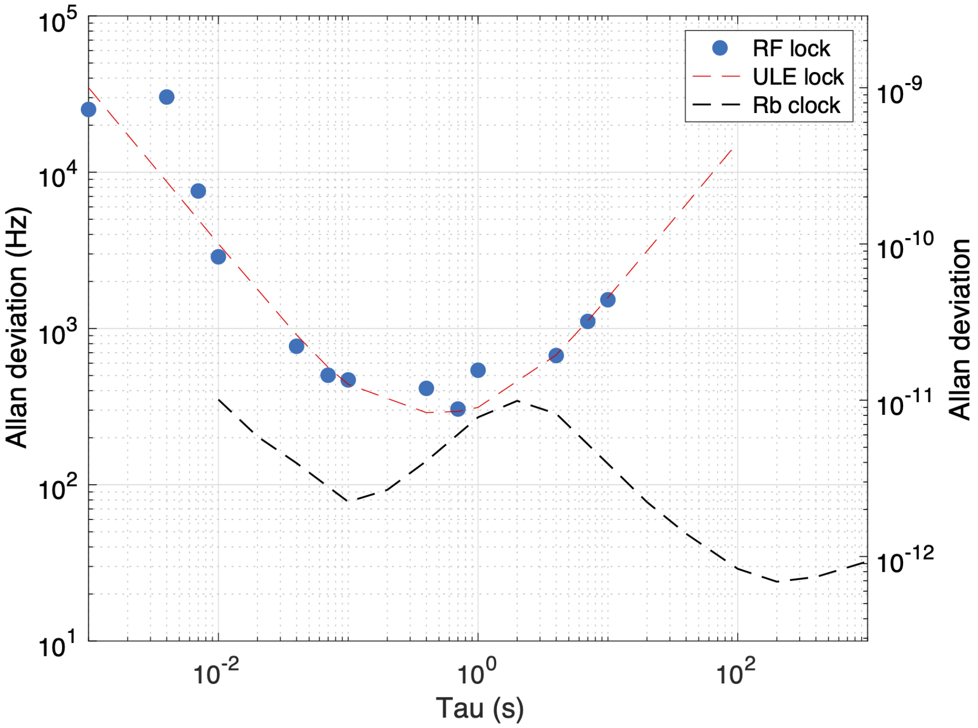

Figure 4.3: Allan deviation of the Lamb-dip-locked QCL frequency versus the integration time (blue dots); the best interpolation curve, $\sigma_y^2(\tau) = 10^{24}\tau^{-2} + 0.6 \cdot 10^{22} + 6 \cdot 10^{24}\tau^2$ (dashed red line); Rb clock stability (black curve).

lators. For M samples with a calculated frequency $y_i(\tau)$, Allan variance is defined as $\sigma_y^2(M, T, \tau) = \frac{1}{2(M-1)} \sum_{i=1}^{M-1} [y(\tau)_{i+1} - y(\tau)_i]^2$. Allan deviation is the square root of this value.

In this case, the QCL is locked against the ^{r}R36(38) line for a CHF$_3$ pressure of 7 Pa (corresponding to the maximum SNR). In comparison, the Allan deviation of the Rb clock measured against a hydrogen maser, used as a reference for the frequency comb, is displayed in the same figure (black curve).

The maximum stability of the QCL is obtained at an integration time of $\tau =$ 1 s corresponding to the minimum Allan deviation of $8.6 \cdot 10^{-12}$. This value seems limited by the employed Rb-clock reference oscillator, allowing the possibility for an even better stability at this integration time.

For shorter integration times, Allan deviation presents a dependence of $\sigma(\tau) = 10^{12} \cdot \tau^{-1}$, which can be described as white phase noise contribution. This is an indication of a tight phase-locking between the QCL and the Lamb-dip reference. Instead, for integration time longer than 1 s, the QCL stability decreases exceeding the Rb-clock limit. From beatnote frequency measurement, this result from a linear drift of 4.5 kHz/min, attributed to the air-pressure-induced shift caused by the relatively high leakage (0.14 Pa/min) from the gas cell.

By removing from the data the measured linear frequency drift, the Allan deviation is limited at the level of $8 \cdot 10^{-12}$ by a flicker frequency noise contribution.

Parameter	Coefficient	Type B uncertanty
CHF_3 preassure	22(1) kHz/Pa	0.75 kHz
gas cell leakege	38(2) kHz/Pa	1.5 kHz
laser power	45 kHz/mW	0.2 kHz
modulation frequency	100 Hz/kHz	negligible
modulation depth	16 kHz/MHz	negligible
electronic offset	0.3 kHz/mV	0.2 kHz
etalon/interference effects		0.5 kHz
Rb-GPS-clock		0.04 kHz
Total type B uncertainty		1.8 kHz ($5{\cdot}10^{11}$)

Table 4.1: Measured and estimated uncertainty budget relative to frequency stabilisation of a QCL to CHF_3 ${}^{r}R_{36}(38)$ absorption line by frequency modulation [93].

4.1.3 Uncertainty budget

A study of the possible effect of systematic error is conducted. In particular, Lamb-dip-locked beatnote frequency dependence as a function of gas pressure and QCL power have been studied. Moreover, gas leakage, electronic offset, etalon effects and reference signals stabilities have been also analysed.

Table 4.1 reports results of this study together with their influence on the systematic (type B) uncertainty of the absolute frequency measurement. From this analysis, it results that the combined contribution of pressure shift coefficient, pressure accuracy measurement and gas cell leakage during the measurement time are the major source of type B uncertainties. The total type B uncertainty is calculated as 1.8 kHz , corresponding to a fractional accuracy of $5{\cdot}10^{-11}$.

Repeatability is also analysed by repeating several measurements with the same nominal parameters over several days. Experimental operating parameters are precisely: $p_{\mathrm{CHF_3}}$= 7.00 ± 0.04 Pa, T_{room}= 22.1 ± 0.5 ℃, P_{pump}= 5 mW, P_{probe}= 1.3 mW, f_{m}= 1.56 MHz, a_{m}= 1.5 MHz. Each measure reported in Fig. 4.4 correspond to an integration time of 1 s averaged for 100 samples (total measurement time per point 100 s). The average of these fifteen independent measurements is 34 743 125 035(2) kHz and they result in a rms deviation of 8.9 kHz ($2.6{\cdot}10^{-10}$). Taking into account the pressure-shift coefficient, the line-centre frequency of the ^{r}R36(38) transition extrapolated at zero pressure is 34 743 124 881(2) kHz (1 158.905 901 53(8) cm^{-1}) [93].

4.2 Absolute frequency stabilisation by modulation transfer

A similar strategy to remove technical noises and to detect absorption signals at higher frequencies is based on modulation transfer [94].

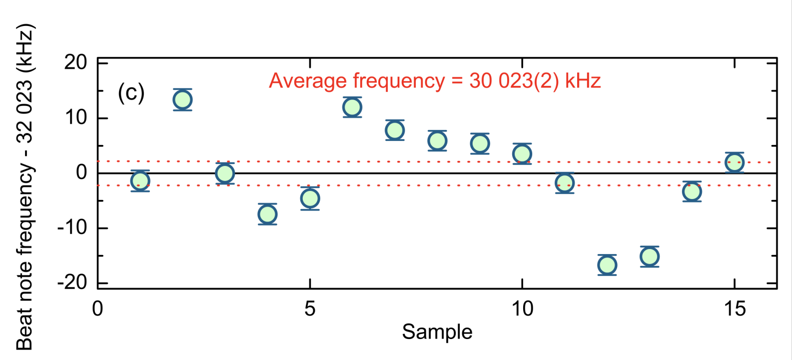

Figure 4.4: Repeatability in the CHF_3 line-centre frequency determination for different measurements. Each point represents the average of 100 samples at 1 s of integration time, with the errorbar corresponding to the standard deviation of this measurements. The dashed red line is the uncertainty of the average value. All the measurements were performed at the same nominal experimental parameters.

When an unmodulated probe beam interacts with a nonlinear medium exited by a modulated pump beam, it acquires sidebands in a process called modulation transfer. This transfer is due to a four-wave mixing process via medium's susceptibility between the probe and two frequency components of the modulated pump.

Differently from wavelength/frequency modulation that are sensible to all the absorption profiles, modulation transfer completely suppresses the linear Doppler broadened absorption and it provides a dispersion-like signal with a zero-crossing at line centre. Due to this, modulation transfer becomes particularly attractive when using non-linear molecular absorption to establish reference with long-term stability and accuracy [95][96].

In this section, modulation transfer is applied to frequency stabilising a QCL to a saturated absorption of CHF_3 [7].

4.2.1 Experimental setup

Fig. 4.5 shows the experimental setup. The laser source is the same QCL of the previous section 3.2.2.

After passing through a 30 dB optical isolator and a half-wave plate, the laser beam is split by a Ge-window at the Brewster's angle. This series of optical elements allow to control the splitting ratio of the Ge-window by changing the half-wave plate. Moreover, it provides a robust rejection of any back-propagating beam. Transmission and reflection of the Ge-window are the pump and the probe beams, respectively, for saturation spectroscopy in a counter-propagating and crossed-linear-polarization configuration.

Before interacting with the sample, the pump beam is focused into a 50 MHz acousto-optic modulator (AOM). The fist order diffraction of the AOM is re-collimated and sent to a 25-cm-long cell filled with few pascal of fluoroform gas, CHF_3, at room temperature. After interacting with the pump beam in the sample, the probe beam

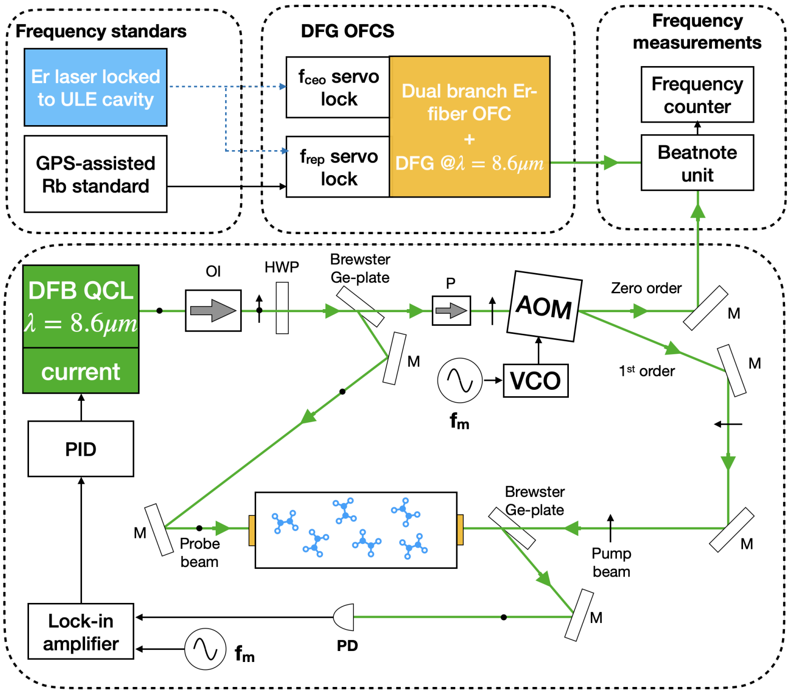

Figure 4.5: Absolute frequency QCL stabilisation by modulation transfer setup. The absolute frequency reference is a sub-Doppler absorption of the CHF_3 molecule. The vertical and the horizontal linear polarization states are represented by black dots and arrows, while circular polarization is represented by a clockwise arrow. OI: optical isolator; HWP: half-waveplate; M: plane mirror; P: polariser; PID proportional-integrative derivative servo controller; AOM: acousto-optic modulator; VCO: voltage controlled oscillator; PD photodetector.

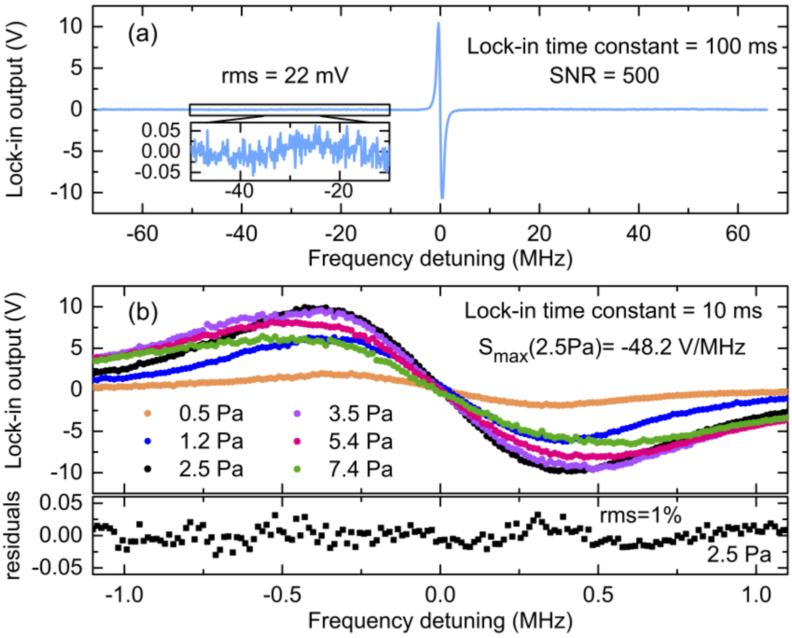

Figure 4.6: Modulation transfer signal of a saturated absorption transition of CHF_3 obtained with the QCL phase locked to mid-infrared OFC. a) 140 MHz frequency scan obtained with the frequency comb locked to the GPS disciplined Rb clock (CHF_3 at 2.5 Pa). b) 2.5 MHz scan obtained with the frequency comb locked to the ULE cavity for different CHF_3 pressure (bottom panel: normalized fit residuals of the modulation transfer signal).

is extracted by a second Ge-window at Brewster's angle placed after the cell, and it is focused on a liquid-nitrogen-cooled HgCdTe detector (1 MHz bandwidth, PD_{MT}).

To implement modulation transfer, the pump beam needs to be modulated. This is done by applying a frequency modulation at a rate of 260.42 kHz (800 kHz modulation depth) to the AOM over the 50 MHz control signal. Modulation transfer signal is retrieved by synchronous detection at the fundamental modulation frequency by a lock-in amplifier connected to PD_{MT}. This signal is then used to frequency lock the QCL to the saturated absorption of CHF_3 by a PID controller closing the loop over the QCL current controller.

The absolute frequency measurement of the laser and its stability performance are obtained by comparison with an optical frequency comb. In particular, the zero-order transmission of the AOM is combined with a DFG mid-infrared optical frequency comb centred at 8.6 μm (section 3.2.2).

4.2.2 Experimental results

Fig. 4.6 shows the modulation transfer signal recorded at the output of a lock-in amplifier acquired with a time constant of 100 ms. The recorded line is identified as ${}^{r}R_{44}(62)$, a ro-vibrational transition belonging to ν_5 band of CHF_3 (line centre frequency 34 751 860 MHz). In particular, Fig. 4.6(a) presents a 139 MHz span obtained with the QCL phase-locked to the optical frequency comb frequency (section 3.2.4) referenced to a Rb clock. The scan is performed by keeping the locking and scanning the repetition rate of the frequency comb. It is worth noticing the flat baseline outside the saturation profile. This is possible thanks to modulation transfer technique, sensitive only to non-linear absorption feature which rejects contributions from any liner absorption profile (at 8.6 μm, the room temperature Doppler width of CHF_3 lines is 50 MHz). By comparing the peak to peak signal and the rms value outside the peak, it is possible to determine a signal to noise as large as 500 (100 ms lock-in integration time and 2.5 Pa of gas pressure).

In the proximity of sub-Doppler line centre, it is recorded the modulation transfer signal with a much higher frequency stability of the optical frequency comb, by locking it to an ultra-low expansion (ULE) optical cavity. This optical reference consists in an ultra-stable Fabry-Pérot cavity created inside a glass designed with a ultra-low thermal expansion coefficient (10^{-8} K^{-1}). In this case, to scan the comb repetition rate, the frequency of the ULE-cavity-locked Er laser is tuned by an additional AOM frequency shifter while keeping the carrier–envelope offset at a fixed value of 10 MHz. Fig. 4.6(b) shows modulation transfer signals recorded for different pressures of CHF_3, from 0.5 Pa to 7.4 Pa. The frequency resolution is 10 times finer than Fig.4.6(a), passing from 137 kHz to 13 kHz. The model employed to fit each profile is based on frequency modulation of a Lorentzian profile in presence of residual amplitude noise. For a CHF_3 pressure of 2.5 Pa, the modulation transfer spectroscopy shows the highest slope at the line-centre frequency of -48.2 V/MHz, a RAM of 0.1%, and a linewidth, full-width at half-maximum, of 1.07 MHz. The retrieved pressure and pump power line broadening coefficients are 63 ± 5 kHz/Pa and 15 ± 5 kHz/mW, respectively.

By using a proportional-integrative-derivative (PID) servo controller acting on the driving current, the modulation transfer signal is used to frequency lock the QCL against the centre of the saturation profile.

Fig. 4.7 displays the RF spectrum (900 Hz resolution) of the beatnote signal between the QCL and the frequency comb, before and after frequency locking to modulation transfer signal. In free running, or better in a low gain locking, the beatnote signal has a 3 dB linewidth of 200 kHz; by increasing the gain and control loop bandwidth the beatnote shrinks down to 11 kHz (observation time 100 ms). This value is limited by the 100 kHz bandwidth of the system, limit imposed by the modulation frequency adopted in this experiment.

QCL frequency stability is characterized by measuring Allan deviation (non-overlapping two-sample deviation) of the beatnote signal versus the integration time, τ , of the used reciprocal (Π) frequency counter.

Fig. 4.8 illustrates the comparison between two different references used to stabilise the optical frequency comb. In the first case, the frequency comb is stabilised with the GPS disciplined Rb clock. Here, the beatnote stability follows the stability of the adopted reference clock, demonstrating that the QCL stabilised against saturated absorption transition is more stable than the frequency comb. In the second case, the frequency comb is stabilised against a ULE cavity. Now, the beatnote short term stability is more than one order of magnitude smaller, starting from a

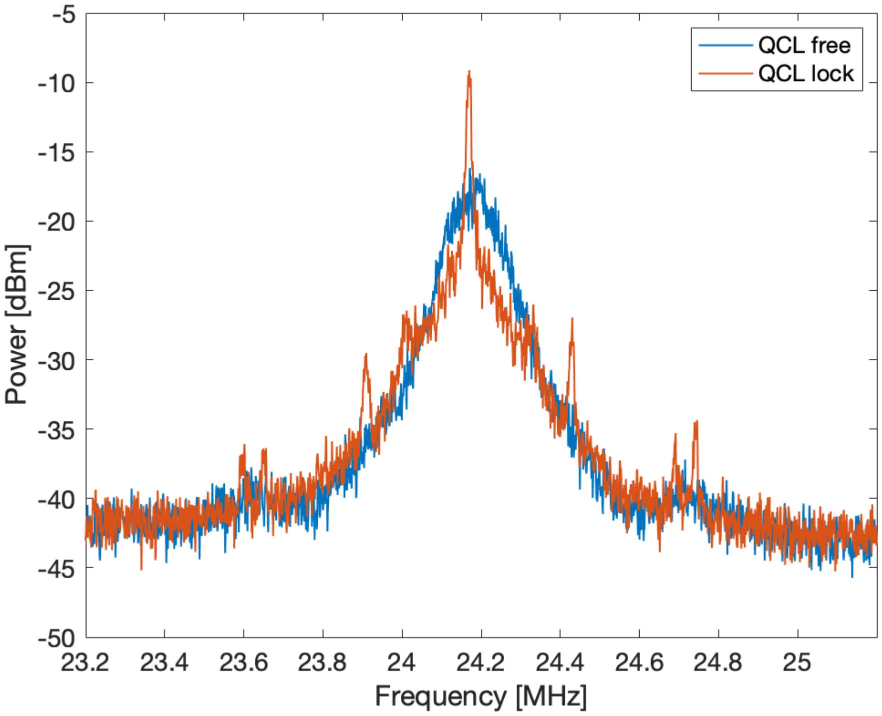

Figure 4.7: Radio frequency spectrum of the beatnote signal between the QCL frequency locked to CHF_3 sub-Doppler transition and the optical frequency comb referenced to the ULE cavity (red curve), in comparison with the free running QCL (blue curve).

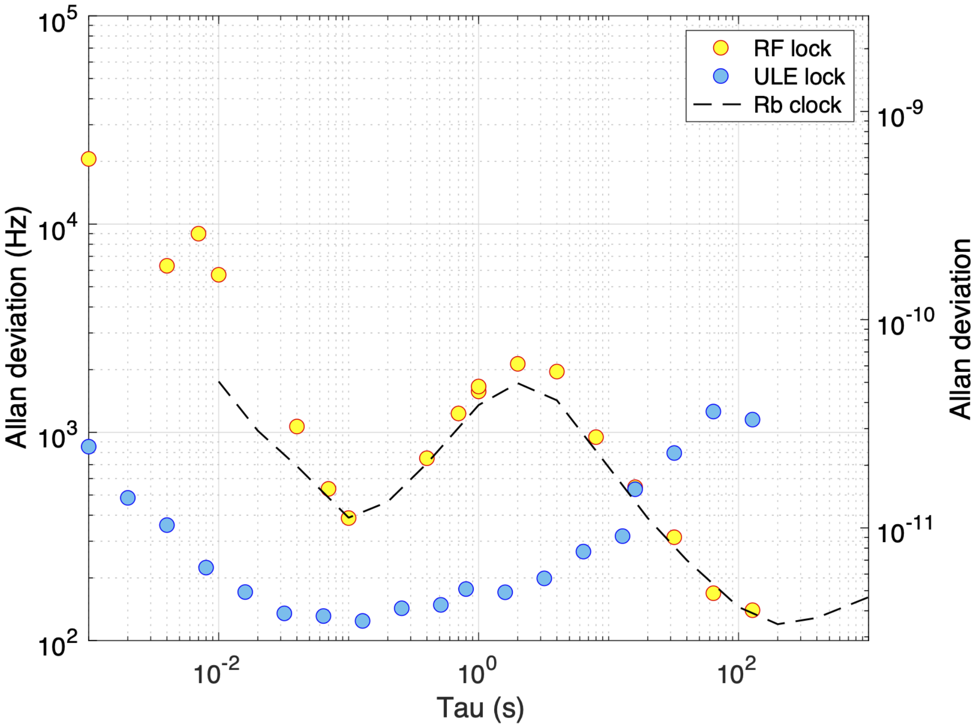

Figure 4.8: Allan deviation of the beatnote signal between the stabilised QCL and the mid-infraed OFC versus the integration time (Yellow: mid-infrared OFC locked to the Rb clock; Blue: mid-infrared OFC locked to the ULE cavity; Black: Rb clock stability).

fractional level of 2×10^{-11} at τ =1 ms and it follows a white frequency noise law $6 \times 10^{-13}\tau^{-1/2}$ until 100 ms. For longer integration times, up to 10 s, the Allan deviation is still lower than the one measured in the RF referencing scheme. The stability then worsens due to the linear drift of the ULE cavity, corresponding to a fractional deviation of $5 \times 10^{-13}\tau$ (as measured with respect to the Rb-self-referenced comb).

4.2.3 Uncertainty budget

In order to further investigate systematic effects that can affect frequency accuracy of the QCL locked to the sub-Doppler profile, sensitivity coefficients of the line-centre frequency with respect to gas pressure, pump and probe powers, and modulation parameters are measured. Fig. 4.9 shows the beatnote frequency dependence as a function of CHF_3 pressures and pump power levels, respectively. The pressure shift presents a linear trend with a slope of 7.7 kHz/Pa. The observed power shifts seems better approximated by a quadratic function. Because of this, it have been chosen to work ar around of 5.25 mW where the pressure shift can be approximated by a linear slope of -6.0 kHz/mW. Also probe beam power have been tested but no significant shift have been observed.

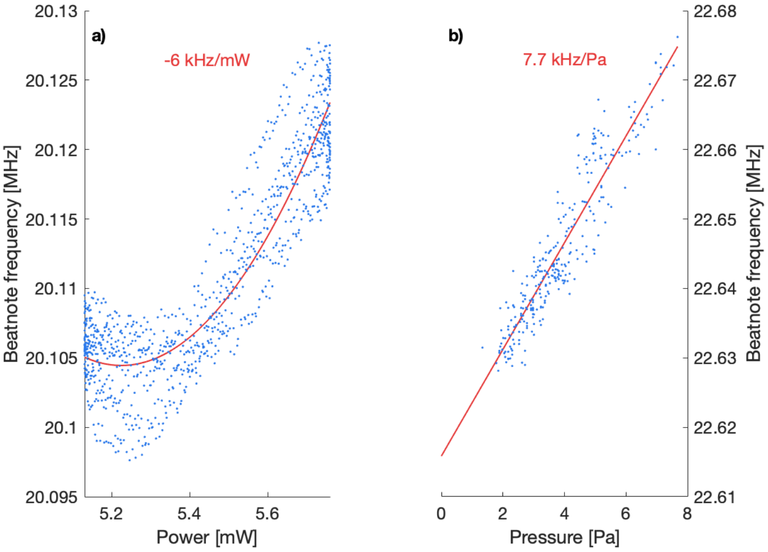

Figure 4.9: QCL-OFC beatnote shift as a function of QCL power (a) and CHF_3 pressure (b). Red line indicates the best fit.

Dispersion profile fittings (Fig.4.6) allow to estimate the residual amplitude modulation (RAM) contribution due to the acousto-optic modulator. This effect modifies the dispersion profile and, in particular, it changes the zero-crossing frequency of the modulation transfer signal. The retrieved frequency offset is estimated in 20 kHz/%RAM [97][98], which, assuming RAM at a level of 0.1%, contributes to the uncertainty of the frequency standard at a level of 5.8×10^{-11}.

Another uncertainty effect is related to the pump and probe beams overlap. The estimated parallelism error is about 0.5 mrad, which leads to an absolute frequency uncertainty of 1.6 kHz (4.6×10^{-11}) [99]. Other effects such as Zeeman shift, splitting of photon recoil doublet, second-order Doppler shift, gas lens effect, and black-body radiation shift give negligible contributions to the systematic uncertainty, with a maximum fractional value of $\sim 10^{-12}$ for the gas lens effect.

In order to verify for repeatability, several measurements are repeated at the same nominal operating parameters ($p = 2.50 \pm 0.03$ Pa, $P_{\text{pump}} = 5.25 \pm 0.05$ mW, $P_{\text{probe}} = 0.25 \pm 0.01$ mW, T=297.5 ± 0.5 K, f_m =260 kHz, and Δf =800 kHz) over several days. For this test, all the parameters are reset and restored to the nominal operation value. In all these measurements, for synthesizers and frequency counters, as well as for the frequency comb, the employed frequency reference was the GPS-disciplined Rb clock, which ensures the best performance in the long term stability.

Fig. 4.10 reports the result of this test, with the result of 18 independent measurements of the absolute frequency of the QCL. Each of them is the average of 10 consecutive data obtained with an integration time of 100 s. The overall unweighted average of the QCL stabilized frequency is 34 751 885 064.9 kHz. The statistical uncertainties results in 11.9 kHz, corresponding to a fractional accuracy

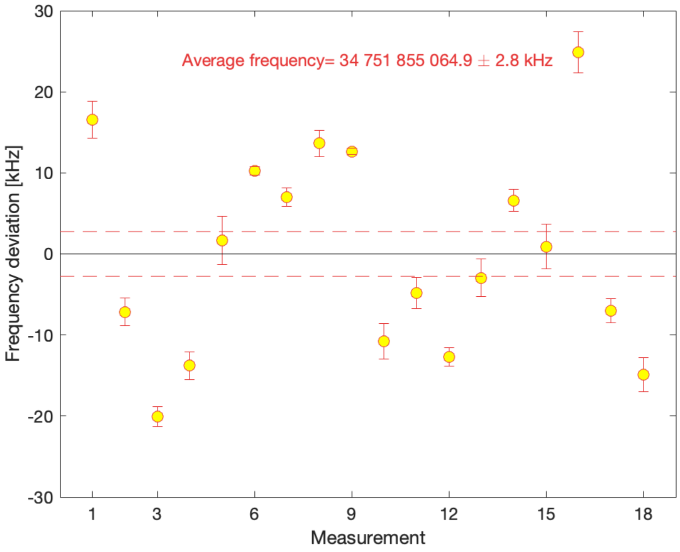

Figure 4.10: CHF_3 line-centre frequency measurements repeated using the same nominal experimental parameters.. Each point represents the average of 10 samples at 100 s of integration time, with the errorbar corresponding to the standard deviation of this measurements. The dashed red line is the uncertainty of the average value.

of 3.4×10^{-10}.

Table 4.2 summarizes the uncertainty budget in the measurements of the absolute frequency of the realized QCL standard, the result is an overall fractional uncertainty of 34.8×10^{-11} or 12 kHz in absolute terms.

By considering a corrections of +25 MHz for the Doppler shift and a correction of +19 kHz due to pressure shifts, the line centre frequency of the CHF_3 ro-vibrational transition is 34 751 860 046 ± 12 kHz.

Parameter	Coefficient	Uncertanty (10^{-11})
CHF_3 pressure	7.6 kHz/Pa	0.7
Power	-6 kHz/mW	0.9
Electronic offset	21 kHz/V	1.2
RAM	20 kHz/1%	5.8
Rb clock(100s)		0.4
Pump/probe overlapping		4.6
Statistics(repeatability)		34
Combined uncertainty		34.8

Table 4.2: Measured and estimated uncertainty budget relative to frequency stabilisation of a QCL to CHF_3 ${}^{r}R_{44}(62)$ absorption line by modulation transfer[7].

Chapter 5

Scanning micro-cavity resonator (SMART) direct-comb spectroscopy

Direct comb spectroscopy allows to use all the frequency comb as a probing beam in order to excite several transitions at the same time. Thanks to its broadband nature and its absolute frequency accuracy, direct-frequency-comb spectroscopy is nowadays considered a fundamental tool in many applications of science and technology for high-fidelity mapping of atomic and molecular transitions. However, in order to acquire its broad spectrum and accessing its absolute precision, a spectrometer is needed with a sufficient high-resolution to resolve the single comb mode. If this is the case, direct comb spectroscopy resolution is set by the comb repetition frequency, but the accuracy can be much better, down to the single comb mode linewidth making negligible the instrumental line shape. Dispersive spectrographs are a simple and robust tool for parallel acquisition of the broadband frequency comb but, most of the time, they do not have a sufficient resolution to resolve single comb-mode. In order to exceed the spectrograph resolution limitation, Fabry–Pérot filter cavities can be used to increase the comb line spacing and relax the spectrograph resolution requirements.

5.1 Principles of SMART direct-comb spectroscopy

One of the possible spectrometers that can resolve the single comb mode is based on a scanning Fabry–Pérot micro-cavity resonator, SMART DFCS (Scanning Micro-cAvity ResonaTor Direct Frequency Comb Spectroscopy) [8].This approach can be seen as a simplified version of Vernier spectroscopy.

Vernier spectroscopy [59] is based on the matching between a frequency comb repetition frequency, f_{rep}, with a Fabry–Pérot cavity free spectral range, FSR. The matching is usually kept with a scaling factor m such that f_{rep}/FSR= $m/(m-1)$, in this way the cavity is resonant with only some of the modes of the frequency comb making possible to resolve them with a dispersive spectrometer, like a grating. Then, by changing the cavity length, it is possible to change the resonant condition and obtaining another group of comb mode at the output of the resonator. A tilting mirror synchronous with the scanning of the Fabry–Pérot cavity and a CCD camera are used for the detection. The two-dimensional map generated on the camera will have one direction corresponding to the dispersion spectrometer and a second dimension given by the cavity scanning.

SMART technique has a very similar approach but it relies on a micro-cavity with a high FSR, so high that only few comb modes can be resonant at each time.

An optical frequency comb with frequency $\nu_{comb} = f_{\mathrm{CEO}} + n f_{\mathrm{rep}}$, where f_{CEO} is the comb offset frequency, f_{rep} is the comb line spacing, and n is the order of the comb line, is coupled to a Fabry-Pérot micro-resonator. This resonator is characterised by a free-spectral-range FSR$= c/(2d) \gg f_{\mathrm{rep}}$, where d is the mirrors separation and c is the speed of light and a cavity Finesse, $F \approx \pi R/(1-R)$ being R the mirror reflectivity. By designing a cavity with FSR$\gg f_{\mathrm{rep}}$ and FSR$/F < f_{\mathrm{rep}}$, it results that only few comb modes can be resonant with the cavity at a given length d. Moreover, given a frequency comb with a bandwidth $\Delta\nu_c$, if FSR$> \Delta\nu_c$ only one comb mode is resonant at a given time. In this way, it is possible to record all the frequency comb spectrum by scanning the cavity length. Since fo many experimental application, the optical bandwidth of the frequency comb is bigger then the cavity FSR, spectral aliasing can occur. For this reason, a low dispersion grating is added after the cavity in order to detect a single Fabry–Pérot resonance on the detector. In addition, it is possible to detect the whole comb spectrum by replacing the single detector with an array.

The SMART approach reduces the system complexity since it does not rely on a precise matching of cavity length and repetition frequency. In addition, it allows a direct implementation of this method to any spectral region from 20 μm to 200 nm. A further spectral extension down to THz region will be feasible in the next years when high-finesse THz resonators will be available.

5.2 Experimental setup

Fig. 5.1 shows the implemented SMART setup based on a commercial Er-fiber optical frequency comb, a narrow-linewidth distributed-feedback (DFB) Er-fiber laser, a scanning microresonator and a reflective diffraction grating (600 grooves/mm) [9].

The optical frequency comb is the same of section 3.2.3 a dual-branch Er-fiber femtosecond laser with repetition rate of 250 MHz (frequency stabilised against the GPS disciplined Rb clock), an optical bandwidth from 1500 to 1600 nm and an average output power of 500 mW. In this case, one the outputs is used to detect and stabilise, by self referencing, the carrier envelop offset frequency. This is done by coupling the output to a highly-nonlinear fiber for octave spanning supercontinuum generation (from 1000 to 2100 nm). The part around 1000 nm is frequency doubled and it is recombined with the supercontinuum in a photodetector. The generated beatnote, corresponding to the CEO frequency is then stabilised to with respect to the Rb clock.

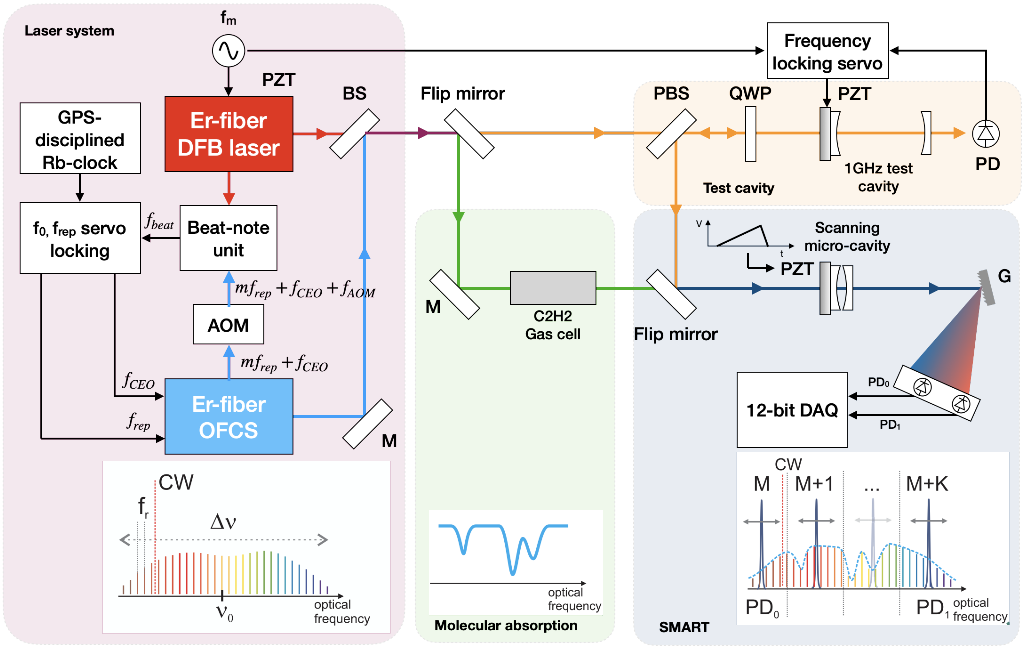

Figure 5.1: SMART spectroscopy experimental setup. OFCS: optical frequency comb synthesiser; PZT: piezoelectric trasducer; BS: beam splitter; f_m frequency synthesiser; M: plane mirror; PD: photodetector; G: diffraction grating; PBS: polarizing beam splitter;. AOM: acousto-optic modulator; DAQ: data acquisition system.

The second amplified output is used as probing beam for the SMART experiment. An additional fiber-coupled CW single-frequency laser is used in the experiment. This narrow linewidth (100 kHz at 1 ms integration time), tunable (from 1440 to 1650 nm) laser is providing a frequency reference for the absolute frequency calibration of the smart technique. The two lasers, the frequency comb and the CW, are combined in a fiber coupler and then sent through an aspherical fiber collimator to the Fabry–Pérot scanning micro-resonator. This last element is constituted by two spherical mirrors with a radius of curvature 1 meter, separated by 250 μm. The cavity finesse is 50 000 ($T = 0.005\%$ at 1540 nm), FSR is 600 GHz and transmission modes linewidths are 12 MHz.

By applying a linear voltage ramp to the piezoelectric transducer (PZT) on one of the two mirrors is then possible to frequency sweep the transmission mode of the cavity.

Since optical frequency comb bandwidth is larger than the cavity FSR, different comb modes can be resonant with different modes of the Fabry–Pérot . In order to avoid spectral aliasing, the micro-cavity output is dispersed by a reflective diffraction grating and then detected on two separate InGaAs photodetectors. A first detector, PD_0, is collecting a part of the comb spectrum containing also the CW-laser. This corresponds to M-th order of the cavity. The second detector, PD_1, mounted on a translation stage, can be aligned to detect another Fabry–Pérot mode, $M + K$. The two detectors are then sampled by a 12-bit digital oscilloscope with a sampling rate of 25 MS/s and processed by a computer.

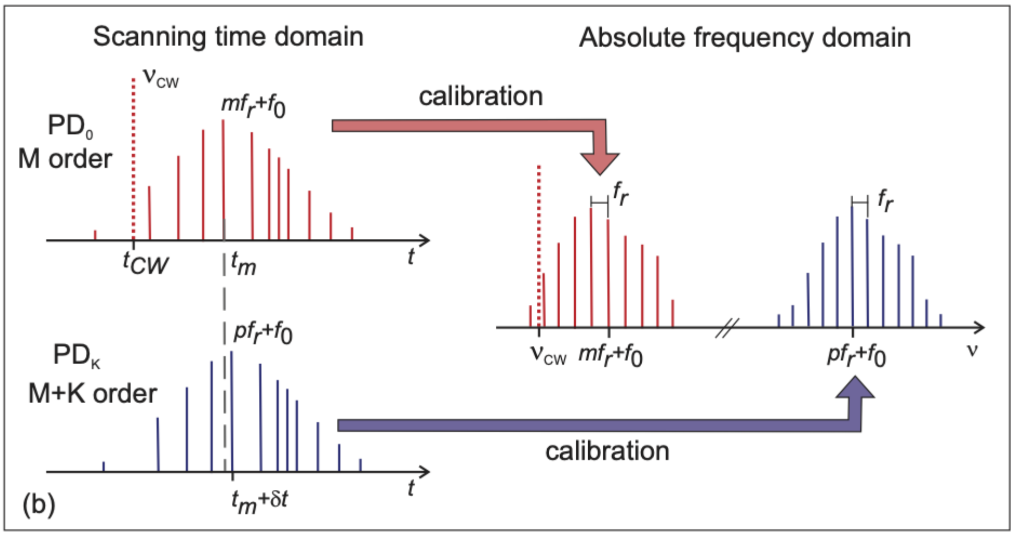

Figure 5.2: Scanning-time to absolute-frequency calibration principle.

With this measuring setup, two different experiments are performed: a first one focused on resolution and a second one on bandwidth.

In order to test the resolution, a second Fabry–Pérot cavity is aligned in the setup. This test cavity is a plano-concave resonator with 1-GHz FSR and a nominal cavity Finesse of 2500 corresponding to a 400 kHz linewidth. Resonator mirrors have nominal reflectivities of 99.9 and 99.98% for the plane and concave (1 meter radius of curvature) surfaces, respectively. The second surface of the curved mirror is anti-reflection coated, whereas the input surface of the plane mirror is uncoated with Fresnel reflection coefficient of 3.3%.

The spectroscopy of the test cavity is performed by interleaving several spectra taken in successive measurements with a different detuning between the frequency comb and the test cavity. To ensure no frequency drift and to remove any low noise perturbation during the measurement time, a lock chain is set. One resonance of the test cavity is frequency locked to the CW Er-fiber laser. The locking is performed by applying to the laser a frequency dithering (100 kHz modulation frequency and 100 kHz modulation depth) to its PZT actuator and closing the feedback control loop on the test cavity PZT. In addition, to finely tune the optical frequency comb around the test cavity resonances, a frequency-shifted replica of this is also stabilized with respect to the CW Er-fiber laser using the beatnote signal with one tooth of the frequency comb. The frequency shift is provided by an acousto-optic modulator. By closing the loop on the frequency comb repetition frequency, thanks to its intra-cavity electro-optic modulator, it is possible to keep the relation $(\nu_{comb} + f_{AOM}) = (mf_{\text{rep}} + f_{\text{CEO}} + f_{AOM}) = \nu_{cw} + f_{beat} = N\text{FSR}$. In this way, by changing AOM frequency by 1 MHz, it is possible to finely scan the frequency comb across the calibration Fabry–Pérot resonance and, by successive measurements, to record the cavity reflection by SMART technique.

The second experiment, testing the bandwidth capability of the system, is performed by adding a 10-cm-long acetylene gas cell (filled at 50 mbar pressure) before the scanning microcavity (and by removing the test cavity of the previous experiment). The $\nu_1 + \nu_3$ ro-vibrational bands of acetylene (C_2H_2) are around 1.55 μm. The scanning micro-cavity transmission, dispersed by a diffraction grating, is measured by two photodetectors PD_0 and PD_1.

PD_0 is measuring the M-th mode of the cavity, which corresponds to the mode that can be resonant also with the CW-laser. Starting from this known frequency, the frequency axis can be reconstructed. The closest comb mode can be assigned by knowing the beatnote frequency with the CW laser. And any other comb mode can be assigned by adding multiple of the repetition rate. In this way, any non-linearity of the scan can be corrected. This absolute assignment is straightforward to do on PD_0, due to the presence of the calibration CW-laser. On PD_1, instead, it is possible to correct the scan non-linearity due to the equidistant mode of the frequency comb but, in principle, it is not possible to assign an absolute frequency, since there is not a frequency reference to disambiguate comb mode number. This limitation can be overcome by taking in consideration that also the Fabry–Pérot modes are periodic. Since the absolute frequency of the M-th order of the scanning micro-cavity, thanks to PD_0 is known, it is possible to reconstruct also the frequency of any other $M + K$ order by simply adding a multiple of the FSR (Fig. 5.2). In this way, all the spectra measured by different photodetectors can be calibrated with absolute precision. Once absolute calibration is achieved, coherent averaging is possible with the consequence of increasing SMART sensitivity.

5.3 Experimental results

The ultimate frequency resolution of the SMART technique is characterised by measuring the period narrow-linewidth resonances of a test Fabry-Pérot cavity (1GHz FSR).

Fig. 5.3 shows the photodetector voltage as a function of time. This represents one transmission order of the micro-cavity resonator, with each line corresponding to a frequency comb mode. The single mode are well resolved, each of them with a linewidth of 12 MHz, corresponding to the instrumental line shape (micro-cavity resonance linewidth).

From Fig. 5.3(b), it is possible to notice that not all the comb modes have the same amplitude, precisely, one every four modes has a lower intensity. These correspond to the test-cavity resonances, which "absorbs", or better transmits some comb modes. Since the repetition rate is 250 MHz and the test-cavity FSR is 1 GHz, this corresponds to the ratio 1 to 4.

By using each comb mode as a frequency marker, each of them corresponding to a frequency distance equal to the frequency comb repetition rate, it is possible to reconstruct the micro-cavity scanning during the measurement. Fig 5.4 shows the mirror distance as a function of time with a linear fit. The residuals show an overtone modulation present during the scanning.

Going back to the test cavity measurement, the amplitude of each comb modes is used as a sampling point in order to reconstruct its reflection profile. 28 different

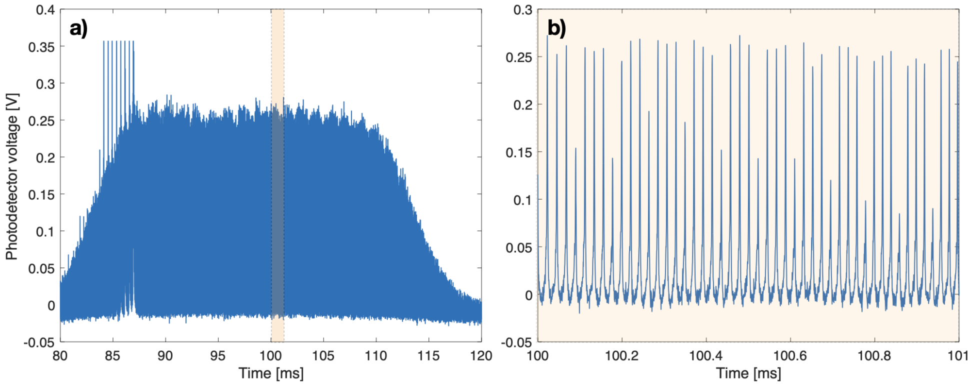

Figure 5.3: Micro-resonator transmission versus scanning time. a) All the spectrum detected by PD_0. b) Detailed zoom at t=100 ms, where cavity resonance can be distinguished as a decrease of the transmission.

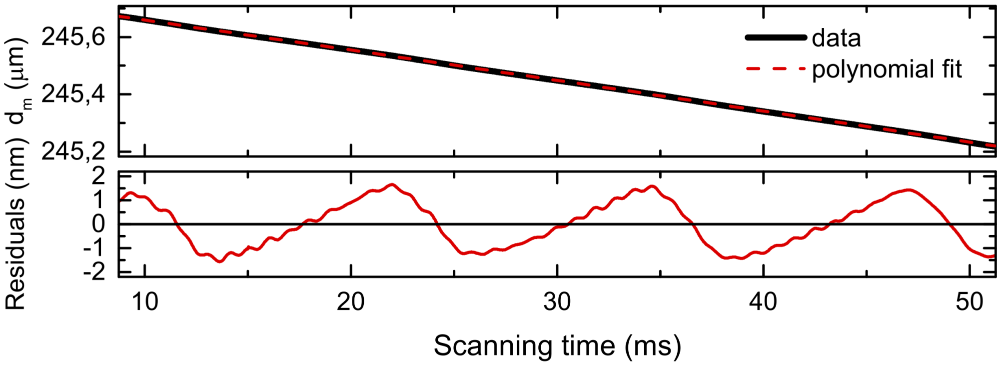

Figure 5.4: Micro-resonator mirror separation versus scanning time, d_m, as retrieved by the absolute frequency calibration of the PD_0 spectrum (black data). The dashed red-line represents the best fit with a 2-order polynomial function (fit residuals are reported in the bottom panel).

measurements are performed, and for each of them, the offset between the locked test cavity and the frequency comb is changed. Fig. 5.5 shows the result of these successive scans, each of them averaged 50 times. The reconstructed reflection profile presents a periodic set of narrow features corresponding to the periodic resonance of the test cavity. Each of these resonances is 1 GHz apart from each other, and the whole structure presents a sinusoidal-like modulation of the minima in the range between 40 and 60%.

This modulation is attributed to the 3.3% reflectivity of the first surface of input mirror of the test-cavity, that with a refractive index of 1.44 and a thickness of 6.35 mm., matches the periodicity of the modulation (≈16 GHz).

Each cavity mode is fitted using a complex Lorentzian profile, resulting from possibility of phase mismatch between the beam reflected at the input mirror and the beam reflected by the cavity [100]. Fig 5.6 shows an example of this fitting. Residuals of the fitting are limited by noise, with a rms value around 1%. From the analysis of multiple reflection profiles, a FWHM modulation is discovered (Fig. 5.7). This modulation matches with the amplitude modulation cited before. It turns out that the residual reflectivity of input mirror transfers to a modulation of cavity Finesse and, as a consequence, on the resonance linewidth. The averaged linewidth is 420 kHz with a mean fit uncertainty of 33 kHz (1 σ).

To better estimate the possibility of frequency distortion introduced by the SMART technique, a fit with a complex Voigt profile, instead of a complex Lorenzian, have been performed. The frequency comb tooth linewidth can play a role by introducing a Gaussian instrumental lineshape. However, the retrieved Gaussian (FWHM) linewidth contribution to the Voigt profile is 20 ± 44 kHz, i.e., consistent with a zero result. In the worst case, assuming the deviation of the Gaussian linewidth as the instrumental contribution, the ultimate resolution of the implemented SMART method would be at the 44-kHz level. This result is perfectly compatible with comb tooth linewidth, measured in previous works in the range between 20 kHz and 50 kHzf or observation times from 1 to 10 ms [101].

The second part of the experiment aims to test the broad-bandwidth capability of the SMART technique. In this case, the target is a 10 cm-long acetylene gas cell at 50 mbar. Two detectors are placed after the SMART cavity, one in correspondence of the CW reference laser, PD_0, and a second one in correspondence of a different cavity order PD_1,.

Fig. 5.8 shows the two photodetector signals measured as a function of time, while scanning the microcavity length with a maximum span $\Delta d \approx 0.5$ μm in 40 ms. Again, the comb modes, as well as the CW laser, are well resolved and they present an instrumental linewidth of 12 MHz. Absorption features of the C_2H_2 gas are clearly visible as a modulation of the comb spectrum detected by, PD_1.

The calibration algorithm is applied to reconstruct the frequency axis. The CW laser, with a frequency stability better than the comb repetition rate, fixes the order of the closest comb mode, n_{CW}, as $n_{CW} = (\frac{\nu_{CW} - f_{\mathrm{CEO}}}{f_{\mathrm{rep}}})$. Starting from this mode every other comb mode of PD_0 can be uniquely determined as $\nu_{comb} = (n_{CW} + q) f_{\mathrm{rep}} + f_{\mathrm{CEO}}$, with q integer number. Each of these frequencies correspond also to a time instant of the scanning as $\nu_{comb} = (M) FSR(t)$. Starting from this

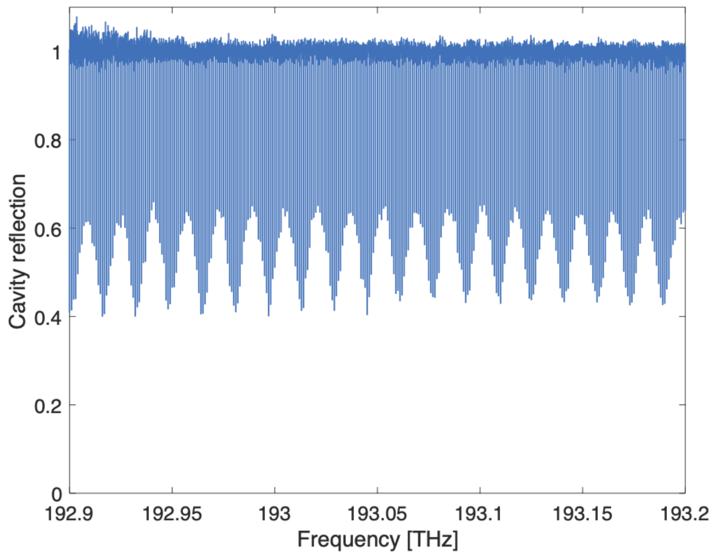

Figure 5.5: Test-cavity reflection measured by SMART spectroscopy.

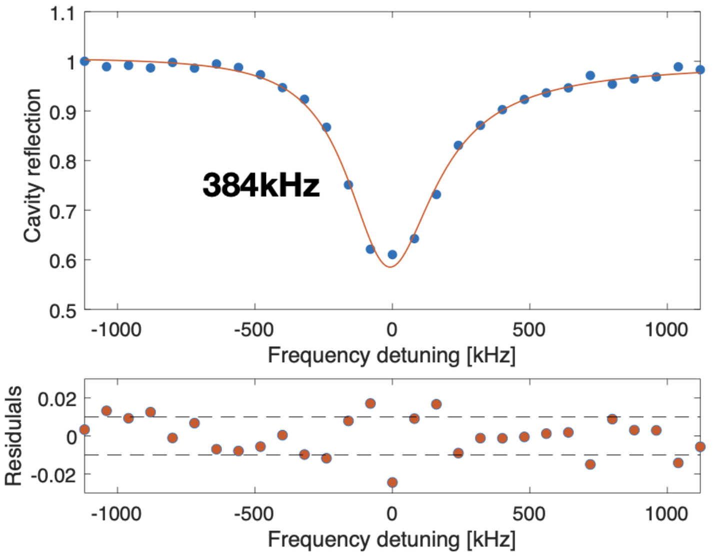

Figure 5.6: SMART measured reflection profile (blue dots) fitted by a complex Lorentzian function (red line). Residuals are plotted in the bottom figure, grey dashed lines indicate the rms residuals ≈1%.

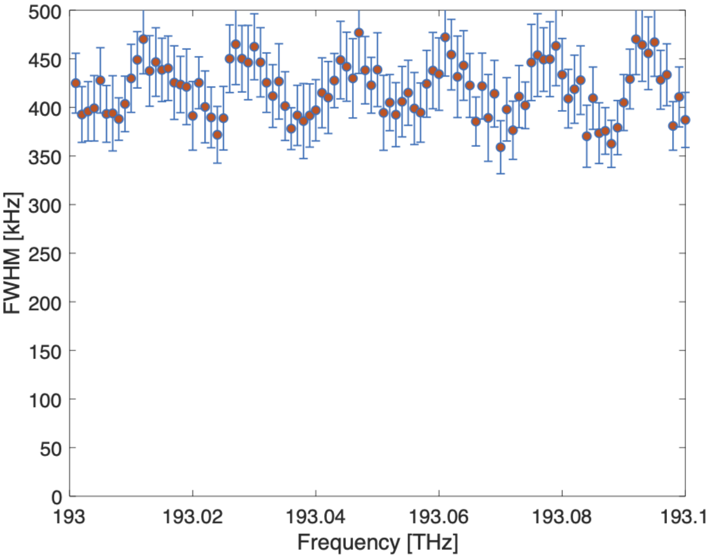

Figure 5.7: Fitted linewidth full width at half maximum, FWHM, for several cavity resonances as a function of the optical frequency.

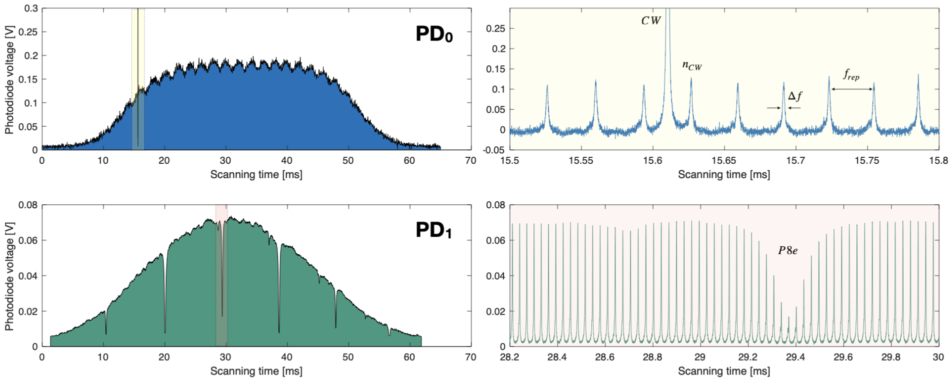

Figure 5.8: Left panels: micro-resonator transmission versus scanning time detected by PD_0 top and PD_1 bottom. For PD_1, several absorption profiles of the P-branch of the C_2H_2 are visible as holes in the frequency comb spectrum. Right panels: highlighted part of the left panels. For PD_0,the CW laser and the single comb modes are shown. For PD_1, a detailed the absorption line $\mathrm{P8_e}$ of C_2H_2 is presented.

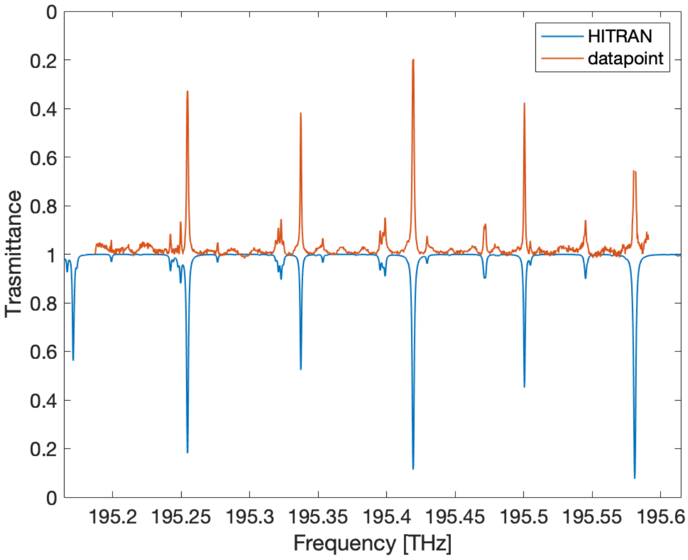

Figure 5.9: Recorded transmission spectrum from 10-cm long gas cell of C_2H_2 at 50 mbar (blue curve), together with the HITRAN simulation (red curve).

first detector calibration, every other micro-cavity mode scanning can be defined as $\nu = (M + K)\mathrm{FSR}(t)$, being K an integer. Since there is not any particular matching between frequency comb and scanning micro-cavity, two different detectors do not detect a comb mode at the same time. Time instants between two comb modes are linearised and successive frequency assignment can be adjusted rounding the frequency to the closed integer order q that matches the condition $\nu_{comb} = (n_{CW} + q)f_{\mathrm{rep}} + f_{\mathrm{CEO}}$.

Fig. 5.9 shows the calibrated transmission feature of the acetylene in comparison with HITRAN simulation, demonstrating a good matching of the absorption features. By moving the second detector PD_1 to different positions, it is possible to record different micro-cavity transmission orders. After recalibration, the result is presented in Fig. 5.10(a), for $M = 317$ and $K = 2, 3, 4, 5, 6$. Each of the main lines from these four bands is fitted by using absorption parameters (like line-strength, line centre, pressure broadening coefficient).

Fig. 5.10(b) reports the line centre frequencies of the main absorption line of C_2H_2 recorded in the four spectral bands measured for this experiment. The standard deviation of the error compared to HITRAN database is 2.2 MHz. A limited signal to noise ratio and a residual baseline modulation are the main causes for this uncertainty.

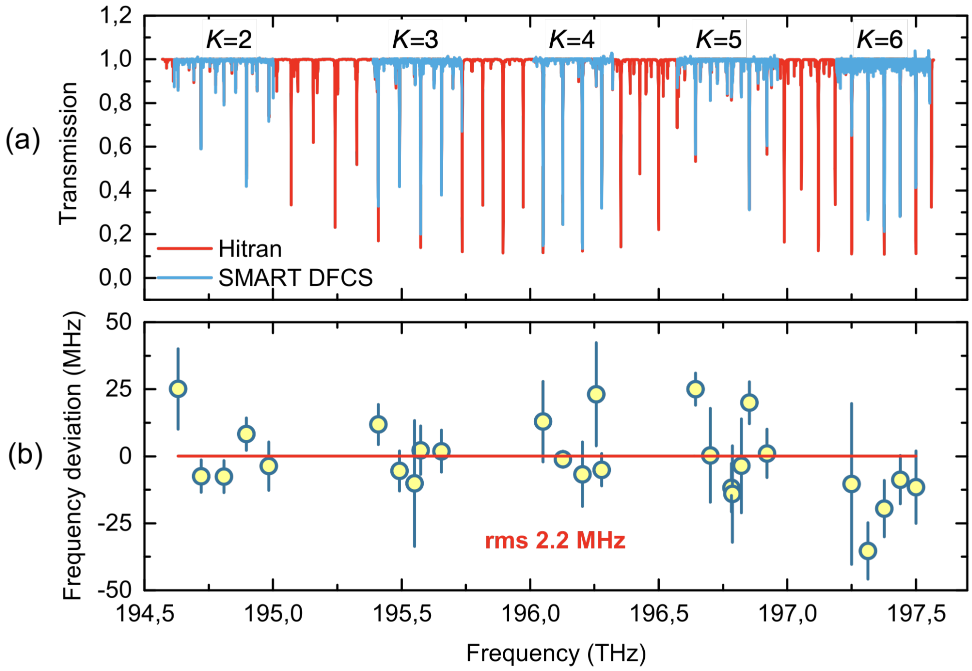

Figure 5.10: a) Transmission spectrum of 10-cm long gas cell of C_2H_2 at 50 mbar. Blue: Spectra measured by SMART spectroscopy, corresponding to micro-resonator transmission orders $M + K$ with $M = 317$ and $K = 2, 3, 4, 5, 6$. Red: HITRAN database simulation. b) Frequency deviation between retrieved acetylene line centre frequencies and HITRAN database (yellow dots). The errorbar corresponds to the fitting error (1σ).

Chapter 6

Dual-comb hyperspectral imaging

Dual-comb spectroscopy combines advantages of broadband spectroscopy and tunable laser spectroscopy into a single platform. It allows to interrogate and measure broad spectra by using a single detector, like in conventional Fourier transform spectroscopy, but it provides frequency resolution and accuracy of single frequency laser with a resolution set by the source rather than the instrument. Additionally, it presents some unique advantages, like the possibility of having a system free of moving parts and a resolution free from any geometrical constrains. Since its first demonstration, dual-comb spectroscopy has explored many different applications in many different spectral regions. It has been applied to precision metrology of molecular line centres [102][103], in microscopy even at sub-wavelength spatial resolution [104], to a spectral lidar [105][106], it has been expended in non-linear spectroscopy like stimulated Raman scattering [107], comb-based coherent anti-Stokes Raman spectroscopy [108], and two-photon spectroscopy [109].

Regarding hyperspectral imaging, dual-comb application has been limited, and its implementation has been restricted to mechanical sample scanning approach [107][110]. More recently, two experiments demonstrated the possibility to obtain a hyperspectral image by dual-comb spectroscopy without any moving part. The first one, exploited Hadamard structured illumination and single-pixel detection [111]; a second one demonstrated the first direct hyperspectral dual-comb imaging architecture in which interferograms were directly acquired by a camera [112][113]. In this experiment, the goal was to further increase spectral bandwidth and resolution, while keeping a parallel acquisition using a camera.

6.1 Principles of dual-comb spectroscopy

Dual-comb spectroscopy is an interferometric direct-comb technique that allows single comb-line detection over its whole bandwidth by using a single detector and without the needs of any moving parts. This technique requires two mutually coherent frequency combs with a slightly difference repetition rate which interferes on a photodiode. The interference generates a radio-frequency version of the starting optical frequency comb, creating a map one-to-one between optical and radio-frequency

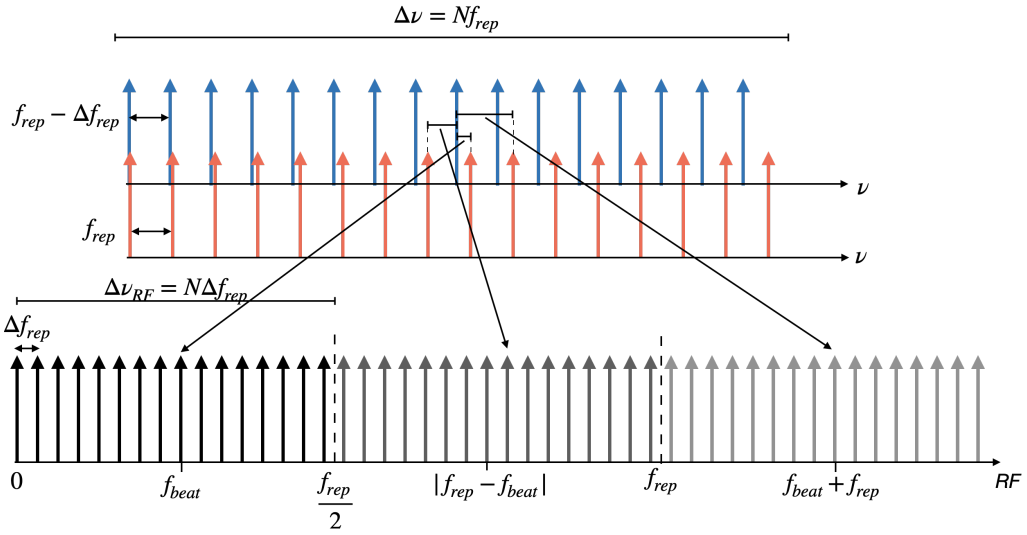

Figure 6.1: Dual-comb principle: red and blue arrow represent two frequency combs with repetition frequency f_{rep} and $f_{\text{rep}} + \Delta f_{rep}$, spanning a bandwidth $\Delta\nu$. Black and grey: beatnote between pair of comb modes.

domains. Because of this remapping, if one of the two optical combs interacts with a sample, recording spectral features, it is possible to recover the same information from the radio frequency comb.

Frequency remapping can be easily understood by looking at the two frequency combs into the frequency domain. A difference in repetition rate means a different mode spacing between the two combs. When they are combined on a photodetector, heterodyne beatnotes between pairs of comb modes are generated, each of these them at a different frequency. With two frequency combs, each of them represented by $\nu_{1,2} = n_{1,2} f_{rep_{1,2}} + f_{ceo_{1,2}}$, the beatnotes between pairs of comb modes result

$$f_{beat} = |\nu_1 - \nu_2| = |n_1 f_{rep_1} - n_2 f_{rep_2} + f_{ceo_1} - f_{ceo_2}| = |\widetilde{n}\Delta f_{\text{rep}} + \Delta f_{\text{CEO}} + \Delta\widetilde{n}\frac{f_{\text{rep}}}{2}|, \quad (6.1)$$

with $f_{rep_2} = f_{rep_1} - \Delta f_{\text{rep}} = f_{\text{rep}} - \Delta f_{\text{rep}}$, $\Delta f_{\text{CEO}} = |f_{ceo_1} - f_{ceo_2}|$, $\widetilde{n} = 0, 1, 2, ...$ and $\Delta\widetilde{n} = 0, 1, 2, ...$ This equation describes the generated radio frequency comb. The first term represents the down-converted version of the comb, with a new line spacing equal to the difference in repetition rate, Δf_{rep}, and with a centre equal to Δf_{CEO}, second term. The third term indicates that multiple copies of the starting frequency comb can be detected, each of them separated by half a repetition frequency. Because of this periodicity, if the difference in repetition rate is not chosen carefully, spectra aliasing can occur, meaning that multiple comb lines are remapped to the same radio frequency. If the frequency comb spans a spectral width $\Delta\nu$, the condition that needs to be satisfied is that all the comb modes $N = \Delta\nu/f_{\text{rep}}$ are fitting in between 0 and half of the repetition rate,

$$N\Delta f_{\text{rep}} \leq \frac{f_{\text{rep}}}{2}, \quad (6.2)$$

so that

$$\Delta f_{\text{rep}} \leq \frac{f_{\text{rep}}^2}{2\Delta\nu}. \tag{6.3}$$

Additionally, detector and sampling rate have to be chosen in order to be able to acquire the complete signal. If the detector bandwidth or its sampling rate can not reach $f_{\text{rep}}/2$, the right term of equation 6.2 should be replaced by the maximum frequency span, f_{max}, that the system is capable of.

$$N\Delta f_{\text{rep}} \leq f_{max}. \tag{6.4}$$

Because of the interferometric nature of dual-comb spectroscopy, in order to reach single comb mode detection, a minimum detection time is required so $T \geq 1/\Delta f_{\text{rep}}$. Because of Eq. 6.3, this means that there is direct trade-off between the optical bandwidth, the acquisition speed and the repetition rate.

Another aspect to be taken in consideration is the signal to noise ratio. As known from FTIR, signal to noise ratio scales as the square root of the acquisition time, SNR$\propto T^{1/2}$ [60], resulting in an additional factor to add in the trade-off balance for dual-comb spectroscopy.

In addition, in order to measure for a time T and averaging constructively, the two frequency combs should keep their mutual coherence for this time. Different strategies are possible. It is possible to generate a frequency comb starting from the same seed laser in order to keep common most of the noise sources. Alternatively, coherence time can be further extended by data post-processing.

In the case of spectrally resolved comb lines, each comb tooth provides a single independent spectral sample, with its amplitude and its frequency. In this way, the resolution is set by the repetition rate of the frequency comb. However, because each comb mode is much narrower than the repetition rate, there is minimal cross talk between adjacent spectral elements, i.e., no instrument line shape. This means that the fundamental resolution is set by the comb tooth linewidth a resolution that can be accessed by successive measurements obtained by scanning the frequency comb (for example by changing its offset frequency).

All these concepts can be easily extended from a single detector to an array of detectors (camera). In this case, every array element is recoding an interferogram, which can be Fourier transformed to obtain the spectrum. At this point, it is possible to create a hyperspectral map, a hypercube of information with the light intensity recorded at each point in space and at each frequency.

6.2 Experimental setup

The experimental setup is sketched in Fig. 6.2. The two comb lasers are generated with an all-fiber electro-optic set-up followed by non-linear spectral broadening. A continuously tunable laser, emitting from 1530 nm to 1620 nm, with 50 mW of output power, is split in two arms, each of them generating one of the two frequency combs. The first stage consists in an electro-optic intensity modulator (EOM). The EOM is controlled by a electrical pulse train generator, creating pulses of 50 ps with

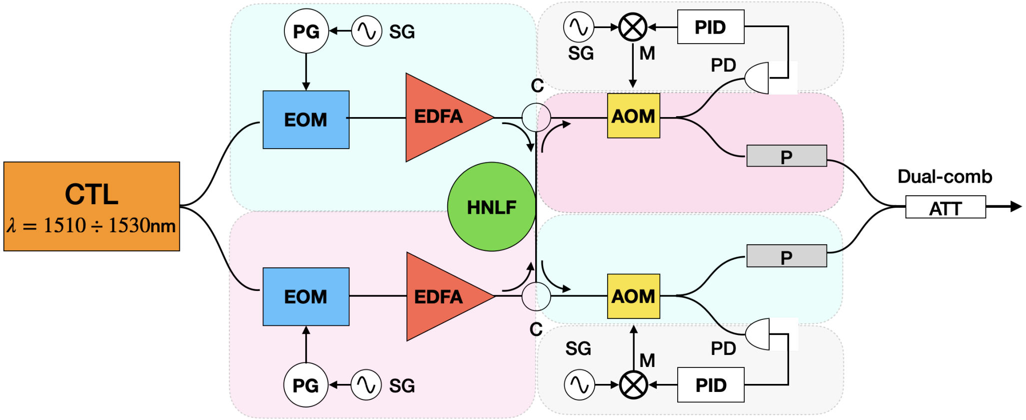

Figure 6.2: Dual-comb hyperspectral imaging setup. AOM: acousto-optic modulator; ATT: attenuator; C circulator; CTL: continuously tunable laser; EDFA: erbium-doped fiber amplifier; EOM: electro-optic modulator; HNLF: highly non-linear fiber; M: double balanced mixer; P: polariser; PD: photodetector; PG: pulse generator; PID: proportional integrativederivative servo controller; SG: signal generator.

an externally controllable repetition rate (maximum frequency 20 GHz). At the output of the EOM a train of pulses is generated, corresponding to a bandwidth of 0.1 nm. The output is sent to a L-band erbium-doped fiber amplifier in order to reach an output power of 100 mW. At this point, the two beams are sent in a counter-propagating manner inside a 2 km-long highly-nonlinear fiber, HNLF, (with a non-linear coefficient of 11.5 $W^{-1}km^{-1}$), in order to further increase the bandwidth, reaching 6 nm. Counter-propagation is needed in order to keep common the noises generated inside the fiber. After extracting the broadened light using a circulator, each frequency comb is sent to a 25 MHz acousto-optic modulator acting as a frequency shifter. After preliminary tests, it becomes clear that the major source of noise for this interferometric spectrometer was intensity noise generated in non-linear broadening. In order to reduce this contribution, the two AOM have been also used as a feedback control to the frequency combs power. The output of the AOM is split in two arms by a 10:90 coupler. The 10% of the radiation is sent to a photodetector that measures the output power. The generated signal is sent to a Proportional Integrative Derivative controller (PID) and the loop is closed to the amplitude of the sinusoidal wave that controls the AOM. Due to this, the radiation presents at least 25 dB decreased noise all over the acquisition band (0-10 kHz). Fig. 6.3 reports relative intensity noise measurements before and after control.

After this noise control stage, the two frequency combs are recombined and collimated within a 8 mm diameter, they interrogate two cells: one containing a gas of acetylene at a pressure of 146 Torr; a second one with a gas of ammonia at 133 Torr (with a double pass). The absorption cells are constituted by input and output angled windows, resulting in a trapezoidal lateral profile. In this way, the beams travels a longer distance in a part of the cell compare to another, simulating a spacial variation of the length of the absorption. The two cells are placed with different orientations, approximately a relative rotation of 180 degrees between them.

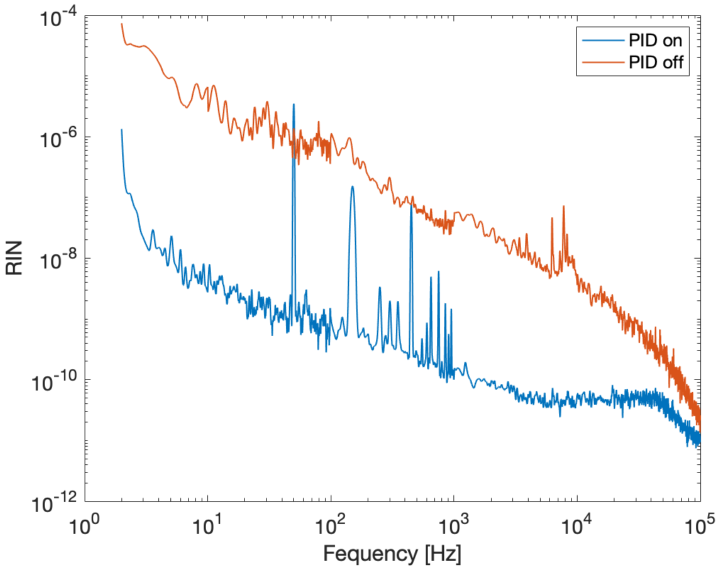

Figure 6.3: Relative intensity noise at the output of HNLF. Comparing between feedback control on (blue) and feedback control off (red).

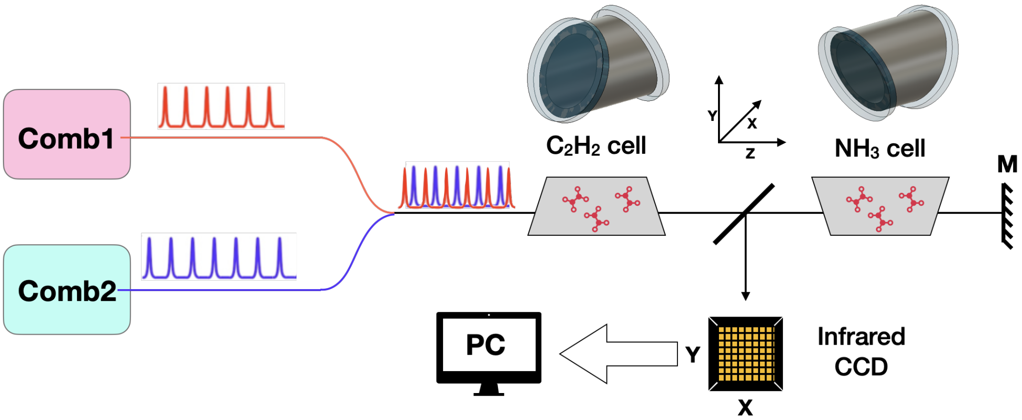

Figure 6.4: Dual-comb hyper-spectral imaging setup. The two frequency comb, comb1 and comb2 are combined are sent through two absorption cells containing ammonia, NH_3, and acetylene, C_2H_2. The transmission is recorded on a CCD camera. M: mirror, BS: beam splitter, PC: computer for acquisition.

The transmitted radiation is then focused onto a fast 14 bits infrared InGaAs CCD camera. The camera has a 60 MHz internal clock that synchronises the start of each frame integration. This model is equipped also with an external control clock signal input. It has been tested but it has resulted in a very high noise in the pixel readout. For this reason, it has been chosen its internal clock and to employ data-processing tools to correct for asynchronous detection. The camera can be set to acquire a different number of pixels. This number imposes an upper limit to the frame per second (FPS) that the camera is able to acquire. For example, at the maximum dimension 320x256, it is possible to acquire 330 FPS, at 32x32 12000 FPS or at 8x4 20000 FPS. For a first demonstration, targeted to achieve high spectral resolution, a 32x16 configuration has been chosen in order to allow acquisition at 10300 FPS. This parameter sets the limit for the ratio between frequency comb repetition rate and difference in repetition rate, according to Eq. 6.4, where f_{max} =FPS/2. For this experiment, it is chosen a repetition rate of 350 MHz. As a consequence, the difference in repetition frequency is 2 Hz and the relative offset is 2.5 kHz ($\approx$FPS/4).

The total power reaching the camera is 1 μW and the camera integration time is set to 80 μs.

6.3 Experimental results

Each pixel of the camera is recording a time trace similar to the one of Fig.6.5, this represents a series of interferograms. In particular, a series of seven burst (corresponding to 3.5 s) is used to compute a Fast Fourier Transform (FFT). This time window is chosen by taking in consideration the maximum coherence time of the system. Coherence time is experimentally determined by looking at the comb mode shape after Fourier transform. Fig. 6.6 shows the results for FFT time windows of 10.5 s and 21 s, respectively. In the second case, the FFT window is too long compared to the coherence time between the two frequency combs, resulting in a beatnote with a multiple peaks. For 10.5 s, instead, the beatnote can be still considered a single pick. The time window of 3.5 s has been chosen for the experiment to be well inside the coherence time.

In order to increase the SNR, it is possible to average several spectra. Before averaging, for each spectrum, the magnitude is calculated and the frequency axis is adjusted, in order to correct any possible shifts due to the asynchronous sampling. The result of 998.5 s of averaging is reported in Fig. 6.7.

Each comb mode is clearly resolved, and it is represented by a sinc-function with a width given by the inverse of a FFT window. It is possible to obtain the transmission spectrum by taking the peak value of each comb mode. After baseline removing, Fig. 6.8(b) is obtained. The result is then compared with a simulation of acetylene and ammonia transmittance (Fig. 6.8(a)). A very good agreement is found for acetylene while a poorer result is obtained from ammonia, due to low precision of parameter reported in HITRAN database. A closer look to a couple of ammonia and acetylene lines (Fig. 6.9) makes more clear the previous statement.

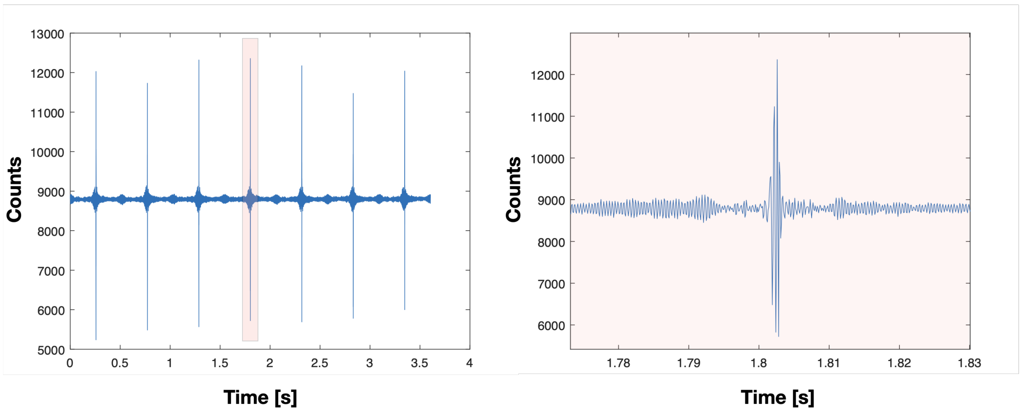

Figure 6.5: Left: seven interferogram bursts recorded as a function of time on the pixel 16x8. Right: detail of a single burst of the sequence (highlighted area in the right plot).

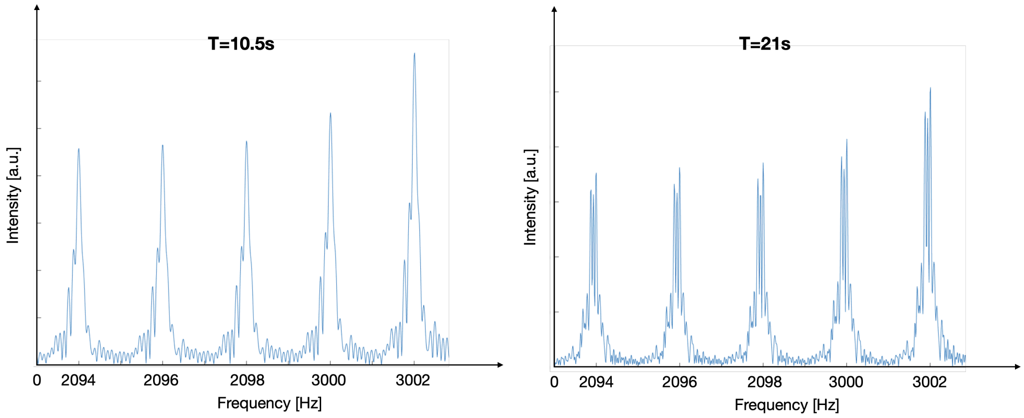

Figure 6.6: Frequency comb amplitude spectra with two different Fourier transform windows. Left: 10.5 seconds. Right: 21 seconds.

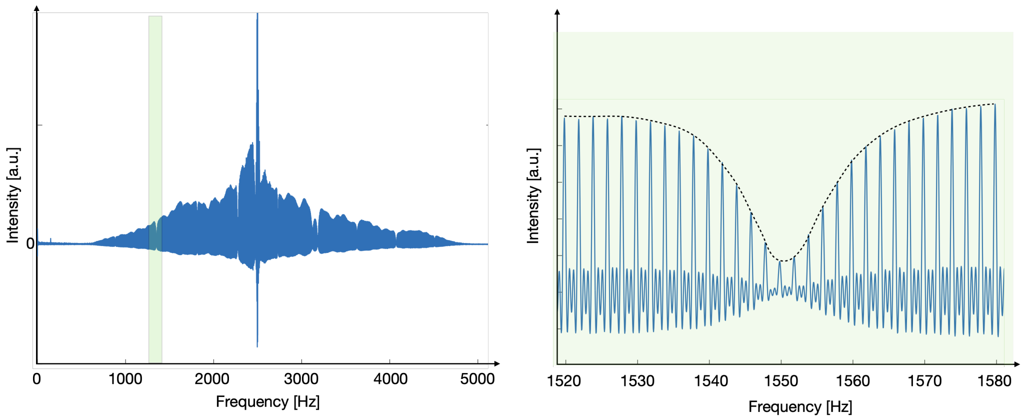

Figure 6.7: Left: averaged dual-comb spectrum (1000s). Right: spectrum detail around 1550 Hz (green highlighted rectangle); the envelope of an absorption feature of acetylene is indicated by the dash black curve.

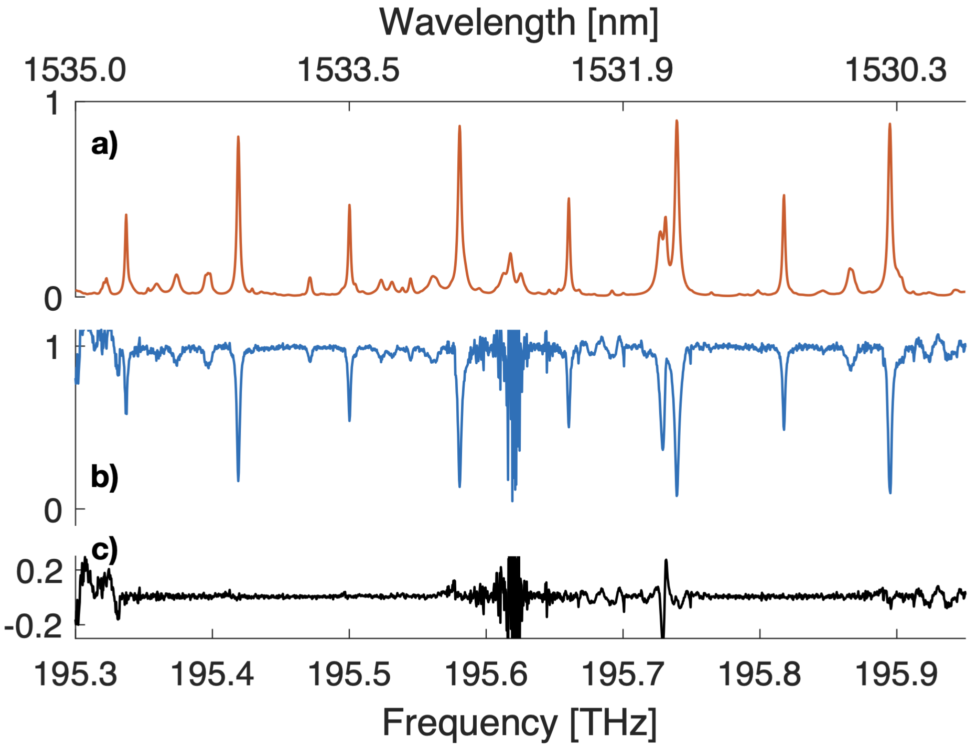

Figure 6.8: a) HITRAN simulation for acetylene at p = 146 Torr and L = 3.5 cm and ammonia at p =133 Torr and L = 9 cm. b) Dual-comb transmittance spectrum. c) Residuals plot.

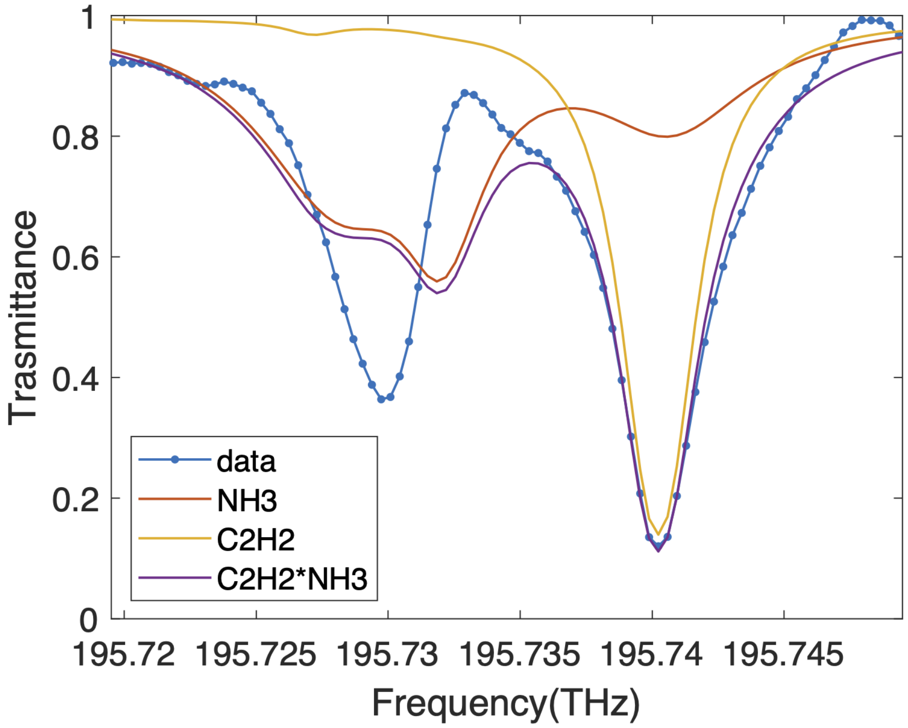

Figure 6.9: Transmittance spectrum recorded with dual-comb spectroscopy in comparison best fit obtained with HITRAN parameter. Blue curve: experimental data. Yellow: best fit of acetylene. Red: best fit for ammonia. Purple: transmittance product of ammonia and acetylene.

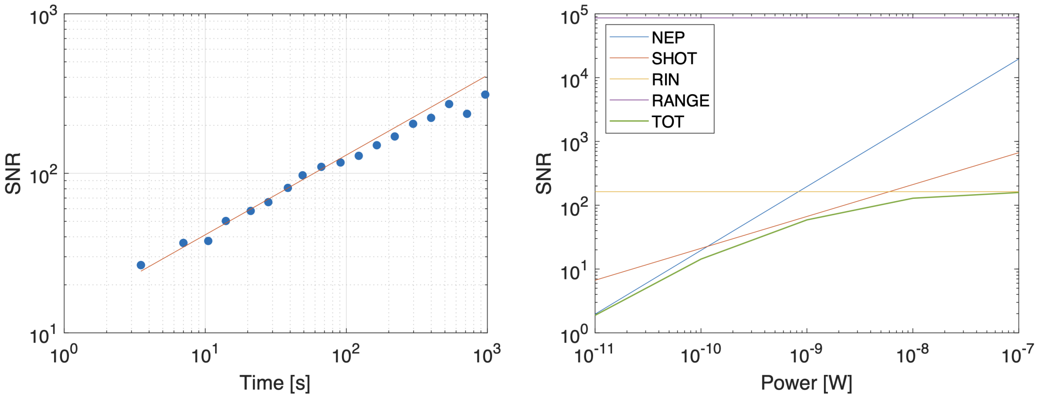

Figure 6.10: a) Dual-comb spectroscopy signal to noise ratio as a function of the averaging time. b) Signal to noise ratio estimated [114] with an averaging time of 100 s by several contributions as a function of the power. RIN: laser relative intensity noise; SHOT: shot noise; NEP: detector noise equivalent power; RANGE: quantisation noise; TOT: total contribution.

As a final result, signal to noise ratio, SNR, is evaluated as a function of the measurement time (Fig. 6.10). SNR is calculated starting from a fitting of acetylene line at 195.41 THz. This line is isolated and far from ammonia strong absorptions. The fitting model is a Voigt profile plus a 5-th degree polynomial baseline. The residual of this fit should approximate well the signal to noise ratio of the system.

A square root dependence of SNR with respect to averaging time can be retrieved up to 100 s, and up to 1000 s the deviation is less than a factor of 2. In addition, different contributions to the signal to noise ratio have been analysed. Fig. 6.10(b) reports effects of noise equivalent power (NEP), shot noise (SHOT), laser intensity noise (RIN) and quantisation noise (RANGE) for different single pixel power level at 100s of averaging time. In this experiment, the power is between 1 and 10 nW per pixel. The measurements are shot-noise limited.

Until now, only single pixel results have been presented. Of course, each pixel is recording an interferogram and, in consequence, a spectrum. The only difference is the power of light impinging on each pixel, according to the map of Fig. 6.11.

Once the spectrum is obtained for each pixel, it is possible to perform a fit as a function of the gas path length. The result is plotted in Fig. 6.12 and Fig. 6.13. Each map is then fitted with a plane in order to retrieve the angle of each cell.

As expected, the precision obtained for acetylene is higher compared to ammonia. This can be explained by taking in consideration the presence of different strong absorptions of acetylene within the frequency range of the experiment, and by considering the poor quality of parameters for ammonia, especially regarding pressure broadening and pressure shifts. However for both absorption cells, their angle have been retrieved, respectively 190 degrees for the acetylene cell and 8 degrees for the ammonia cell (in the y-x plane). The cell length average precision is 0.02 cm for the acetylene and 0.2 cm for the ammonia. This value are calculated as the average standard deviation of the length calculated at each pixel.

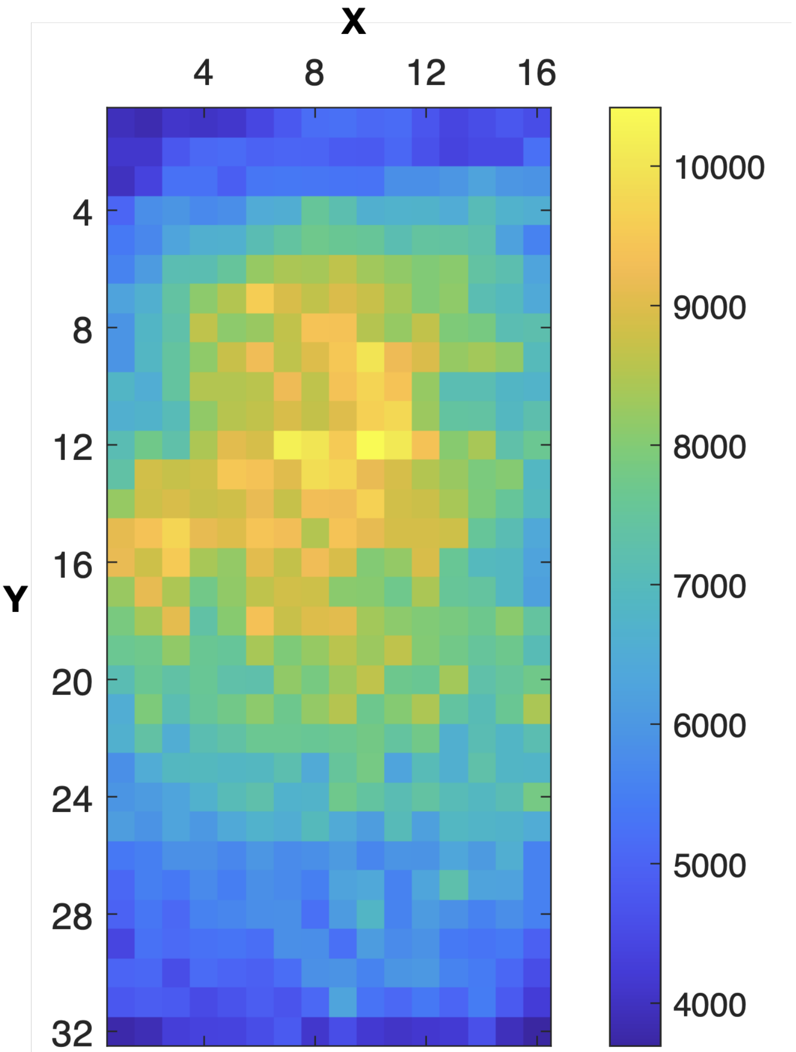

Figure 6.11: Intensity recorded on 32x16 pixels. Intensity is measured in counts between 0 a 2^{14}.

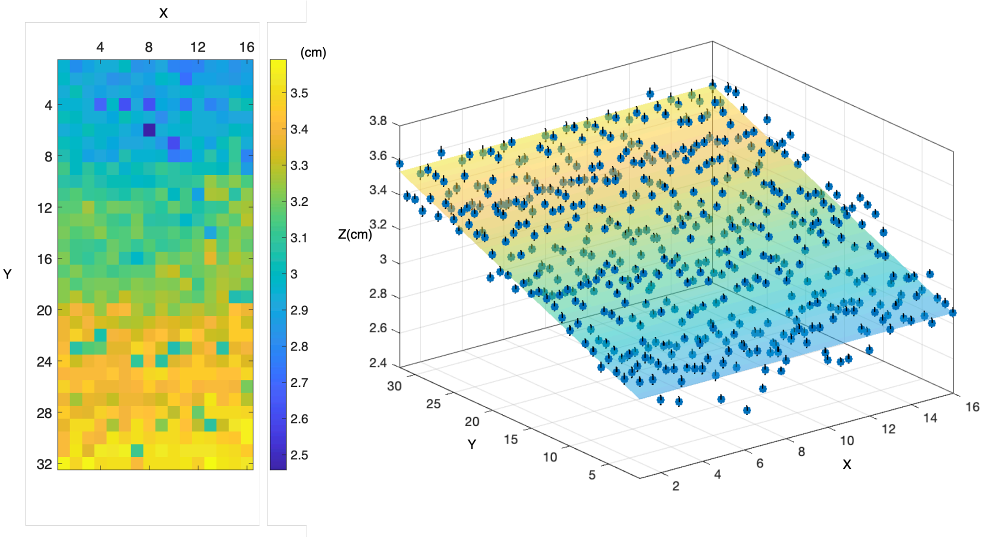

Figure 6.12: a)Acetylene cell length map retrieved by fitting the absorption profile as a function of pixel position (X, Y). Fitted length is expressed by the colour bar. b) Points and errorrbars represent the reconstructed lengths with their fitting uncertainties. The plane is the best fit of these experimental points.

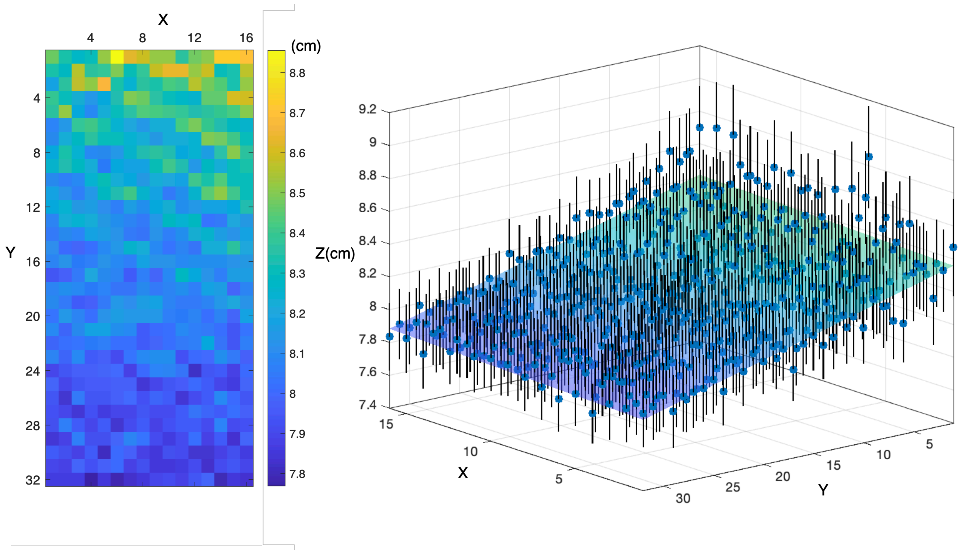

Figure 6.13: a)Ammonia cell length map retrieved by fitting the absorption profile as a function of pixel position (X, Y). Fitted length is expressed by the colour bar. b) Points and errorrbars represent the reconstructed lengths with their fitting uncertainties. The plane is the best fit of these experimental points.

Conclusions and perspectives

The work in this doctoral thesis has focused in high-precision and broadband frequency-comb-spectroscopy in near- and mid-infrared spectral regions. Both comb-assisted and direct-comb approaches have been analysed.

A high-resolution comb-assisted QCL spectrometer has been developed to investigate the crowded absorption spectrum of CHF_3 molecule at around its fundamental ν_2 and ν_5 vibrational band at 8.6 μm. Sub-Doppler line absorption profiles and line centre frequencies have been recorded with high fidelity and high precision as a function of gas pressure and QCL power. Combining phase-locking methods of the QCL to the optical frequency comb and high sensitivity modulation spectroscopy techniques, CHF_3 spectroscopic parameters have been recorded with high signal to noise ratio. Thanks to this, line centre frequencies of 95 transitions have been measured with fractional precision of $2{\cdot}10^{-11}$ (corresponding to an absolute frequency accuracy of 400 Hz). In addition, exploiting the narrow features of the sub-Doppler absorption lines of CHF_3 as absolute frequency references, a molecular frequency standard at 8.6 μm has been realised. This mid-infrared reference has been fully characterised in terms of stability and accuracy using two different locking strategies, the frequency modulation and the modulation transfer methods. The former demonstrated fractional precision of $8\ {\cdot}10^{-12}$ and an accuracy of $3{\cdot}10^{-10}$. The latter showed a long-term stability and accuracy of $4\ {\cdot}10^{-12}$ and $3{\cdot}10^{-10}$, respectively. Results are very similar for long term stability (longer than 1 s), but modulation transfer showed almost 2 orders of magnitude better stability at short times. Smaller pressure, narrower transit time broadening and lower temperatures can all lead to a further decrease of the molecular linewidth and, as a consequence, to a better mid-infrared frequency standard. For this purpose, high-resolution spectroscopy of cold CHF_3 molecules (at a temperature around 4 K by buffer cooling method) is the natural evolution of this methodology having as a final aim the determination of the proton-electron mass ratio.

Two different direct-comb spectroscopy methods able to resolve the single comb mode have been investigated in the near-infrared spectral region at around 1.5 μm. The novel SMART (Scanning Micro-cAvity ResonaTor) spectroscopy method has demonstrated a high spectral resolution with negligible instrumental line shape contribution, which is ultimately limited by the linewidth of the frequency comb adopted for the experiment. A narrow linewidth Fabry-Pérot cavity (400 kHz) has been used for this demonstration, obtaining an uncertainty of 20-40 kHz in the reconstructed profile. In addition, broadband absolute frequency calibration has been also demonstrated by measuring the $\nu_1 + \nu_3$ ro-vibrational spectrum of the acetylene molecule at around 1.55 μm. An absolute calibration has been obtained over 4 THz optical bandwidth. This direct-comb method allows performances equivalent to other direct-comb techniques but it is based on a simpler and more flexible architecture, able to be easily extended to the mid-IR spectral region.

Finally, a dual-comb spectroscopy approach has been applied to high-spectral resolution imaging of gas samples. Spectroscopy of gases of ammonia and acetylene around 1530 nm have been recorded with 350 MHz resolution over a 0.6 THz. An hyperspectral cube as large as 877710 (32x16x1714) allowed to reconstruct the spatial distribution of C_2H_2 and NH_3 absorptions in a proof-of-concept experiment. High speed camera's technology is still a limiting factor for dual-comb hypespectral imaging. With the development of faster cameras, it is possible to increase spectral bandwidth, spectral resolution, number of pixels and spatial resolution in shorter acquisition times,obtaining a hypespectral analysis tool with unprecedented performances that finds interesting applications in real time environmental and combustion process gas sensing.

Peer reviewed publications

- A. Gambetta, E. Vicentini, Y. Wang, N. Coluccelli, T. T. Fernandez, E. Fasci, A. Castrillo, L. Gianfrani, L. Santamaria, V. Di Sarno, P. Maddaloni, P. Laporta and G. Galzerano. *Metrology-grade sub-Doppler spectroscopy of CHF3 at 8.6* μm. 2017 Conference on Lasers and Electro-Optics Europe and European Quantum Electronics Conference (CLEO/Europe-EQEC) (2017): 1-1.

- A. Gambetta, E. Vicentini, Y. Wang, N. Coluccelli, E. Fasci, Livio Gianfrani, A. Castrillo, V. Di Sarno, L. Santamaria, P. Maddaloni, P. De Natale, P. Laporta and G. Galzerano. *Absolute frequency measurements of* CHF_3 *Doppler-free rovibrational transitions at* $8.6\mu m$. Optics letters 42 10 (2017): 1911-1914.

- A. Gambetta, E. Vicentini, N. Coluccelli, Y. Wang, T. T. Fernandez, P. Maddaloni, P. De Natale, A. Castrillo, L. Gianfrani, P. Laporta, and G. Galzerano. *Versatile mid-infrared frequency-comb referenced sub-Doppler spectrometer.* APL Photonics, 3(4), 046103, (2018).

- A. Gambetta, E. Vicentini, Y. Wang, N. Coluccelli, P. Laporta and G. Galzerano. *High-resolution and ultra-broadband direct-comb absolute-spectroscopy by means of the scanning micro-cavity resonator (SMART) technique.* 73rd International Symposium on Molecular Spectroscopy (June 2018): WA08.

- N. Coluccelli, E. Vicentini, A. Gambetta, C. R Howle, K. Mcewan, P. Laporta, and G. Galzerano. *Broadband Fourier-transform coherent Raman spectroscopy with an ytterbium fiber laser.* Optics Express Vol. 26, Issue 15, pp. 18855-18862 (2018).

- E. Vicentini, A. Gambetta, N. Coluccelli, E. Fasci, A. Castrillo, L. Gianfrani, V. Di Sarno, P. Maddaloni, A. Ceausu-Velcescu, P. De Natale, Y. Wang, T. T. Fernandez, P. Laporta, G. Galzerano, *Rovibrational fine structure and transition dipole moment of* CHF_3 *by frequency-comb-assisted saturated spectroscopy at* $8.6\mu m$. Journal of Quantitative Spectroscopy and Radiative Transfer, Volume 217, 2018, Pages 373-379.

- N. Coluccelli, A. Gambetta, E. Vicentini, P. Laporta, K. McEwan, and C. R. Howle (2019, May). *Fiber-lasers for coherent Raman detection of toxic chemical hazards.* In Chemical, Biological, Radiological, Nuclear, and Explosives (CBRNE) Sensing XX (Vol. 11010, p. 1101015). International Society for Optics and Photonics.

- Y. Wang, S. O. Leonov, V. S. Shiryaev, G. E. Snopatin, B. S. Stepanov, V. G. Plotnichenko, V. E. Karasik, E. Vicentini, A. Gambetta, N. Coluccelli, C. Svelto, P. Laporta, and G. Galzerano *Octave-spanning high-repetition-rate mid-IR supercontinuum for frequency comb synthesis* in 2019 Conference on Lasers and Electro-Optics Europe and European Quantum Electronics Conference, OSA Technical Digest (Optical Society of America, 2019), paper cf_p_19.

- E. Vicentini, Y. Wang, D. Gatti, A. Gambetta, P. Laporta, G. Galzerano, K. Curtis, K. McEwan, C. R. Howle, and N. Coluccelli, *Nonlinear pulse compression to 22 fs at 15.6 μJ by an all-solid-state multipass approach* Opt. Express 28, 4541-4549 (2020).

- S. O. Leonov, Y. Wang, V. S. Shiryaev, G. E. Snopatin, B. S. Stepanov, V. G. Plotnichenko, E. Vicentini, A. Gambetta, N. Coluccelli, C. Svelto, P. Laporta, and G. Galzerano, *Coherent mid-infrared supercontinuum generation in tapered suspended-core $As_{39}Se_{61}$ fibers pumped by a few-optical-cycle Cr:ZnSe laser* Opt. Lett. 45, 1346-1349 (2020).

- E. Vicentini, P. Maddaloni, R. Aiello, A. Gambetta, N. Coluccelli, L. M. Molteni, A. Castrillo, L. Gianfrani, P. De Natale, P. Laporta, G. Galzerano. *Absolute frequency metrology of the CHF_3 8.6μm ro-vibrational spectrum at 10^{-11} level.* Journal of Quantitative Spectroscopy and Radiative Transfer, 106963 (2020).

- Z. Chen, K. Van Gasse, E. Vicentini, J. Huh, S. Poelman, Z. Wang, G. Roelkens, T. W. Hänsch, B. Kuyken, and N. Picqué *High-resolution dual-comb gas-phase spectroscopy with a mode-locked laser on a photonic chip* in Conference on Lasers and Electro-Optics, OSA Technical Digest (Optical Society of America, 2020), paper JTh4A.8.

- G. Galzerano, E. Suerra, D. Giannotti, F. Canella, E. Vicentini and S. Cialdi, *Accurate Measurement of Optical Resonator Finesse*, in IEEE Transactions on Instrumentation and Measurement, vol. 69, no. 11, pp. 9119-9123, Nov. 2020.

- K. Van Gasse, Z. Chen, E. Vicentini, J. Yun Huh, S. Poelman, Z. Wang, G. Roelkens, T. W. Hänsch, B. Kuyken, N. Picqué *An on-chip III-V-semiconductor-on-silicon laser frequency comb for gas-phase molecular spectroscopy in real-time*, in arXiv.

- E. Vicentini, A. Gambetta, N. Coluccelli, V. Di Sarno, P. Maddaloni, P. De Natale, A. Castrillo, L. Gianfrani, P. Laporta, and G. Galzerano, *Absolute frequency stabilization of a QCL at 8.6μm by modulation transfer spectroscopy,* Opt. Lett. 45, 4948-4951 (2020)

- E. Vicentini, Z. Chen, J. H. Huh, G. Galzerano, T. W. Hänsch, and N. Picqué, *High-Spectral-Resolution Imaging Spectroscopy with a Dual-Comb Interferometer,* in Frontiers in Optics / Laser Science, B. Lee, C. Mazzali, K. Corwin, and R. Jason Jones, eds., OSA Technical Digest (Optical Society of America, 2020), paper LTu2F.3.

- Z. Wang, Z. Chen, X. Chao, E. Vicentini, T. W. Hänsch, and N. Picqué, *Precise Mid-Infrared Dual-Comb Spectroscopy of Ethylene,* in Frontiers in Optics / Laser Science, B. Lee, C. Mazzali, K. Corwin, and R. Jason Jones, eds., OSA Technical Digest (Optical Society of America, 2020), paper FW7B.3.

- J. H. Huh, Z. Chen, E. Vicentini, T. W. Hänsch, and N. Picqué, *Dual-Comb Spectroscopy based on Single Electro-Optic Modulation,* in Frontiers in Optics / Laser Science, B. Lee, C. Mazzali, K. Corwin, and R. Jason Jones, eds., OSA Technical Digest (Optical Society of America, 2020), paper LM5F.3.

- E. Vicentini, A. Gambetta, N. Coluccelli, Y. Wang, P. Laporta and G. Galzerano,(2020). *Direct-frequency-comb spectroscopy by a scanning Fabry-Pérot microcavity resonator.* Physical Review A, 102(3), 033510.

- E. Vicentini, A. Gambetta, G. Galzerano, P. Laporta, K. Curtis, K. McEwan, C. R. Howle, and N. Coluccelli, *Fiber laser system for standoff coherent Raman spectroscopy,* Opt. Lett. 45, 5925-5928 (2020)

Bibliography

[1] John L Hall. Nobel lecture: Defining and measuring optical frequencies. *Reviews of Modern Physics*, 78(4):1279, 2006.

[2] Theodor W Hänsch. Nobel lecture: passion for precision. *Reviews of Modern Physics*, 78(4):1297, 2006.

[3] Nathalie Picqué and Theodor W Hänsch. Frequency comb spectroscopy. *Nature Photonics*, 13(3):146–157, 2019.

[4] Luigi Consolino, Francesco Cappelli, Mario Siciliani de Cumis, and Paolo De Natale. Qcl-based frequency metrology from the mid-infrared to the thz range: a review. *Nanophotonics*, 8(2):181–204, 2018.

[5] L Santamaria, V Di Sarno, I Ricciardi, S Mosca, M De Rosa, Gabriele Santambrogio, P Maddaloni, and P De Natale. Assessing the time constancy of the proton-to-electron mass ratio by precision ro-vibrational spectroscopy of a cold molecular beam. *Journal of Molecular Spectroscopy*, 300:116–123, 2014.

[6] Edoardo Vicentini, Pasquale Maddaloni, Roberto Aiello, Alessio Gambetta, Nicola Coluccelli, Lisa M Molteni, Antonio Castrillo, Livio Gianfrani, Paolo De Natale, Paolo Laporta, et al. Absolute frequency metrology of the chf3 8.6-μm ro-vibrational spectrum at 10- 11 level. *Journal of Quantitative Spectroscopy and Radiative Transfer*, page 106963, 2020.

[7] Edoardo Vicentini, Alessio Gambetta, Nicola Coluccelli, Valentina Di Sarno, Pasquale Maddaloni, Paolo De Natale, Antonio Castrillo, Livio Gianfrani, Paolo Laporta, and Gianluca Galzerano. Absolute frequency stabilization of a qcl at 8.6 μm by modulation transfer spectroscopy. *Optics Letters*, 45(17): 4948–4951, 2020.

[8] Alessio Gambetta, Marco Cassinerio, Davide Gatti, Paolo Laporta, and Gianluca Galzerano. Scanning micro-resonator direct-comb absolute spectroscopy. *Scientific reports*, 6:35541, 2016.

[9] Edoardo Vicentini, Alessio Gambetta, Nicola Coluccelli, Yuchen Wang, Paolo Laporta, and Gianluca Galzerano. Direct-frequency-comb spectroscopy by a scanning fabry-pérot microcavity resonator. *Physical Review A*, 102(3):033510, 2020.

[10] Orazio Svelto and David C Hanna. *Principles of lasers*, volume 1. Springer, 2010.

[11] Wolfgang Demtröder. *Laser spectroscopy: basic concepts and instrumentation.* Springer Science & Business Media, 2013.

[12] Horace P. Yuen and Vincent W. S. Chan. Noise in homodyne and heterodyne detection. *Opt. Lett.*, 8(3):177–179, Mar 1983. doi: 10.1364/OL.8.000177. URL `http://ol.osa.org/abstract.cfm?URI=ol-8-3-177`.

[13] James M Supplee, Edward A Whittaker, and Wilfried Lenth. Theoretical description of frequency modulation and wavelength modulation spectroscopy. *Applied Optics*, 33(27):6294–6302, 1994.

[14] Gary C Bjorklund. Frequency-modulation spectroscopy: a new method for measuring weak absorptions and dispersions. *Optics letters*, 5(1):15–17, 1980.

[15] LO Hocker, A Javan, D Ramachandra Rao, L Frenkel, and T Sullivan. Absolute frequency measurement and spectroscopy of gas laser transitions in the far infrared. *Applied Physics Letters*, 10(5):147–149, 1967.

[16] H Schnatz, B Lipphardt, J Helmcke, F Riehle, and G Zinner. First phase-coherent frequency measurement of visible radiation. *Physical Review Letters*, 76(1):18, 1996.

[17] James N Eckstein, AI Ferguson, and TW Hänsch. High-resolution two-photon spectroscopy with picosecond light pulses. *Physical Review Letters*, 40(13): 847, 1978.

[18] Jun Ye. *Femtosecond optical frequency comb: principle, operation and applications.* Springer Science & Business Media, 2005.

[19] John L. Hall. Nobel lecture: Defining and measuring optical frequencies. *Rev. Mod. Phys.*, 78:1279–1295, Nov 2006. doi: 10.1103/RevModPhys.78.1279. URL `https://link.aps.org/doi/10.1103/RevModPhys.78.1279`.

[20] Davide Gatti, Tommaso Sala, Marco Marangoni, Gianluca Galzerano, and Livio Gianfrani. Precision molecular spectroscopy with frequency combs. *Encyclopedia of Analytical Chemistry*, 2012.

[21] David J Jones, Scott A Diddams, Jinendra K Ranka, Andrew Stentz, Robert S Windeler, John L Hall, and Steven T Cundiff. Carrier-envelope phase control of femtosecond mode-locked lasers and direct optical frequency synthesis. *Science*, 288(5466):635–639, 2000.

[22] J Reichert, R Holzwarth, Th Udem, and T W_ Haensch. Measuring the frequency of light with mode-locked lasers. *Optics communications*, 172(1-6): 59–68, 1999.

[23] Harald R Telle, G Steinmeyer, Amy E Dunlop, Joern Stenger, Dirk H Sutter, and Ursula Keller. Carrier-envelope offset phase control: A novel concept for absolute optical frequency measurement and ultrashort pulse generation. *Applied Physics B*, 69(4):327–332, 1999.

[24] Scott A Diddams, David J Jones, Jun Ye, Steven T Cundiff, John L Hall, Jinendra K Ranka, Robert S Windeler, Ronald Holzwarth, Thomas Udem, and Theodor W Hänsch. Direct link between microwave and optical frequencies with a 300 thz femtosecond laser comb. *Physical review letters*, 84(22):5102, 2000.

[25] Tobias J Kippenberg, Alexander L Gaeta, Michal Lipson, and Michael L Gorodetsky. Dissipative kerr solitons in optical microresonators. *Science*, 361(6402), 2018.

[26] Alexander L Gaeta, Michal Lipson, and Tobias J Kippenberg. Photonic-chip-based frequency combs. *Nature Photonics*, 13(3):158–169, 2019.

[27] Zhechao Wang, Kasper Van Gasse, Valentina Moskalenko, Sylwester Latkowski, Erwin Bente, Bart Kuyken, and Gunther Roelkens. A iii-v-on-si ultra-dense comb laser. *Light: Science & Applications*, 6(5):e16260–e16260, 2017.

[28] David A Long, Adam J Fleisher, Kevin O Douglass, Stephen E Maxwell, K Bielska, Joseph T Hodges, and David F Plusquellic. Multiheterodyne spectroscopy with optical frequency combs generated from a continuous-wave laser. *Optics letters*, 39(9):2688–2690, 2014.

[29] Guy Millot, Stéphane Pitois, Ming Yan, Tatevik Hovhannisyan, Abdelkrim Bendahmane, Theodor W Hänsch, and Nathalie Picqué. Frequency-agile dual-comb spectroscopy. *Nature Photonics*, 10(1):27–30, 2016.

[30] Albert Schliesser, Nathalie Picqué, and Theodor W Hänsch. Mid-infrared frequency combs. *Nature photonics*, 6(7):440–449, 2012.

[31] Birgitta Bernhardt, Evgeni Sorokin, Patrick Jacquet, Raphaël Thon, Thomas Becker, Irina T Sorokina, Nathalie Picqué, and Theodor W Hänsch. Mid-infrared dual-comb spectroscopy with 2.4 μm cr 2+: Znse femtosecond lasers. *Applied Physics B*, 100(1):3–8, 2010.

[32] Sergey Vasilyev, Viktor Smolski, Jeremy Peppers, Igor Moskalev, Mike Mirov, Yury Barnakov, Sergey Mirov, and Valentin Gapontsev. Middle-ir frequency comb based on cr: Zns laser. *Optics Express*, 27(24):35079–35087, 2019.

[33] Simon Duval, Martin Bernier, Vincent Fortin, Jérôme Genest, Michel Piché, and Réal Vallée. Femtosecond fiber lasers reach the mid-infrared. *Optica*, 2 (7):623–626, 2015.

[34] Sergei Antipov, Darren D Hudson, Alexander Fuerbach, and Stuart D Jackson. High-power mid-infrared femtosecond fiber laser in the water vapor transmission window. *Optica*, 3(12):1373–1376, 2016.

[35] Cornelia Fischer and Markus Sigrist. Mid-ir difference frequency generation. *Solid-state mid-infrared laser sources*, pages 99–143, 2003.

[36] P Maddaloni, P Malara, G Gagliardi, and P De Natale. Mid-infrared fibre-based optical comb. *New Journal of Physics*, 8(11):262, 2006.

[37] Seth M Foreman, Adela Marian, Jun Ye, Evgeny A Petrukhin, Mikhail A Gubin, Oliver D Mücke, Franco NC Wong, Erich P Ippen, and Franz X Kärtner. Demonstration of a hene/ch 4-based optical molecular clock. *Optics Letters*, 30(5):570–572, 2005.

[38] Christian Erny, K Moutzouris, Jens Biegert, Dietrich Kühlke, Florian Adler, Alfred Leitenstorfer, and Ursula Keller. Mid-infrared difference-frequency generation of ultrashort pulses tunable between 3.2 and 4.8 μm from a compact fiber source. *Optics letters*, 32(9):1138–1140, 2007.

[39] Fritz Keilmann, Christoph Gohle, and Ronald Holzwarth. Time-domain mid-infrared frequency-comb spectrometer. *Optics letters*, 29(13):1542–1544, 2004.

[40] Fritz Keilmann and Sergiu Amarie. Mid-infrared frequency comb spanning an octave based on an er fiber laser and difference-frequency generation. *Journal of Infrared, Millimeter, and Terahertz Waves*, 33(5):479–484, 2012.

[41] Peter G Schunemann, Kevin T Zawilski, Leonard A Pomeranz, Daniel J Creeden, and Peter A Budni. Advances in nonlinear optical crystals for mid-infrared coherent sources. *JOSA B*, 33(11):D36–D43, 2016.

[42] DT Reid, BJS Gale, and J Sun. Frequency comb generation and carrier-envelope phase control in femtosecond optical parametric oscillators. *Laser physics*, 18(2):87–103, 2008.

[43] Nick Leindecker, Alireza Marandi, Robert L Byer, and Konstantin L Vodopyanov. Broadband degenerate opo for mid-infrared frequency comb generation. *Optics express*, 19(7):6296–6302, 2011.

[44] Andreas Hugi, Gustavo Villares, Stéphane Blaser, HC Liu, and Jérôme Faist. Mid-infrared frequency comb based on a quantum cascade laser. *Nature*, 492 (7428):229–233, 2012.

[45] Jonas Westberg, Lukasz A Sterczewski, Filippos Kapsalidis, Yves Bidaux, Johanna M Wolf, Mattias Beck, Jérôme Faist, and Gerard Wysocki. Dual-comb spectroscopy using plasmon-enhanced-waveguide dispersion-compensated quantum cascade lasers. *Optics letters*, 43(18):4522–4525, 2018.

[46] Takeshi Yasui, Yasuhiro Kabetani, Eisuke Saneyoshi, Shuko Yokoyama, and Tsutomu Araki. Terahertz frequency comb by multifrequency-heterodyning photoconductive detection for high-accuracy, high-resolution terahertz spectroscopy. *Applied Physics Letters*, 88(24):241104, 2006.

[47] L Consolino, A Taschin, P Bartolini, S Bartalini, P Cancio, ALESSANDRO Tredicucci, HE Beere, DA Ritchie, R Torre, MS Vitiello, et al. Phase-locking to a free-space terahertz comb for metrological-grade terahertz lasers. *Nature Communications*, 3(1):1–5, 2012.

[48] Nezih T Yardimci, Shang-Hua Yang, Christopher W Berry, and Mona Jarrahi. High-power terahertz generation using large-area plasmonic photoconductive emitters. *IEEE Transactions on Terahertz Science and Technology*, 5(2):223–229, 2015.

[49] David Burghoff, Tsung-Yu Kao, Ningren Han, Chun Wang Ivan Chan, Xiaowei Cai, Yang Yang, Darren J Hayton, Jian-Rong Gao, John L Reno, and Qing Hu. Terahertz laser frequency combs. *Nature Photonics*, 8(6):462–467, 2014.

[50] Christoph Gohle, Thomas Udem, Maximilian Herrmann, Jens Rauschenberger, Ronald Holzwarth, Hans A Schuessler, Ferenc Krausz, and Theodor W Hänsch. A frequency comb in the extreme ultraviolet. *Nature*, 436(7048):234–237, 2005.

[51] Arman Cingöz, Dylan C Yost, Thomas K Allison, Axel Ruehl, Martin E Fermann, Ingmar Hartl, and Jun Ye. Direct frequency comb spectroscopy in the extreme ultraviolet. *Nature*, 482(7383):68–71, 2012.

[52] Scott A Diddams, Kerry Vahala, and Thomas Udem. Optical frequency combs: Coherently uniting the electromagnetic spectrum. *Science*, 369(6501), 2020.

[53] Pasquale Maddaloni, Marco Bellini, and Paolo De Natale. *Laser-based measurements for time and frequency domain applications: a handbook*. CRC Press, 2013.

[54] Harald R Telle, Burghard Lipphardt, and Jörn Stenger. Kerr-lens, mode-locked lasers as transfer oscillators for optical frequency measurements. *Applied Physics B*, 74(1):1–6, 2002.

[55] Christian G Parthey, Arthur Matveev, Janis Alnis, Birgitta Bernhardt, Axel Beyer, Ronald Holzwarth, Aliaksei Maistrou, Randolf Pohl, Katharina Predehl, Thomas Udem, et al. Improved measurement of the hydrogen 1 s–2 s transition frequency. *Physical review letters*, 107(20):203001, 2011.

[56] Anne Amy-Klein, Andrei Goncharov, Christophe Daussy, Christophe Grain, Olivier Lopez, Georgio Santarelli, and Christian Chardonnet. Absolute frequency measurement in the 28-thz spectral region with a femtosecond laser comb and a long-distance optical link to a primary standard. *Applied Physics B*, 78(1):25–30, 2004.

[57] Adela Marian, Matthew C Stowe, John R Lawall, Daniel Felinto, and Jun Ye. United time-frequency spectroscopy for dynamics and global structure. *science*, 306(5704):2063–2068, 2004.

[58] P Domachuk, NA Wolchover, M Cronin-Golomb, A Wang, Alan K George, CMB Cordeiro, Jonathan C Knight, and FG Omenetto. Over 4000 nm bandwidth of mid-ir supercontinuum generation in sub-centimeter segments of highly nonlinear tellurite pcfs. *Optics Express*, 16(10):7161–7168, 2008.

[59] Christoph Gohle, Björn Stein, Albert Schliesser, Thomas Udem, and Theodor W Hänsch. Frequency comb vernier spectroscopy for broadband, high-resolution, high-sensitivity absorption and dispersion spectra. *Physical review letters*, 99(26):263902, 2007.

[60] Peter R Griffiths and James A De Haseth. *Fourier transform infrared spectrometry*, volume 171. John Wiley & Sons, 2007.

[61] Julien Mandon, Guy Guelachvili, and Nathalie Picqué. Fourier transform spectroscopy with a laser frequency comb. *Nature Photonics*, 3(2):99–102, 2009.

[62] Seok-Jeong Lee, Bambang Widiyatmoko, Motonobu Kourogi, and Motoichi Ohtsu. Ultrahigh scanning speed optical coherence tomography using optical frequency comb generators. *Japanese Journal of Applied Physics*, 40(8B): L878, 2001.

[63] Alexander M Zolot, Fabrizio R Giorgetta, Esther Baumann, Jeffrey W Nicholson, William C Swann, I Coddington, and Nathan R Newbury. Direct-comb molecular spectroscopy with accurate, resolved comb teeth over 43 thz. *Optics letters*, 37(4):638–640, 2012.

[64] Zaijun Chen, Ming Yan, Theodor W Hänsch, and Nathalie Picqué. A phase-stable dual-comb interferometer. *Nature communications*, 9(1):1–7, 2018.

[65] Takuro Ideguchi, Antonin Poisson, Guy Guelachvili, Nathalie Picqué, and Theodor W Hänsch. Adaptive real-time dual-comb spectroscopy. *Nature communications*, 5(1):1–8, 2014.

[66] Julien Roy, Jean-Daniel Deschênes, Simon Potvin, and Jérôme Genest. Continuous real-time correction and averaging for frequency comb interferometry. *Optics express*, 20(20):21932–21939, 2012.

[67] Xin Zhao, Guoqing Hu, Bofeng Zhao, Cui Li, Yingling Pan, Ya Liu, Takeshi Yasui, and Zheng Zheng. Picometer-resolution dual-comb spectroscopy with a free-running fiber laser. *Optics Express*, 24(19):21833–21845, 2016.

[68] Soroush Mehravar, Robert A Norwood, N Peyghambarian, and K Kieu. Real-time dual-comb spectroscopy with a free-running bidirectionally mode-locked fiber laser. *Applied Physics Letters*, 108(23):231104, 2016.

[69] Qi-Fan Yang, Xu Yi, Ki Youl Yang, and Kerry Vahala. Counter-propagating solitons in microresonators. *Nature Photonics*, 11(9):560, 2017.

[70] Ming Yan, Pei-Ling Luo, Kana Iwakuni, Guy Millot, Theodor W Hänsch, and Nathalie Picqué. Mid-infrared dual-comb spectroscopy with electro-optic modulators. *Light: Science & Applications*, 6(10):e17076–e17076, 2017.

[71] Hans-Rolf Dübal and Martin Quack. Tridiagonal fermi resonance structure in the ir spectrum of the excited ch chromophore in cf3h. *The Journal of chemical physics*, 81(9):3779–3791, 1984.

[72] Sieghard Albert, Sigurd Bauerecker, Elena S Bekhtereva, Irina B Bolotova, H Hollenstein, Martin Quack, and Oleg N Ulenikov. High resolution ftir spectroscopy of fluoroform 12chf3 and critical analysis of the infrared spectrum from 25 to 1500 cm- 1. *Molecular Physics*, 116(9):1091–1107, 2018.

[73] Edoardo Vicentini, Alessio Gambetta, Nicola Coluccelli, Eugenio Fasci, Antonio Castrillo, Livio Gianfrani, Valentina Di Sarno, Pasquale Maddaloni, Adina Ceausu-Velcescu, Paolo De Natale, et al. Rovibrational fine structure and transition dipole moment of cf3h by frequency-comb-assisted saturated spectroscopy at 8.6 μm. *Journal of Quantitative Spectroscopy and Radiative Transfer*, 217:373–379, 2018.

[74] Richard M Williams, James F Kelly, John S Hartman, Steven W Sharpe, Matthew S Taubman, John L Hall, Federico Capasso, Claire Gmachl, Deborah L Sivco, James N Baillargeon, et al. Kilohertz linewidth from frequency-stabilized mid-infrared quantum cascade lasers. *Optics letters*, 24(24):1844–1846, 1999.

[75] Tanya L Myers, Richard M Williams, Matthew S Taubman, Claire Gmachl, Federico Capasso, Deborah L Sivco, James N Baillargeon, and Alfred Y Cho. Free-running frequency stability of mid-infrared quantum cascade lasers. *Optics letters*, 27(3):170–172, 2002.

[76] Gianni Di Domenico, Stéphane Schilt, and Pierre Thomann. Simple approach to the relation between laser frequency noise and laser line shape. *Applied optics*, 49(25):4801–4807, 2010.

[77] Alessio Gambetta, Nicola Coluccelli, Marco Cassinerio, Davide Gatti, Paolo Laporta, Gianluca Galzerano, and Marco Marangoni. Milliwatt-level frequency combs in the 8–14 μm range via difference frequency generation from an er: fiber oscillator. *Optics letters*, 38(7):1155–1157, 2013.

[78] Alessio Gambetta, Marco Cassinerio, Nicola Coluccelli, Eugenio Fasci, Antonio Castrillo, Livio Gianfrani, Davide Gatti, Marco Marangoni, Paolo Laporta, and Gianluca Galzerano. Direct phase-locking of a 8.6-μm quantum cascade laser to a mid-ir optical frequency comb: application to precision spectroscopy of n 2 o. *Optics letters*, 40(3):304–307, 2015.

[79] A Gambetta, E Vicentini, N Coluccelli, Y Wang, TT Fernandez, P Maddaloni, P De Natale, A Castrillo, L Gianfrani, P Laporta, et al. Versatile mid-infrared frequency-comb referenced sub-doppler spectrometer. *APL Photonics*, 3(4): 046103, 2018.

[80] Pawel Kluczynski, Jörgen Gustafsson, Åsa M Lindberg, and Ove Axner. Wavelength modulation absorption spectrometry—an extensive scrutiny of the generation of signals. *Spectrochimica Acta Part B: Atomic Spectroscopy*, 56(8): 1277–1354, 2001.

[81] Jonas Westberg, Junyang Wang, and Ove Axner. Fast and non-approximate methodology for calculation of wavelength-modulated voigt lineshape functions suitable for real-time curve fitting. *Journal of Quantitative Spectroscopy and Radiative Transfer*, 113(16):2049–2057, 2012.

[82] S Bartalini, S Borri, P Cancio, A Castrillo, I Galli, G Giusfredi, D Mazzotti, L Gianfrani, and P De Natale. Observing the intrinsic linewidth of a quantum-cascade laser: beyond the schawlow-townes limit. *Physical review letters*, 104 (8):083904, 2010.

[83] Ilia Sergachev, Richard Maulini, Alfredo Bismuto, Stéphane Blaser, Tobias Gresch, Yves Bidaux, Antoine Müller, Stéphane Schilt, and Thomas Südmeyer. All-electrical frequency noise reduction and linewidth narrowing in quantum cascade lasers. *Optics letters*, 39(22):6411–6414, 2014.

[84] Lionel Tombez, Stéphane Schilt, Daniel Hofstetter, and Thomas Südmeyer. Active linewidth-narrowing of a mid-infrared quantum cascade laser without optical reference. *Optics letters*, 38(23):5079–5082, 2013.

[85] Papa Lat Tabara Sow, Sinda Mejri, Sean K Tokunaga, Olivier Lopez, Andrey Goncharov, Bérengère Argence, Christian Chardonnet, Anne Amy-Klein, Christophe Daussy, and Benoît Darquié. A widely tunable 10-μ m quantum cascade laser phase-locked to a state-of-the-art mid-infrared reference for precision molecular spectroscopy. *Applied Physics Letters*, 104(26):264101, 2014.

[86] Michael G Hansen, Evangelos Magoulakis, Qun-Feng Chen, Ingo Ernsting, and Stephan Schiller. Quantum cascade laser-based mid-ir frequency metrology system with ultra-narrow linewidth and 1$\times$ 10- 13-level frequency instability. *Optics letters*, 40(10):2289–2292, 2015.

[87] John D Jost, John L Hall, and Jun Ye. Continuously tunable, precise, single frequency optical signal generator. *Optics Express*, 10(12):515–520, 2002.

[88] S Bartalini, P Cancio, G Giusfredi, D Mazzotti, P De Natale, S Borri, I Galli, T Leveque, and Livio Gianfrani. Frequency-comb-referenced quantum-cascade laser at 4.4 μm. *Optics letters*, 32(8):988–990, 2007.

[89] F Cappelli, I Galli, S Borri, G Giusfredi, P Cancio, D Mazzotti, A Montori, N Akikusa, M Yamanishi, S Bartalini, et al. Subkilohertz linewidth room-temperature mid-infrared quantum cascade laser using a molecular subdoppler reference. *Optics letters*, 37(23):4811–4813, 2012.

[90] Simone Borri, Saverio Bartalini, Pablo Cancio, Iacopo Galli, Giovanni Giusfredi, Davide Mazzotti, and Paolo De Natale. Quantum cascade lasers for high-resolution spectroscopy. *Optical Engineering*, 49(11):111122, 2010.

[91] Eugenio Fasci, Nicola Coluccelli, Marco Cassinerio, Alessio Gambetta, Laurent Hilico, Livio Gianfrani, Paolo Laporta, Antonio Castrillo, and Gianluca Galzerano. Narrow-linewidth quantum cascade laser at 8.6 μm. *Optics letters*, 39(16):4946–4949, 2014.

[92] Matthew S Taubman, Tanya L Myers, Bret D Cannon, Richard M Williams, Federico Capasso, Claire Gmachl, Deborah L Sivco, and Alfred Y Cho. Frequency stabilization of quantum-cascade lasers by use of optical cavities. *Optics letters*, 27(24):2164–2166, 2002.

[93] Alessio Gambetta, Edoardo Vicentini, Yuchen Wang, Nicola Coluccelli, Eugenio Fasci, Livio Gianfrani, Antonio Castrillo, Valentina Di Sarno, Luigi Santamaria, Pasquale Maddaloni, et al. Absolute frequency measurements of chf 3 doppler-free ro-vibrational transitions at 8.6 μm. *Optics Letters*, 42(10):1911–1914, 2017.

[94] Jon H Shirley. Modulation transfer processes in optical heterodyne saturation spectroscopy. *Optics Letters*, 7(11):537–539, 1982.

[95] Jun Ye, Long Sheng Ma, and John L Hall. Molecular iodine clock. *Physical review letters*, 87(27):270801, 2001.

[96] Shengnan Zhang, Xiaogang Zhang, Jingzhong Cui, Zhaojie Jiang, Haosen Shang, Chuanwen Zhu, Pengyuan Chang, Ling Zhang, Jianhui Tu, and Jingbiao Chen. Compact rb optical frequency standard with 10- 15 stability. *Review of Scientific Instruments*, 88(10):103106, 2017.

[97] Esa Jaatinen, David J Hopper, and Julian Back. Residual amplitude modulation mechanisms in modulation transfer spectroscopy that use electro-optic modulators. *Measurement Science and Technology*, 20(2):025302, 2008.

[98] Y Natali Martinez de Escobar, Silvana Palacios Álvarez, Simon Coop, Thomas Vanderbruggen, Krzysztof T Kaczmarek, and Morgan W Mitchell. Absolute frequency references at 1529 and 1560 nm using modulation transfer spectroscopy. *Optics letters*, 40(20):4731–4734, 2015.

[99] Sang Eon Park, Ho Seong Lee, Taeg Yong Kwon, and Hyuck Cho. Dispersion-like signals in velocity-selective saturated-absorption spectroscopy. *Optics communications*, 192(1-2):49–55, 2001.

[100] Sho Okubo, Yi-Da Hsieh, Hajime Inaba, Atsushi Onae, Mamoru Hashimoto, and Takeshi Yasui. Near-infrared broadband dual-frequency-comb spectroscopy with a resolution beyond the fourier limit determined by the observation time window. *Optics express*, 23(26):33184–33193, 2015.

[101] Nicola Coluccelli, Marco Cassinerio, Alessio Gambetta, Paolo Laporta, and Gianluca Galzerano. Frequency-noise measurements of optical frequency combs by multiple fringe-side discriminator. *Scientific reports*, 5(1):1–10, 2015.

[102] Esther Baumann, Fabrizio R Giorgetta, William C Swann, Alexander M Zolot, I Coddington, and Nathan R Newbury. Spectroscopy of the methane ν 3 band with an accurate midinfrared coherent dual-comb spectrometer. *Physical Review A*, 84(6):062513, 2011.

[103] Sho Okubo, Kana Iwakuni, Hajime Inaba, Kazumoto Hosaka, Atsushi Onae, Hiroyuki Sasada, and Feng-Lei Hong. Ultra-broadband dual-comb spectroscopy across 1.0–1.9 μm. *Applied Physics Express*, 8(8):082402, 2015.

[104] Markus Brehm, Albert Schliesser, and Fritz Keilmann. Spectroscopic near-field microscopy using frequency combs in the mid-infrared. *Optics express*, 14(23):11222–11233, 2006.

[105] Sylvain Boudreau, Simon Levasseur, Carlos Perilla, Simon Roy, and Jérôme Genest. Chemical detection with hyperspectral lidar using dual frequency combs. *Optics express*, 21(6):7411–7418, 2013.

[106] Martin Godbout, Jean-Daniel Deschênes, and Jérôme Genest. Spectrally resolved laser ranging with frequency combs. *Optics express*, 18(15):15981–15989, 2010.

[107] Takuro Ideguchi, Simon Holzner, Birgitta Bernhardt, Guy Guelachvili, Nathalie Picqué, and Theodor W Hänsch. Coherent raman spectro-imaging with laser frequency combs. *Nature*, 502(7471):355–358, 2013.

[108] Takuro Ideguchi, Birgitta Bernhardt, Guy Guelachvili, Theodor W Hänsch, and Nathalie Picqué. Raman-induced kerr-effect dual-comb spectroscopy. *Optics letters*, 37(21):4498–4500, 2012.

[109] Arthur Hipke, Samuel A Meek, Takuro Ideguchi, Theodor W Hänsch, and Nathalie Picqué. Broadband doppler-limited two-photon and stepwise excitation spectroscopy with laser frequency combs. *Physical Review A*, 90(1):011805, 2014.

[110] Lukasz A Sterczewski, Jonas Westberg, Yang Yang, David Burghoff, John Reno, Qing Hu, and Gerard Wysocki. Terahertz hyperspectral imaging with dual chip-scale combs. *Optica*, 6(6):766–771, 2019.

[111] Kyuki Shibuya, Takeo Minamikawa, Yasuhiro Mizutani, Hirotsugu Yamamoto, Kaoru Minoshima, Takeshi Yasui, and Tetsuo Iwata. Scan-less hyperspectral dual-comb single-pixel-imaging in both amplitude and phase. *Optics Express*, 25(18):21947–21957, 2017.

[112] Pedro Martín-Mateos, Farid Ullah Khan, and Oscar Elías Bonilla-Manrique. Direct hyperspectral dual-comb imaging. *Optica*, 7(3):199–202, 2020.

[113] Farid Ullah Khan, Guillermo Guarnizo, and Pedro Martín-Mateos. Direct hyperspectral dual-comb gas imaging in the mid-infrared. *Optics Letters*, 45 (19):5335–5338, 2020.

[114] Nathan R Newbury, Ian Coddington, and William Swann. Sensitivity of coherent dual-comb spectroscopy. *Optics express*, 18(8):7929–7945, 2010.